Strategies for development of high-performing open-cathode polymer electrolyte membrane fuel cells

by

Anand Sagar

M.Tech., Indian Institute of Technology Hyderabad, 2015

Thesis Submitted in Partial Fulfillment of the
Requirements for the Degree of
Doctor of Philosophy

in the
School of Mechatronic Systems Engineering
Faculty of Applied Sciences

SIMON FRASER UNIVERSITY
Summer 2023

Declaration of Committee

Name:	**Anand Sagar**
Degree:	**Doctor of Philosophy**
Title:	**Strategies for development of high-performing open-cathode polymer electrolyte membrane fuel cells**

Committee:

Chair: **Farshid Najafi**
Assistant Professor, Mechatronic Systems Engineering

Erik Kjeang
Supervisor
Professor, Mechatronic Systems Engineering

Dave Ghosh
Committee Member
Adjunct Professor, Mechatronic Systems Engineering

Christopher L. Gardner
Committee Member
Research Associate, Mechatronic Systems Engineering

Sachin Chugh
Committee Member
Chief Research Manager and CEA to Director (R&D), R&D Centre, Indian Oil Corporation Limited, India

Krishna Vijayaraghavan
Examiner
Associate Professor, Mechatronic Systems Engineering

Trung Van Nguyen
External Examiner
Professor, Chemical and Petroleum Engineering
University of Kansas

Abstract

The fuel cell technology commercialization is greatly dependent on the efficiency, cost, and durability of the fuel cell stacks. These are coupled with the effectiveness of the thermal and water management of polymer electrolyte membrane fuel cell (PEMFC) systems. The conventional liquid-cooled PEMFC systems include several balance of plant components like humidifiers, compressors, heat exchangers, etc. for an efficient operation leading to overall increased cost. The open-cathode PEMFC systems on the other hand use minimal auxiliary components by using ambient air as an oxidant as well as a coolant for extracting the heat away from the system. They offer lower system size and easier operation, with the main tradeoff being low efficiency. This thesis aims to investigate novel strategies for the development of high-performing open-cathode systems by using a computational modelling approach followed by experimental investigations. Firstly, a comprehensive, three-dimensional computational fuel cell model is developed, validated, and utilized to study the operational and hygrothermal behaviour of an open-cathode PEMFC at various ambient conditions compared to conventional liquid cooled cells. Moderate self-heating followed by membrane drying is found to be the key contributors towards lower cell performance for open-cathode cells while in operation at moderate-to-high current densities and high air flow rates. At the component level, the water sorption/desorption rate constant (γ) for the ionomer is found detrimental to the overall cell performance; the current density at 0.6 V is found to increase remarkably by 130% by reducing γ from 10 s^{-1} to 0.1 s^{-1} under given ambient air conditions. This is accomplished through enhanced water retention and membrane hydration at elevated temperature. On further investigation, the strategic cathode catalyst layer (thin, high Pt/C ratio, high ionomer loading), cathode microporous layer (thin, high porosity), and membrane (thin) design is found to enable collective improvements in kinetics, oxygen mass transport, ohmic resistance, self-heating, and water retention in the ionomer phase. Lastly, these findings from the computational model are experimentally validated and a current density rise of 88% at 0.6 V and 53% at 0.4 V is achieved by the strategically designed membrane electrode assembly for open-cathode cells offering increased power density.

Keywords: open-cathode; power density; fuel cell; ionomer; microporous layer; three-dimensional model

To my beloved family!

Acknowledgments

I would like to express my deepest gratitude to my senior supervisor, Dr. Erik Kjeang, for his constant support, patience, motivation, enthusiasm, and immense knowledge throughout my PhD program. It has been a wonderful journey and a true honor for getting the opportunity to work with Dr. Kjeang.

I would like to thank Dr. Christopher L Gardner and Dr. Dave Ghosh for providing me with support and guidance at every step of my program.

I would like to thank my supervisor, Mr. Sachin Chugh, and Mr. Alok Sharma from Indian Oil R&D for providing valuable advice, support, and suggestions during my program.

I would like to acknowledge SFU and Indian Oil R&D for the financial support and facilities for research. This research was funded and administered through the SFU – Indian Oil joint PhD program in clean energy.

I would also like to thank the members of the Fuel Cell Research Lab (FCReL) at SFU, Canada, and scientists at Indian Oil R&D for their consistent support as well as cooperation towards the success of my PhD. I am thankful to all the administrative staff at MSE office of SFU and Indian Oil R&D for their seamless support rendered throughout my graduate study. I would like to thank Mr. Kapil Sonkar (Indian Oil R&D), Dr. K. Mohanraju (Indian Oil R&D), Dr. Meenakshi Sundarraman (Indian Oil R&D), Dr. Paran Jyoti Sarma (Indian Oil R&D, SFU) for their useful advice.

Finally, I am deeply grateful to my teachers, mentors, and my family for their consistent support who have inspired me to pursue my research career.

Table of contents

Declaration of Committee ii

Abstract iii

Dedications iv

Acknowledgments v

Table of contents vi

List of figures viii

List of tables ix

List of acronyms x

List of greek symbols xii

List of appendices xiii

Organization of the dissertation xiv

Chapter 1. 1

Introduction 1

1.1 Polymer electrolyte membrane fuel cells 1

1.2 Types of cooling in PEMFCs 5

1.3 Open cathode PEM fuel cell 7

1.4 MEA design effect in PEMFCs 11

1.5 PEM fuel cell modelling 17

Objectives and Scope 19

Chapter 2. 20

Materials and methods 20

2.1 Modelling details 20

2.2 Experimental details 27

Chapter 3. 31

Summary of Contributions 31

3.1 A computational analysis on the operational behaviour of open-cathode polymer electrolyte membrane fuel cells 31

3.2 Strategic ionomer design for high performing fuel cells with open cathode 34

3.3 Model driven membrane electrode assembly design for high-performing open-cathode polymer electrolyte membrane fuel cells 39

3.4 Experimental design of high performing open cathode polymer electrolyte membrane fuel cells 45

Chapter 4. 50

Conclusions and Future work 50

4.1 Conclusions 50

4.2 Future work 54

References 56

Appendices 68

Appendix-A A computational analysis on the operational behaviour of open-cathode polymer electrolyte membrane fuel cells 69

Appendix-B Strategic ionomer design for high performing fuel cells with open cathode.. 84

Appendix-C Model driven membrane electrode assembly design for high-performing open-cathode polymer electrolyte membrane fuel cells. 92

Appendix-D Experimental design of high performing open cathode polymer electrolyte membrane fuel cells…….…….. 126

List of figures

Figure 1. Exploded view of a PEMFC 2
Figure 2. Voltage losses in a PEM fuel cell 4
Figure 3. Schematic of a conventional PEM fuel cell system 5
Figure 4. (a) Conventional liquid-cooled PEMFC system. (b) Open-cathode PEMFC system 8
Figure 5. Schematic of GDL/MPL microstructure in a PEMFC 13
Figure 6. Schematic of oxygen and water transport at the MEA level of a PEMFC 16
Figure 7. (a) 3D schematic of the computational domain used for modelling. (b) BCs used for modelling 21
Figure 8. Experimental setup of single-cell open-cathode PEMFC 28
Figure 9. Greenlight Innovation G60 fuel cell test station setup at IOC R&D Centre 29
Figure 10. (a) Model validation result for case-1 and (b) RH difference between inlet and outlet in the cathode air flow as a function of cell voltage. 33
Figure 11. Effect of ionomer water sorption/desorption rate constant (γ) on the (a) polarization curve and (b) average water content at the PEM for open-cathode PEMFC systems 36
Figure 12. (a) Average RH profile at the cathode side for (a) $\gamma = 10\ s^{-1}$ and (b) $\gamma = 0.1\ s^{-1}$ 38
Figure 13. Comparative polarization curves for the baseline MEA design and the parametrically modified MEAs with (a) best CCL design and (b) best CMPL design 42
Figure 14. CD trend for the MEA design changes at 0.6 V 43
Figure 15. (a) Pareto charts obtained from ANOVA analysis at (a) 0.6 V and (b) 0.4 V. 45
Figure 16. (a) Current density for the five MEAs operated at cell voltages of 0.6 V and 0.4 V at steady state, following thermal equilibration and (b) Comparative Nyquist plot of impedance for the five MEAs obtained by in-situ EIS on the single cell open-cathode fuel cell operated at 0.6 V. 49

List of tables

Table 1. Dimensions of the open-cathode single cell used for 3D modelling..... 22
Table 2. List of parameters used for the 3D computational modelling..... 24
Table 3. Operating conditions used for simulating open-cathode PEMFC performance. 32
Table 4. Parametric design of MEA components for simulation and performance comparison of open-cathode PEMFCs..... 39
Table 5. List of DoE design factors and levels..... 43
Table 6. Details of the different MEAs prepared for open-cathode fuel cell testing. 46

List of acronyms

3D	Three dimensional
AC	Alternating current
ACL	Anode catalyst layer
ANOVA	Analysis of variance
BC	Boundary condition
BoP	Balance of plant
BPP	Bi-polar plate
CL	Catalyst layer
CCL	Cathode catalyst layer
CCM	Catalyst coated membrane
CD	Current density
CMPL	Cathode microporous layer
DoE	Design of experiments
ECSA	Electrochemical active surface area
EIS	Electrochemical impedance spectroscopy
GDE	Gas diffusion electrode
GDL	Gas diffusion layer
H	High
HFR	High frequency resistance
L	Low

LSC	Long side chain
MEA	Membrane electrode assembly
MPL	Microporous layer
nlpm	Normal liters per minute
OCV	Open circuit voltage
ORR	Oxygen reduction reaction
PEM	Polymer electrolyte membrane
PEMFC	Polymer electrolyte membrane fuel cell
Pt	Platinum
Pt/C	Platinum on carbon
PTFE	Polytetrafluoroethylene
RH	Relative humidity
RMS	Root mean square
SSC	Short side chain

List of greek symbols

α_i	Charge transfer coefficient at i^{th} electrode
γ	Water sorption/desorption rate constant (s^{-1})
ε_i	Volume fraction of i^{th} domain
η	Overpotential (V)
λ	Water content
μ_i	Dynamic viscosity of the i^{th} species (Pa s)
ρ_i	Density of the i^{th} species (kg m^{-3})
σ_i	Effective electrolyte conductivity of i^{th} domain (S m^{-1})
Σ	Summation
ϕ_i	Potential at i^{th} electrode (V)

List of appendices

Appendix A: A computational analysis on the operational behaviour of open-cathode polymer electrolyte membrane fuel cells

Appendix B: Strategic ionomer design for high performing fuel cells with open cathode

Appendix C: Model driven membrane electrode assembly design for high-performing open-cathode polymer electrolyte membrane fuel cells

Appendix D: Experimental design of high-performing open-cathode polymer electrolyte membrane fuel cells

Organization of the dissertation

This dissertation is prepared with the following organization: Chapter 1 provides the motivation for the thesis, an introduction to polymer electrolyte membrane fuel cells (PEMFCs), types of cooling in PEMFCs, design, and details of open-cathode PEMFCs along with the challenges and limitations, a brief discussion on modelling related works done previously in the area of PEMFCs and open-cathode, and objectives and scope. Chapter 2 includes the materials and methods with subsections namely, modelling details and experimental details. The main contributions of this work are briefly summarized in Chapter 3. The details of each part of the work are provided in Appendices (A-D) at the end of the thesis, where the results are arranged in the form of published journal articles and drafted manuscripts. Finally, Chapter 4 discusses the overall findings, conclusions, and future work.

Chapter 1.

Introduction

Hydrogen is proposed to be widely used as the primary energy carrier across various parts of the globe leading to the development of a hydrogen economy. The full scale hydrogen economy development is envisaged to benefit the environment, strengthen energy security, and advantage the end users in various ways [1]. The feasibility of hydrogen usage ranges from the electrochemical route using fuel cells, co-combustion with other fuels, and direct combustion [2]. Also, the available processes for hydrogen production are several namely gasification, steam methane reforming, pyrolysis, photobiolysis, and water electrolysis to name a few [3]. Following the decarbonization goals, most of the countries have set high targets for H_2 production and usage. The hydrogen strategy for Canada projects the use of nearly 30% of its secondary energy usage to be met by H_2 by 2050 [4]. At the same time, a developing economy like India targets to become a front runner in H_2 production by 2030 with projections of five million tons of green H_2 production [5]. The use of H_2 through polymer electrolyte membrane fuel cells (PEMFCs) has shown a wide range of applicability from stationary applications to automotive applications and various other applications [6–8]. However, the high cost of the overall PEMFC systems has been a critical inhibitor towards the commercialization of this technology unlike conventional energy sources [9]. The use of the balance of plant (BoP) components incurs a significant cost to the overall system for conventional liquid-cooled PEMFCs [10]. This brings our interest to study and understand the various operational aspects of an open-cathode PEMFC which uses ambient air both as an oxidant and coolant and thereby uses minimal BoP components [11].

1.1 Polymer electrolyte membrane fuel cells

A fuel cell is defined as an electrochemical cell in which the chemical energy of a fuel and an oxidizing agent gets converted to electricity by means of a redox reaction taking place [12]. A fuel cell stack comprises several unit cells arranged in series with the net cell voltage as the summation of individual cell voltages. Based on the selection of fuel and

oxidant pairs and their operating temperature, various types of fuel cells are broadly categorized. PEMFCs are among the most prominent fuel cell technologies being used for several applications ranging from high power stationary sources, and mid-power automotive applications to low power portable devices [13]. Commercial PEMFCs mostly use high-grade hydrogen with a purity level of up to 99.999% as fuel and ambient air as oxidant. The PEMFC comprises graphite or metal-based bipolar plates which carry reactant gases onto the cell, a carbon-based macroporous backing layer also called a gas diffusion layer (GDL) which allows gases to diffuse to the reactant site passing through a microporous layer (MPL) and reaching the catalyst layer (CL) which is coated on top of a polymeric membrane which acts as an ion transport media [14]. The exploded view is depicted in Figure 1. The respective electrochemical reactions at the anode and cathode take place at the membrane-CL interface which is a three-phase boundary where electrolyte, electrode, and reactant gases co-exist at one site as shown in (1), (2), and (3) [15].

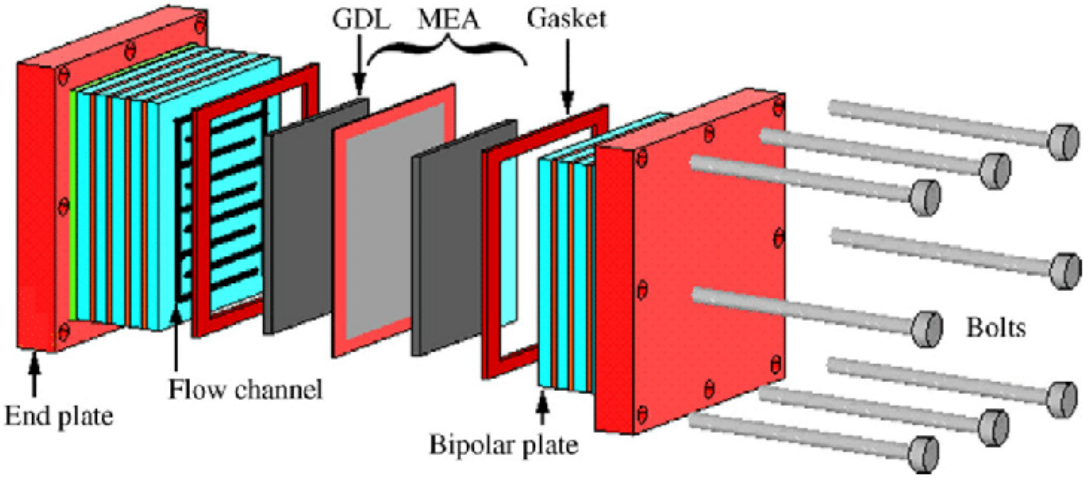

Figure 1. Exploded view of a PEMFC. "Reproduced with permission from [16] © 2007 Elsevier Science & Technology Journals; permission conveyed through Copyright Clearance Center, Inc."

$$H_2 \rightarrow 2H^+ + 2e^-;\ E^0 = 0.0\ V \quad \textbf{(1)}$$

$$\frac{1}{2}\,O_2 + 2H^+ + \,2e^- \rightarrow H_2O\;;\; E^0 = 1.23\,V \quad \textbf{(2)}$$

Overall cell reaction: $H_2 + \frac{1}{2}\,O_2 \rightarrow H_2O$ **(3)**

The H_2 coming at the anode side oxidizes at anode CL to produce H^+ ions along with e^-. The protons produced at the anode CL pass through the ion-conducting membrane and reach the cathode CL where they combine with the e^- flowing through the outer circuit and O_2 to produce $\mathrm{H}_2\mathrm{O}$ as the only by-product other than the heat released in the process [17]. The theoretical cell voltage for the PEMFC is 1.23 V. However, due to losses pertaining to mixed potential and hydrogen crossover, the open-circuit voltage (OCV) is near 1.0 V. The cell voltage drops subsequently when a current is drawn from the cell. Various other losses come into consideration when operating at different current regimes namely the kinetic losses, ohmic losses, and mass transport losses as shown in Figure 2.

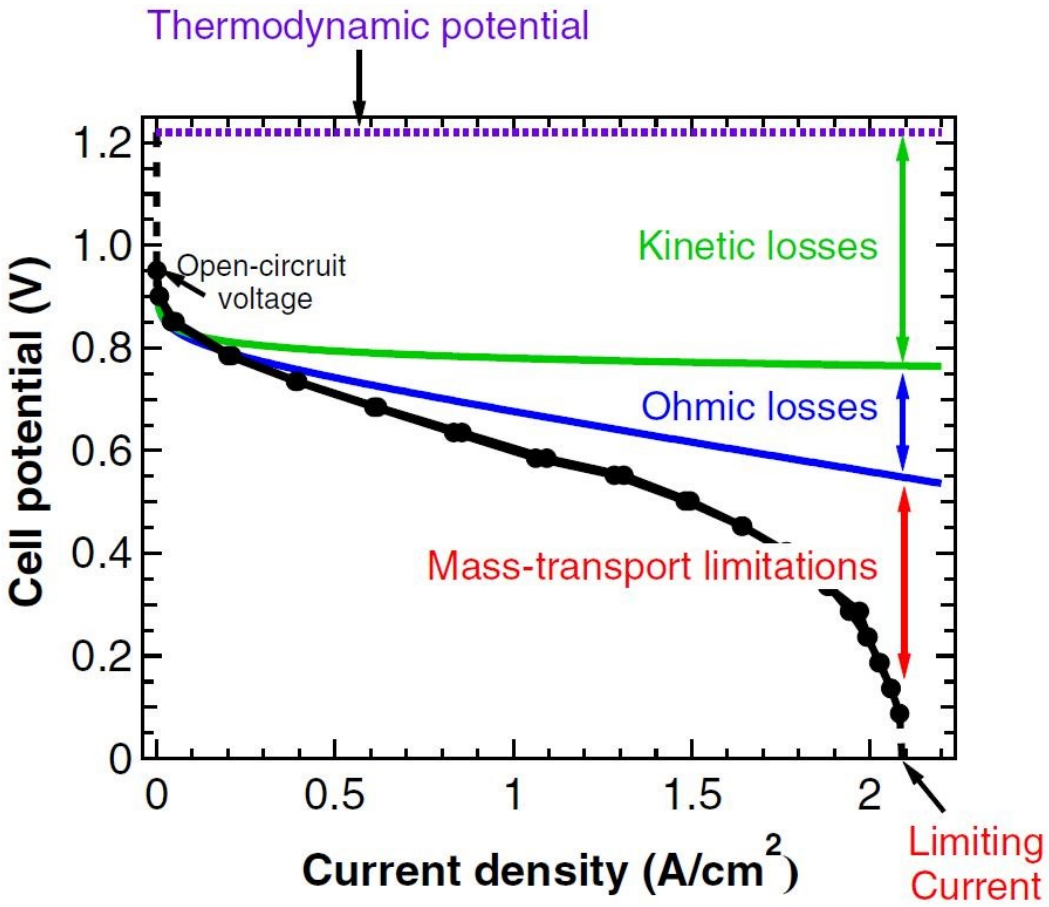

Figure 2. Voltage losses in a PEM fuel cell. "Reproduced with permission from [18] © 2014 IOP Publishing, Ltd; permission conveyed through Copyright Clearance Center, Inc."

The maximum cell voltage which a PEMFC can theoretically produce is called the thermoneutral voltage (E_{th}) which corresponds to the cell voltage considering all the enthalpy change of the reactant gases is converted to electrical energy. E_{th} is determined based on the phase in which the product water is present in the fuel cell. If the product water is in the liquid phase, E_{th} is considered to be at 1.48 V; whereas for water produced in the gaseous phase, E_{th} is near 1.25 V. The standard equilibrium potential (E_N) is further calculated based on the Nernst equation at given temperature and pressure conditions [19]. The actual cell voltage obtained for a fuel cell in operation mode is OCV minus the voltage losses occurring in the cell. At lower current densities, activation losses are more evident which is due to the energy consumed in crossing the threshold energy barrier for the redox reaction to take place. It refers to the losses due to the kinetics of charge transfer reaction across the electrode-electrolyte interface [20]. Ohmic losses are offered primarily by membrane dehydration and resistance is offered due to protonic resistance from the membrane and ionomer dominates the overall losses while operating at medium current densities [21]. The thickness and ionic conductivity of the membrane play a major role in deciding the ohmic losses [22]. Whereas, at high current densities, the amount of water produced is higher which blocks the pathway for reactant gases thereby offering mass transport losses as dominant voltage loss. Also, if the rate of fuel/oxidant supplied is less than the rate of consumption of reactants, concentration polarization losses or mass transport losses may occur [23].

The conventional PEMFC systems operate at moderate pressure and with fully humidified flows. They also use liquid coolant to maintain the stack temperature [24]. For the efficient running of a fuel cell system, BoP components like an air compressor, humidifiers, and heat exchangers are required to meet the pressure, temperature, and thermal balance demands as depicted in Figure 3. However, they consume additional power which falls under the auxiliary losses and incurs extra costs [25]. The total cost includes the capital cost for setting up such BoP components and operational costs. The BoP components constitute nearly 35% of the total cost of the system for transport applications [10].

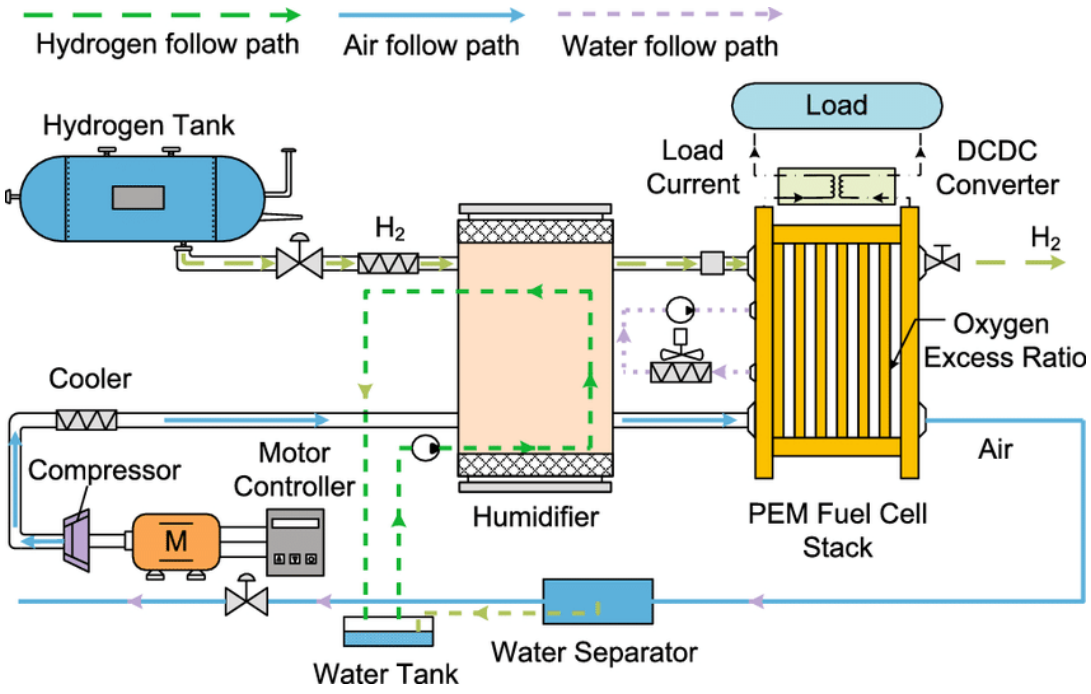

Figure 3. Schematic of a conventional PEM fuel cell system. "Reproduced with permission from [26] © 2020 Springer Nature BV; permission conveyed through Copyright Clearance Center, Inc."

1.2 Types of cooling in PEMFCs

The overall heat generated in a PEMFC is calculated by the difference in E_{th} and V_{cell} multiplied by the current drawn. The different sources of heat generation constitute irreversible heat produced in the electrochemical reaction, entropic heat of reaction, ohmic heat production, and the heat produced due to phase change [19]. The heat generated by a PEMFC is critical for the health of the cell when operated for a long time at high current densities [27]. The rate of heat removal with reference to the rate of heat generated in the system decides the thermal balance of the system and consequently the efficiency of the overall system. The maintenance of a certain temperature level is crucial to the cell performance as it guides the cell kinetics which decides the overall rate of electrochemical reaction taking place at the individual cell level. The polymeric membrane acts as a protonic conductor in a PEMFC and the overall ionic resistance is greatly dependent on the membrane hydration and temperature as shown in (4) where, $'\sigma_m'$ represents the ionic conductivity of the membrane, λ depicts the local water content at the membrane, and T is the membrane operating temperature [7]. The ionic resistance is found to contribute

significantly to the overall cell performance. However, enhancement of cell temperature over a cutoff temperature can lead to severe membrane dehydration and also impact cell kinetics adversely. There are various ways of extracting the extra heat from a PEMFC as listed below.

$$\sigma_m = (0.5139\lambda - 0.326)\exp[1268\,(\tfrac{1}{303} - \tfrac{1}{T})] \quad \textbf{(4)}$$

Using liquid cooling

The cooling of a PEMFC is done conventionally using liquid coolants or antifreeze [19] which are circulated across the individual cells to extract the extra heat generated in the system. The cooling channels are engraved on an extra plate in addition to the flow channels for the purpose of carrying coolants onto the system. However, it adds extra weight to the overall system which reduces the specific power density of the system. Most of the commercial PEMFC stacks designed for high power applications (> 5 kW) use this strategy for cooling. The suitable applications for such systems involve automotive stacks and stacks used for stationary applications. The design of the cooling channel is optimized based on the power requirements of the stack being operated.

Using heat spreaders or heat pipes

The bipolar plate used in a PEMFC also acts as a carrier for the removal of the extra heat generated inside the cell. Due to conduction, the heat generated is transferred to the external bipolar plate which is further dissipated to the ambient through the external surface of bipolar plates. The use of heat spreaders in a bipolar plate further enhances the rate of heat dissipation which brings efficient thermal management inside the cell. The heat pipes are external materials that are embedded into the graphite plates and help in the heat transport of the system. This type of cooling is also called edge cooling or passive cooling. The use of a coolant pump can be eliminated in this type of cooling, unlike conventional liquid cooling, thereby reducing the overall size of the cooling system. The heat spreader material used for this kind of cooling uses high thermal conductive materials like expanded graphite or pyrolytic graphite to extract the extra heat from the system [28].

Cooling with separate airflow

Ambient air can also be used for cooling the PEMFC stack by passing through separate channels engraved onto the bipolar plate. This type of cooling technique has been found

suitable to operate on low power application stacks ranging from 100 W up to 2 kW. Ballard Power Systems has used this technology for PEMFC stacks even up to 5 kW by use of new, lost cost materials. This kind of stacks have added advantage of low system weight and low parasitic losses as compared to conventional liquid-cooled stacks, however, have their limitations in terms of thermal management [13], [23].

Cooling with phase change materials

This method of cooling uses the latent heat of the coolant, unlike the liquid cooling approach where the sensible heat of the coolant is used to take out the heat from the system. The latent heat of such phase change materials is up to 500 times higher than the sensible heat possessed by the liquid coolants, which gives an advantage of low coolant flow rate requirement. The coolant is thus guided by the pressure difference, or the density difference and an external coolant pump is not required in such systems. This type of cooling is attained in two ways, evaporative cooling and cooling through boiling. The boiling temperature of the coolant is kept higher than the PEMFC stack temperature in case of evaporative cooling and water is mostly used in such kinds of cooling processes. On the other hand, in the cooling through boiling approach, the choice of coolant is made on its temperature being kept lower than the PEMFC stack temperature [24-25].

1.3 Open cathode PEM fuel cell

Introduction

A conventional PEMFC system generally uses humidified fuel and oxidants and operates at moderate pressure to achieve high fuel cell performance. The humidifiers, compressors, pressure regulators, and other such components are used as a part of the system which increases the total weight of the system along with its cost. On the other hand, open-cathode PEMFCs use ambient air both as an oxidant as well as coolant which eliminates the use of external BoP components needed for coolant supply and handling [29]. This kind of system design reduces the overall mass of the system and makes the operation much easier thereby reducing the overall cost of the system [30]. The ambient air used as coolant and oxidant can be directly provided by natural convection which is called air-breathing fuel cell systems [31]. However, such systems are limited to very low performance since the low ambient air flow is also not able to extract the heat generated

inside the cell and thereby causes thermal and water management issues resulting in limiting cell performance [32]. This kind of passive air cooling can be used for very low power applications ranging from milliwatt to watt level.

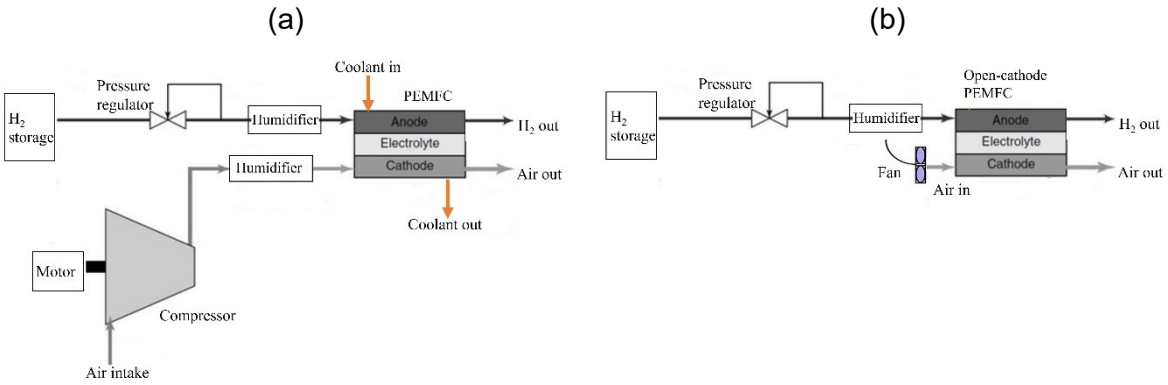

Figure 4. (a) Conventional liquid cooled PEMFC system. (b) Open-cathode PEMFC system.

The other type of air-cooled system which utilizes an external fan/blower to send the air onto the system for cooling the PEM fuel cell uses the forced convection mode as shown in Figure 4. In this kind of system, the external humidifier and compressor needed for a conventional fuel cell system are eliminated which drastically reduces the overall cost and size of the system. The fan/blower used additionally adds to some small parasitic losses to the overall system which contributes a very low percentage of the overall power being generated from the system [33]. This design of PEMFC is usually referred to as open-cathode design and has various advantages in terms of simple stacking, easy handling, lighter weight, and overall, less system cost as compared to conventional fuel cell systems [34].

The use of a fan/blower is integral for an open-cathode PEMFC where forced convection is the key phenomenon guiding the fuel cell dynamics. The selection of fan type and it's positioning along with the control of the fan becomes an important guiding factor toward overall cell performance. The fan connected to the open-cathode system provides ambient air onto the fuel cell which extracts the heat generated under load and hence determines the thermal management of the system [35]. Axial fans are generally preferred over centrifugal ones to exploit the large air flows which can be achieved by overcoming large pressure drops [36]. A numerical study [37] suggested that suitable fan selection can be derived based on analysis of the fuel cell system characteristic curve and the fan

characteristic curve. The point of open-cathode stack operation is suggested to fall in the optimized operational region of the fan and far from the unstable operational zone of the fan. As compared to a fan configuration with the fan attached in blower mode, the one with the fan attached in suction mode was found to give superior cell performance for an open-cathode system associated with more uniform temperature and velocity distribution and higher power generation [38]. The duty cycle of the fan was also found to be affecting the open-cathode PEMFC performance to a greater extent noticeably at the high current operation as compared to the low current operation. The effect of changing fan speed on various operating parameters like cell temperature, stack voltage, and parasitic power losses revealed that the open-cathode system showed less performance while operated at low fan speed consuming high power and this may also lead to heat accumulation in the system thereby poor thermal management [39]. A better stack temperature regulation was found to be achieved with regulated fan operation as compared to a non-regulated fan operation, which contributes to the overall performance enhancement [40].

The configuration of cathode channels in an open-cathode system becomes important since it decides the overall flow rate of air flowing through the fuel cell. The aspect ratio (width/depth) of the flow channel and the overall flow cross-sectional area has been tested while operating a 100 cm^2 single-cell open-cathode system operated at 25 ^oC and 60-70% relative humidity (RH) of ambient air. For a given flow rate operated in transient load conditions, the flow area was not found influential on the overall fuel cell performance whereas, a high aspect ratio was found to support the cell performance attributing to better air dissolution at the membrane electrode assembly (MEA) [41]. Also, the too high aspect ratio can lead to large mechanical stress which must be avoided. The land/channel ratio and the bending angle of the cathode channel were also found to influence the cell performance for open-cathode PEMFC in addition to the variation of width and depth of the channels. The land/channel ratio showed different effects at high versus low current density operations pertaining to different opening rates. Also, a large land/channel ratio was found to worsen the cell performance overall [42]. The open-cathode channel dimensions were also found to affect the pressure drop imposed on the airflow, whereas the smallest dimension (width and depth) had the highest pressure drop as compared to other dimensions for the same cathode air flow rate [43].

The open-cathode PEMFC systems operate on ambient air and are inherently affected by ambient air quality, including temperature and humidity. Zeyoudi *et al.* studied the

operation of such systems in the condition of the United Arab Emirates (UAE) and found the cell performance to be majorly affected by seasonal weather conditions. Hot and humid conditions in summer led to higher performance whereas hot and arid conditions resulted in membrane dry out [44], with lower performance during winter conditions at a lower temperature. Similar findings have been reported for Saudi Arabia's condition by Alanazi *et al.* [45]. The increment of cell temperature is theoretically thought to have a positive impact on the cell performance, however, for an open-cathode system, the power density of an eight cells assembly was found to decrease with increasing ambient temperature [46]. This reduction in cell performance was attributed to the high reaction heat generation which leads to dehydration in the fuel cell causing increased ohmic resistance, unlike conventional fuel cell systems. The airflow rate and hydrogen humidification levels were also found detrimental to forced air-convection PEMFC stacks [47]. On the other hand, high hydrogen humidity has been found to inhibit the cell performance of such systems at higher current density as an outcome of water flooding and pore blockage due to high reaction rates [48]. Additionally, the increase in hydrogen pressure for a 3-cell 50 cm^2 active area open-cathode stack helped increase the stack performance up to a cutoff pressure of 50 kPa, beyond which the cell performance remained stable with no significant improvement. The H_2 humidity level was also not found highly contributing to the overall cell performance with a minimal performance improvement for 100% humidified gas as compared to dry H_2. The effect of input temperature of H_2 was however found to vary for the single-cell performance as compared to the 3-cell stack performance. The performance of the 3-cell stack increased first and then reduction was observed with temperature increase, however, the single-cell performance kept on decreasing with an increase in H_2 inlet temperature [49].

Limitations and challenges

The open-cathode PEM fuel cell systems utilize ambient air as an oxidant as well as coolant directly onboard. The ambient air quality thus greatly affects the performance of such systems. Their performance is lower than for conventional systems [50] because of numerous factors involved in the design and operation of the cell. The temperature and RH of ambient air are highly impactful to the overall cell performance as it decides the operational environment of a fuel cell which decides the characteristic of the cell performance. The RH inside a fuel cell is decided based on the humidity of the input air

and temperature levels of the stack being operated [51]. The airflow rate at which the cell operates is also decisive of the overall performance, whereas excess airflow can lead to drying and deficient airflow can lead to liquid water flooding and impeded oxygen mass transport [46]. The fan/blower being used for such systems is often modulated to meet the different flow rates required as per the operating current densities. The usage of the air filter before the open-ended cathode inlets is useful in trapping the unwanted dust particulates which can inhibit the MEA performance and also block the airflow [52]. The open-cathode systems are generally limited to serving low to mid-range power applications up to 5 kW which can be cooled by the air stream. Above this range, the demand for cooling is difficult to meet by air as a coolant thus restricting the open-cathode stacks to operating at low power requirements.

1.4 MEA design effect in PEMFCs

Gas diffusion layer

GDL also called the backing layer is a macroporous carbon structure used as an interconnecting layer between the bipolar plate and the electrode [53]. This layer is porous in nature and allows the gas to pass through it providing a modulated pathway onto the catalyst layer. The GDL is electrically and thermally conductive and is an integral part of the overall thermal and water management in a PEM fuel cell [54]. The GDL is an asymmetric material and possesses different material properties in different directions [55]. The reduced thermal gradient within a GDL which is suitable for long durability is favored by high electrical and thermal conductivity [56]. The heat transfer resistance to the porous GDL is dependent on the fiber-fiber contact point which depends on the porosity of the layer [57]. The decrease in porosity was found to result in a decrement in thermal and electrical resistance [58]. On the other hand, the gas permeability and diffusivity are negatively impacted by lowering the porosity [59-60], which consequently reduces the oxygen availability at the cathode catalyst layer (CCL). The structure of GDL, porosity, fiber geometry and compression are among the factors influencing gas and water transport in the fuel cell [47–51]. The MPL is often used with a GDL to support water management in a fuel cell which is a carbon-based layer with polytetrafluoroethylene (PTFE) treatment on it [61]. The pictorial depiction of GDL and MPL microstructure is presented in Figure 5. The amount of PTFE used in an MPL decides the level of water accumulation and

hydration of the polymeric membrane [62-63]. The microstructure of the GDL and MPLs are studied using techniques like scanning electron microscopy through which analysis in terms of layer thickness, fiber orientation, smoothness of different layers, and PTFE bonding can be revealed [55–60], [64]. Nowadays, X-ray computed tomography has been widely used to study the three-dimensional structure of GDL layers which is a non-destructive technique and reveals data in terms of porosity, tortuosity, and pore size [65-66]. *In-situ* 3D structure is analyzed by image processing techniques [67].

GDL thickness and porosity are crucial to the overall performance of an open-cathode system. The effect of GDL porosity while operating at different open-cathode conditions is found to influence the overall cell performance to a greater extent against the GDL thickness changes [68]. Increased GDL bulk density with reduced porosity has been reported for favored ohmic resistance and current density in such dry operating environments. Low cathode charge transfer resistance possessed by less porous GDL was observed in such studies. In an open-cathode system, the water diffused on the cathode GDL is actively removed by the convective flow of air on the cathode side. Alternatively, due to back-diffusion, the water diffuses to the anode side via the membrane and humidifies the dry hydrogen. Thus, the material property of anode GDL in terms of porosity and PTFE content becomes equally important for effective water transport in the system. Conclusively, the combined effect of anode and cathode GDL and their individual properties determine the overall cell performance [69].

The conventional use of PTFE as a hydrophobic binder in a GDL/MPL has been used widely to facilitate better water management at high current densities [70]. However, some recent trends have shown the usage of a multilayer GDL/MPL with hydrophobic and hydrophilic properties for much more efficient water transport across MEAs preferably for low humidity cathode operations. [71-72]. The use of internal hydrophilic MPL has been suggested as an internal humidifier due to its water absorption capability [73]. The thickness, porosity, and permeability of MPL are found to be influencing the thermal and water management of the entire cell similar to the backing layer. The addition of MPL helps in maintaining a uniform thermal gradient across the fuel cell and thereby adding to the overall performance [74].

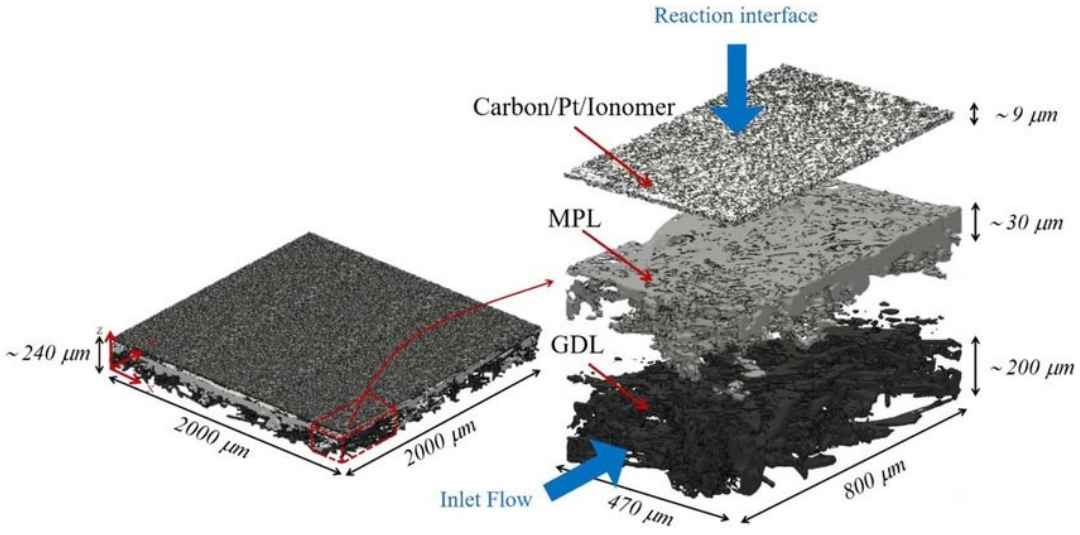

Figure 5. Schematic of GDL/MPL microstructure in a PEMFC. "Reproduced with permission from [75] © The Author(s) 2019. Published by ECS under the terms of the Creative Commons Attribution 4.0 License."

Catalyst layer

The CL is the three-phase boundary layer where the membrane phase, gas phase, and solid electrode phase co-exist to facilitate electrochemical reactions [76]. The anode catalyst layer (ACL) and CCL usually have similar structure and composition although the cathode has higher catalyst loading and more influence on cell performance due to sluggish ORR [77–80]. There are primarily two ways of CL preparation based on the substrate at which the catalyst ink is coated. The catalyst coated membranes (CCMs) are prepared by coating catalyst ink on both the sides of the polymeric membrane using various techniques. Whereas the gas diffusion electrodes (GDEs) are manufactured by directly depositing the catalyst ink on to the GDLs. A MEA is subsequently prepared by either hot pressing two GDLs and the CCM in between or the GDEs and the PEM in the other approach.

Several methods listed below are used widely for preparation of these fuel cell electrodes.

- Ultrasonic spraying – This technique is widely used at laboratory scale for preparation of CLs. Ultrasonic waves are used to atomize the catalyst inks into uniform droplets which are sprayed to membranes/GDLs with the help of shaping

air. Thin films of CL are formed by heating and volatilizing the solvents used to prepare the catalyst inks in this process [81-82].

- Electro spraying – In the process of electro spraying, the catalyst ink droplets are first charged through a high-voltage electric field and then ejected in the form of aerosol which gets deposited at the substrate. The flow rate and DC voltage are some crucial parameters which decide the quality of coating overall [81-83].
- Inkjet printing – The inkjet printing (IJP) is a digital printing method where the catalyst ink droplets are precisely deposited in different patterns on the substrate without any physical contact. There are two different ways of inkjet printing which are used widely, the continuous inkjet printing method which uses the continuous flow of liquid being ejected from a nozzle due to surface tension. In the other process called as drop-on-demand IJP the ink ejection required for printing through the nozzle is on-demand [82].
- Screen printing – In this technique, the catalyst ink is printed over a mask layer which is usually a porous surface that further allows to transfer the layer on the desired substrate in order to generate the desired coating pattern. In the process of printing, a screen frame is applied above the substrate surface and a squeegee is swept across the screen after loading the catalyst ink onto the screen. The screen is separated from the substrate once the solution is applied through the screen onto the surface of the substrate. Finally, after drying a homogeneous electrode film is obtained in the process [81-82].

The catalyst ink is generally composed of carbon-supported catalyst, along with an ionomer and suitable solvent for slurry dispersion [84]. The method of catalyst coating and composition of slurry ink decides the overall microstructure of the CL. The material properties of the CL like the catalyst activity, porosity, permeability, and thermal and electrical conductivity determine the overall rate of reaction taking place at the CL which decides the cell performance. The use of a thicker catalyst layer is shown to have more stable cell performance at high temperatures with the use of a low % Pt/C catalyst by holding more water at the CCL and thus maintaining higher humidity. On the other hand, thicker CL results in high mass transfer resistance and ohmic resistance leading to low performance for an open-cathode PEMFC [85]. The CL comprises of solid region distributed volumetrically along with voids, and the optimization of solid to void ratio

determines overall cell performance at given operating conditions [86]. The solid network of Pt/C facilitates the transport of e^- whereas the ionomer phase is responsible for the H^+ transport to and from the electrocatalyst and the void region in the CCL is responsible for oxygen transport and H_2O transport as shown in Figure 6. The mass transport limitations in the cell are primarily caused by O_2 concentration polarization which is dependent on the CCL thickness and porosity for gas phase transport as well as diffusion through the ionomer thin film and/or water at the catalyst particles. A decrement in CL porosity was reported to enhance mass transport losses, however, the charge transfer resistance for the ORR was not found to increase [87]. The ionomer phase in the CCL is responsible for protonic conduction which contributes to the overall ohmic losses. The ionomer/carbon (I/C) weight ratio thus quantifies the optimal hydration level and protonic resistance in the system. At low humidity conditions, a high I/C ratio (≥ 0.6) has been found to optimally balance the low hydration levels in the cell for conventional liquid-cooled PEMFC [88]. The low ionomer presence at the CL can significantly decrease the proton transfer and inhibit the electrochemical reaction, whereas excess ionomer can cause water flooding and decreased electrochemically active surface area (ECSA) which can lead to severe performance drop [89]. The rate of ORR is also affected by the thickness of the ionomer layer at the CL and is indirectly dependent on the dispersion of the ionomer on Pt/C [90-92]. At low RH conditions and while operating at high current densities, the protonic resistance across the CL becomes a limiting factor for performance and catalyst utilization. At similar Pt loading and I/C ratio, the catalyst with higher ECSA was found to perform better at high RH conditions, whereas at dry conditions, due to increased protonic resistance even the high ECSA catalyst gave inferior performance [93].

The equivalent weight (EW) of an ionomer is defined as the weight of dry polymer per mole of the acid group present in its dry resin form [94]. It has been observed that the water sorption increases with a decrease in EW and an increase in the sorption temperature [95]. The EW of ionomer has also been reported to influence the overall cell performance for PEM fuel cell operations. The cell hydration was found to be improved possessing lower mass transport resistance with the use of high EW ionomer for the dry operation of air-cooled, open-cathode PEMFCs [96] as compared to low EW ionomers determined by electrochemical impedance spectroscopy studies. On the contrary, CLs with short side chain (SSC) ionomers were found to achieve high performance for high humidity (100%) as well as moderate humidity (50%) operating cases at 80^0C referring to

the different ionomer backbone structures present in SSC unlike long side chain (LSC) ionomers [97]. Comparative studies of SSC and LSC ionomers being used at the same operating conditions have shown SSC exhibit higher ECSA, O_2 transport resistance, double-layer capacitance, and protonic conductance as compared to LSC. Also, the O_2 mass transport resistance was found to decrease with an increase in RH for both types of ionomers primarily due to higher water content at the Pt/ionomer interface [98-99].

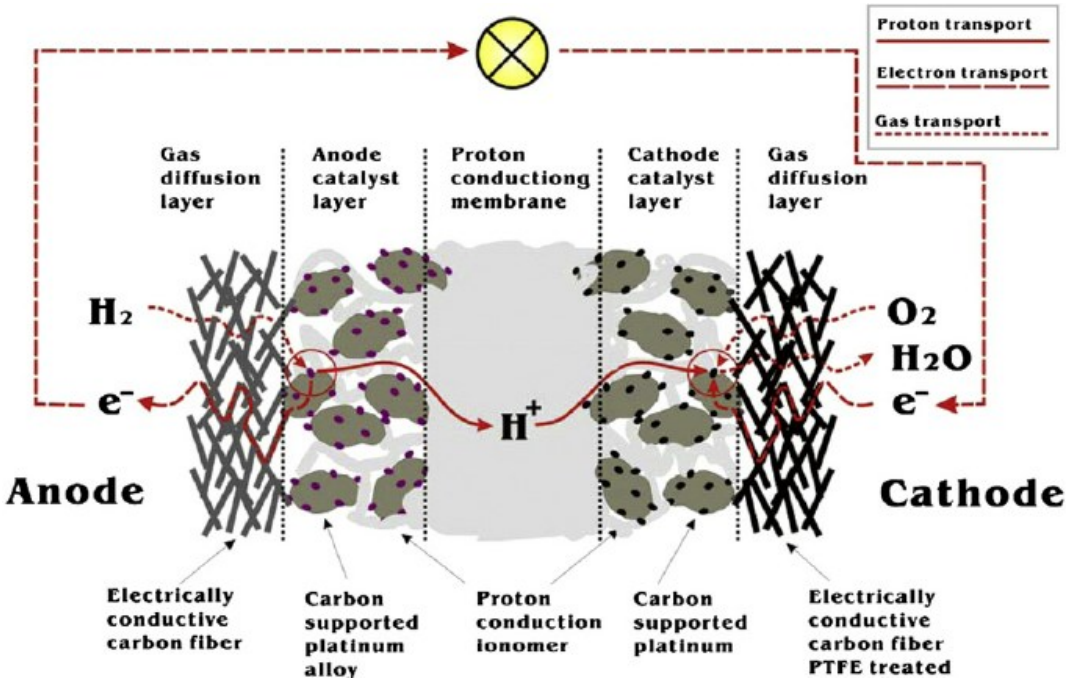

Figure 6. Schematic of oxygen and water transport at the MEA level of a PEMFC. "Reproduced with permission from [100] **© 2021 Elsevier Science & Technology Journals; permission conveyed through Copyright Clearance Center, Inc."**

Membrane

The typical membrane for PEMFCs is desirable to possess high ionic conductivity with the least hydrogen cross-over and negligible electron transport across its bulk phase. Also, the thermal, chemical, and mechanical stability of the membrane is of key importance for the smooth operation of PEMFCs [101]. Perfluorosulfonic acid based membranes are the standard membrane type used for fuel cells operating below 100 ^oC. The hydrophilic sulfonated side chain is responsible for water absorption whereas the perfluorinated backbone is hydrophobic and provides mechanical support [102]. Dupont's Nafion® is the most widely used membrane to date for PEMFCs. Nafion® offers high durability of above

60,000 hrs. and possesses high chemical stability along with high protonic conductivity. Also, it requires higher humidification for protonic conduction and has a high manufacturing cost [95–99]. Competing for these challenges, Dow company and Solvay have come up with SSC membranes offering higher crystallinity, and higher protonic conduction at higher glass transition temperatures than Nafion® [103]. The use of composite membranes is getting wider acceptance recently since the release of e-PTFE reinforced membrane by Gore and Associates which offer higher mechanical stability as compared to conventional PFSA membranes with thinner PEMs [104]. Various literature has also shown progression towards the use of hygroscopic inorganic materials as fillers used in the polymer matrix for enhanced water transport [95]. Liu *et al.* [105] have shown the benefits of using thinner Nafion® 211 membrane as compared to Nafion® 212 membrane for forced-convection PEMFCs however the detailed understanding of suitable selection of membrane materials for open-cathode PEMFCs are required for better understanding of the technology and its limitations.

1.5 PEM fuel cell modelling

The use of modelling and simulation has been pursued extensively by various researchers and scientists in PEMFCs to minimize the longer experimentation time and financial implications related to these trials. The fuel cell modelling also helps to bring insight into physical variables like monitoring pressure, temperature, humidity, concentration, etc. distribution inside the cell/stack which is not possible to be estimated from most of the characterization techniques available [106]. Fuel cell modelling has been carried out for decades since fuel cell research has been taking shape. Initially, the fuel cell models were limited to zero-dimensional, one-dimensional, or two-dimensional models and were limited in covering the multiphysics coupling, primarily the water and thermal management in fuel cells. One of the reasons is the computational power limitations along with less understood phenomena and theories established for PEMFC operation and its challenges. Some of the earlier prominent works involved the development of one-dimensional, MEA isothermal models [107-109], quasi-two-dimensional models [110], two-dimensional models without electrodes assuming the ultrathin dimension of such electrodes, a thermal effect demonstrated in fuel cell model [111-112] and addressing water flooding in PEMFCs [113] using a 1-D model. Most of the earlier models use various simplifications because

of the limited numerical techniques available and were analytic in nature. Gradually, the usage of computational fluid dynamics (CFD) was applied to fuel cell modelling with two-phase flow [105-106]. Later, research groups developed non-isothermal, three-dimensional fuel cell models [114] along with the inclusion of multi-phase flow and phase change [115]. The modelling and simulation have helped in understanding various physical phenomena with a focus on water and reactant transport in gas channels and GDLs [110-112]; the effect of MPLs [116]; water transport in the membrane [114-115], [117-118], the influence of CL microstructure on cell performance [119-120], geometrical effects of various components [121-122] and non-isothermal operation and thermal management [123-124], to name a few representative contributions.

The recent trends in modelling and simulation also involve performance models featuring start-up and cold start dynamics [125-126], dynamics of channel flow [119], [120], [127], and transient models of entire MEAs and cells [128-129]. Anode impurity and corrosion studies are among the areas covered by degradation models in the literature [123-124]. A keen interest in microscale and mesoscale modelling has also emerged in recent years along with a focus on molecular modelling and quantum mechanical models [129-133]. The various techniques involved in modelling of PEMFCs based on different lengths and time scales use a continuum based macro-scale approach, Lattice-Boltzmann Method, Molecular Dynamics, Dissipative Particle Dynamics, Density Functional Theory, and Quantum Mechanical electronic structure methods [106].

The modelling of an open-cathode system has been limited in the literature. A two-dimensional model was developed to investigate the impact of fan power, orientation, and operation of fans in blowing and suction mode and pressure drop on the cell performance [37], [134-136]. A numerical model depicting thermal analysis of an open-cathode system [137-139] and a full cell-level thermal characterization were predicted along with the impact of airflow rate and in-plane thermal conductivity of bipolar plate on the overall cell performance [139-140]. The concept of electro-thermal performance mapping using temperature and current distribution data collected by inserting sensors across the cell concluded that at low current, the current density distribution is guided by the reactant consumption gradients, whereas at high current, the cell temperature is found to dominate the current density distribution [141-143].

Objectives and Scope

The operational behavior of open-cathode PEMFCs is sparsely available in the literature which motivated us to do an in-depth study of the system by undergoing various experiments to study the impact of ambient conditions on the overall state of the cell and its performance. A modelling approach is followed by developing a robust 3D model integrated with thermal, performance, and water transport sub-models which is a shortfall in this research area. The present study focuses on using a computational modelling approach to understand the transport phenomena occurring in an open-cathode system and further analyze its operational behaviour at different operating conditions. The limitations in terms of high ohmic losses due to drying and slower kinetic rate because of the ambient operational regime are established which were not clearly demarcated in previous research. The model once validated with experimental results is considered a guiding tool to investigate design changes at the component level of the open-cathode system which helps in bringing down the limitations towards cell performance of such systems. Individual component selection and design are key to the development of high-performing open-cathode systems. Emphasis on articulating the strategic ionomer design along with proper MPL selection is a potential gap in the literature which is addressed by proper changes made at the design level. The overall MEA design with proper loading and CL porosity is also found to add to the cell performance of such systems. The individual effect of design variables along with their interaction effect is also studied using the DoE tool with computational results as an input. Finally, a set of experiments are performed to demonstrate and validate the trends of modelling results obtained.

Chapter 2.

Materials and methods

2.1 Modelling details

The 3D computational fuel cell model is developed using the finite element analysis based computational software COMSOL Multiphysics 5.4. The model is non-isothermal and is developed for obtaining steady state solution primarily for the open-cathode cells, however, it can also be used for liquid-cooled cells by changing certain boundary conditions (BCs). This has been explained and validated in subsequent sections. Out of a bigger stack, the central channel of the central cell is simulated in this study following the periodic approximation. Taking symmetry of the fuel cell geometry into account, half channel, and half rib parts on each side of the 5-layered MEA are resolved and considered as the computational domain, as depicted in Figure 7(a). The channels and ribs are a part of the graphitic bipolar plate which supports reactant flows as well as provides electrical conductance to the electrons generated. The MEA consists of GDLs and CLs on both sides of the polymeric membrane termed anode and cathode respectively. The cell-to-cell temperature gradients and the lateral temperature gradients are neglected in the study considering all the cells to have an identical core temperature. These assumptions are made for the benefit of reduced computational cost achieving a predictive trend at the cell level. Figure 7 represents the computational domain with a polymeric electrolyte membrane sandwiched between flow channels, gas diffusion layers, and catalyst layers on both sides. Table 1 describes the dimensions of the various domains of the 3D computational geometry. Extensive details in terms of mesh type, solver details, and parametric details have been provided in Appendix A.

(a)

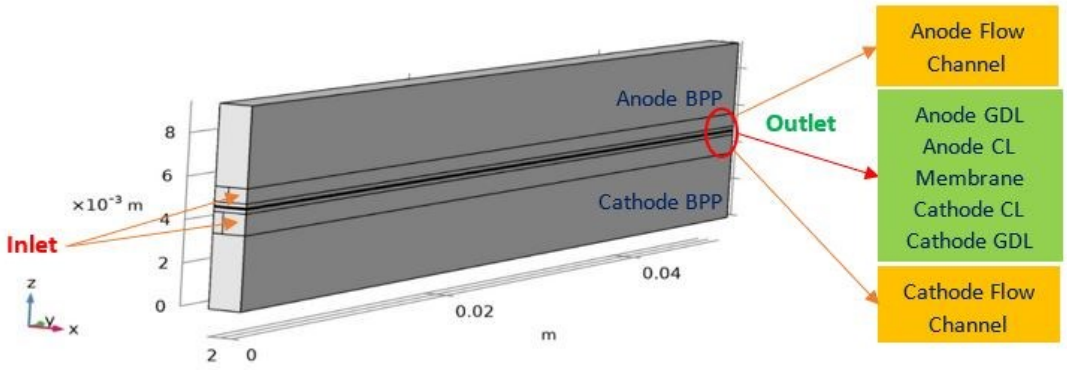

(b)

$\dot{V} = \dot{V}_{in,a}$ P = 1atm

$x_{H_2,in} = 1 - \frac{P_{sat}}{P_{in,a}} \times RH_{anode}$ x : Outflow

$T = T_{in,a}$ T : Outflux

	Anode BPP	**I**
II	**Anode FF**	
	Anode GDL	**III**
IV	**Anode CL**	
	Membrane	**V**
VI	**Cathode CL**	
	Cathode GDL	**VII**
VIII	**Cathode FF**	
	Cathode BPP	

$\dot{V} = \dot{V}_{in,c}$ P = 1atm

$x_{O_2,in} = 0.21 * (1 - x_{H_2O,in})$ x : Outflow

$x_{H_2O,in} = \frac{P_{sat}}{P_{in,c}} \times RH_{cathode}$ T : Outflux

$T = T_{in,c}$

II- VII are the internal interfaces between the different layers from top to bottom

I, VIII - Periodic BC: $T_{top,anode\ side\ BPP} = T_{bottom,cathode\ side\ BPP}$

II- VII - x : No flux; T : No flux

II - $V = 0\ V$; VII - $V = V_{cell}$

Figure 7. (a) 3D schematic of the computational domain used for modelling. (b) BCs used for modelling.

Table 1. Dimensions of the open-cathode single cell used for 3D modelling.

Open-cathode cell			
	Dimension		
Domain	Length (mm)	Width (mm)	Height (mm)
Flow Channel (Anode/Cathode)	50	0.825/1.0	0.7/1.0
GDL (Anode/Cathode)	50	1.425	0.19
CL (Anode/Cathode)	50	1.425	0.015
Membrane	50	1.425	0.05
Ribs (Anode/Cathode)	50	0.6/0.425	0.7/1.0
Bipolar plate (BPP)	50	1.425	3.8/3.5

The present model consists of several governing physics which apply to both liquid-cooled cells and open-cathode PEMFCs. The mass conservation equation (5) is solved in conjunction with Navier- Stokes equation (6) in the whole of the computational domain except the membrane and rib area of the bipolar plate. The convection-diffusion equation (7) solves for the transport of H_2 and H_2O on the anode side which is dependent on the anode inlet RH, whereas on the cathode side, the gaseous mixture of air and H_2O is solved with cathode inlet RH as the BC. Here, 'ρ' is the mixture density, 'u' is the velocity vector, 'S_{mass}' is the mass source term, 'P' is the pressure, 'μ' is the kinematic viscosity, 'S_{mom}' is the momentum source term, 'c_i' is the molar concentration of each chemical species, 'D_{eff}' is the effective gas diffusivity, and 'S_{mol}' is the molar source term for generation/consumption of different species in the respective domains.The local distribution of potential is solved by the charge conservation equations (8), (9) which have grounded cell voltage and actual cell voltage as BCs at the respective current collectors. Both these equations are solved simultaneously at the porous electrodes (GDLs and CLs) where 'σ_s' is the electrode electrical conductivity and 'σ_m' is the electrolyte phase ionic

conductivity. 'ϕ_s', 'j_s' are the electrode potential and current density, whereas 'ϕ_m', 'j_m' are the electrolyte potential and current density respectively. The overall water transport in the fuel cell is governed by the two-phase water transport, including the vapour phase and ionomer phase, whereas liquid water is neglected. Liquid water production is not considered in the present work because of the relatively lower relative humidity and low current density operation in the open-cathode systems in contrast to conventional liquid-cooled systems [143-144]. The implication of this assumption is for cases where the current density is too high and excess amount of water is generated at the cathode side which can lead to flooding. Although in open-cathode since the air flow rates are relatively higher in most of the operating cases, the accumulation of water in the channels are less likely. The species conservation equation (7) includes the distribution of water in the vapour phase in the system, whereas equation (10) solves the water transport in the ionomer phase. The water balance is governed by (10) where 'n_d' is the electro-osmotic drag coefficient, ' j_m' is the electrolyte current density, 'D_d' is the back-diffusion coefficient, 'S_d' is the source term, ' F' is the Faraday's constant and 'C_d' is the net water concentration in the dissolved phase. The water produced at the CCL is considered in vapour phase in Appendix A, thereafter the water production is considered in the ionomer phase or dissolved phase in subsequent work from Appendix B to D. The thermal heat distribution inside the cell is governed by the conduction-convection heat equation (11) in all parts where 'T' is the local temperature, 'C_p' is the specific heat of the fluid, 'k_{eff}' is the effective thermal conductivity, and 'S_T' is the heat source term which constitutes heat generation inside the cell via entropic heat of reaction, irreversible heat of electrochemical reactions, and heat dissipation due to ohmic losses. The phase change from the dissolved phase to the gas phase and vice versa at the ACL and CCL is incorporated in the 'S_T' itself and is determined by the mass source term multiplied by the enthalpic heat [145-146]. The water transport from gaseous phase to dissolved phase and vice versa is guided by the overall concentration gradient and water sorption/desorption rate constant (γ).

$$\nabla.(\rho u) = S_{mass} \quad \textbf{(5)}$$

$$\rho u.\nabla u = -\nabla P + \mu\nabla^2 \mathrm{u} + S_{mom} \quad \textbf{(6)}$$

$$u.\nabla c_i = \nabla.\left(D_{eff}\nabla c_i\right) + S_{mol} \quad \textbf{(7)}$$

$$\nabla.(\sigma_s \nabla\phi_s) = -j_s \quad \textbf{(8)}$$

$$\nabla.(\sigma_m \nabla\phi_m) = -j_m \quad \textbf{(9)}$$

$$\nabla.(-D_d\nabla C_d) + \nabla.\left(\frac{n_d}{F} j_m\right) = S_d \quad \textbf{(10)}$$

$$\rho C_p u.\nabla T = \nabla.\left(k_{eff}\nabla T\right) + S_T \quad \textbf{(11)}$$

The various assumptions considered for modelling the fuel cells are listed below:

1. The flow is incompressible and laminar because of the low Reynolds number.
2. The gaseous mixtures are assumed to be an ideal gas mixture.
3. The polymeric membrane is assumed to be impermeable and thus crossover of fuel from the anode to the cathode side is assumed negligible.
4. The interfacial resistances are considered minimal and hence neglected.
5. The formation is water is considered in gaseous form and the transport of water is considered only in gaseous and dissolved phase forms; the liquid water transport is neglected.

Table 2. List of parameters used for the 3D computational modelling.

Physical Property	Value	Units
Dynamic viscosity at anode	9.5×10^{-6}	Pa s
Dynamic viscosity at cathode	1.96×10^{-5}	Pa s
GDL Porosity	80	%
GDL Permeability	1.9×10^{-12} (IP) / 7.0×10^{-12} (TP)	m^2
CL Porosity	30	%
CL Permeability	1.0×10^{-14}	m^2

CL electrical conductivity	450	S m^{-1}
GDL electrical conductivity	17500 (IP) / 230 (TP)	S m^{-1}
Electrolyte volume fraction	0.2723	
Binary diffusion coefficient of H_2-H_2O	0.915 x10^{-4}	m^2 s^{-1}
Binary diffusion coefficient of N_2-H_2O	0.256 x10^{-4}	m^2 s^{-1}
Binary diffusion coefficient of O_2-N_2	0.22 x10^{-4}	m^2 s^{-1}
Binary diffusion coefficient of O_2-H_2O	0.282 x10^{-4}	m^2 s^{-1}
Exchange current density at anode electrode	50	A m^{-2}
Exchange current density at cathode electrode	1.2 x10^{-4}	A m^{-2}
Effective platinum surface area ratio (e_l)	0.6	
Platinum loading (m_{Pt})	0.5	mg cm^{-2}
Specific active area of platinum (S_{Pt})	30	m^2 g^{-1}
Charge transfer coefficient	0.5	
Thermal conductivity of fluid at anode	0.18	W m^{-1} K^{-1}
Thermal conductivity of fluid at cathode	0.03	W m^{-1} K^{-1}
Heat capacity at constant pressure of fluid at anode	1.44 x10^4	J kg^{-1} K^{-1}
Heat capacity at constant pressure of fluid at cathode	1.01 x10^3	J kg^{-1} K^{-1}
Ratio of specific heats of fluid at anode	1.41	
Ratio of specific heats of fluid at cathode	1.4	
Thermal conductivity of porous matrix GDL	21 (IP) / 0.5 (TP)	W m^{-1} K^{-1}
Thermal conductivity of porous matrix CL	1.5	W m^{-1} K^{-1}
Density of porous matrix GDL	2.2 x10^3	kg m^{-3}

Density of porous matrix CL	2.2 x10^3	kg m^{-3}
Specific heat capacity of porous matrix GDL/CL	1.05 x10^3	J kg^{-1} K^{-1}
Thermal conductivity of solid membrane	1.5	W m^{-1} K^{-1}
Thermal conductivity of anode/cathode BPP	75 (IP) / 30 (TP)	W m^{-1} K^{-1}
Density of solid membrane	1.98 x10^3	kg m^{-3}
Density of anode/cathode BPP	1.78	g cm^{-3}
Heat capacity at constant pressure of solid membrane	4.197 x10^3	J kg^{-1} K^{-1}
Heat capacity at constant pressure of anode/cathode BPP	0.71 x10^3	J kg^{-1} K^{-1}

The computational model uses parameters listed in Table 2 and is designed to calculate the average current density at the given operating cell voltage. The three primary voltage losses namely the activation, ohmic, and mass transport losses are further deduced using (12), (13), and (14). η_{MT} is calculated after deducing the V_{cell} from the model and empirically calculated η_{act} and η_{ohmic}. 'V_{cell}' denotes the overall cell voltage, 'OCV' is open circuit voltage, '$\eta_{act,anode}$' is the activation overpotential on anode, '$\eta_{act,cathode}$' is the activation overpotential on cathode, 'η_{ohmic}' is the ohmic overpotential, 'η_{MT}' is the combined mass transport overpotential at the anode and cathode, 'R' is the gas constant, 'T' is the cell temperature, 'α_i' is the charge transfer coefficient at the i^{th} electrode, '$i_{0,i}$' is the exchange current density at the i^{th} electrode, 'i' is the operating current density, 'I' is the operating current, and 'R_{ohmic}' is the ohmic resistance.

$$V_{cell} = OCV - \eta_{act,anode} - \eta_{act,cathode} - \eta_{ohmic} - \eta_{MT} \quad \textbf{(12)}$$

$$\eta_{act} = \frac{RT}{\alpha_i F} ln\left(\frac{i}{i_{0,i}}\right) \quad \textbf{(13)}$$

$$\eta_{ohmic} = IR_{ohmic} \quad \textbf{(14)}$$

2.2 Experimental details

This section describes the experimental scope of this work which is performed to validate the various findings from the computational simulations performed over a wide range of operating parameters and cell design. A single cell test architecture is setup to perform model validation as described in Appendix A, B, and C. Also, the design strategies of best MEA at the component level as obtained in Appendix B and C from the computational model are verified using the same single cell test architecture by performing various in-house tests described in Appendix D. These tests are performed at the Fuel cell testing lab, Indian Oil R&D Centre, and are carried out in an environmental chamber at the centre using an in-house developed single-cell setup and in-house coated MEAs. A detailed description of the experimental setup, operating conditions, MEA fabrication, and test protocols are described subsequently.

Experimental setup

The experiments were performed using 25 cm^2 single-cell hardware which was developed in-house. The setup contains a duct for the supply of ambient air to the open-cathode channels and thermocouples to monitor temperature at various positions. The single-cell consists of an anode flow plate with serpentine channels, a cathode flow plate with parallel channels, in-house coated CCMs and GDLs. The channel dimensions along with the thickness of other cell components are provided in Table 1. The cell is supported by gold-plated current collectors on both sides to draw current and monitor the cell voltage. The cell hardware further consists of an endplate on both sides and gas inlet and outlet ports. A PA 2200 Nylon based duct is 3D printed and integrated with the single-cell setup to provide the air flow for cooling as well as acting as the reactant flow for the cell operation. The open-cathode setup is tightly wrapped from all sides using glass wool to thermally insulate it for better results. The cell compression is performed manually by torque wrench by applying optimal torque of 4 N/m to each of the four-cornered bolts of the hardware. The whole setup is shown in Figure 8. The MEA used for model validation consists of a Nafion® NRE-212 membrane coated with 60% Pt/C catalyst with effective loading of 0.5 mg/cm^{-2} and ionomer loading of 30% (wt/wt %) on both sides supported by a Sigracet 29BC GDL. The extensive experimental portion of the thesis is presented in Appendix D with details of various CCMs being tested, the scope of testing, the preparation method of MEAs, and results obtained from those testing.

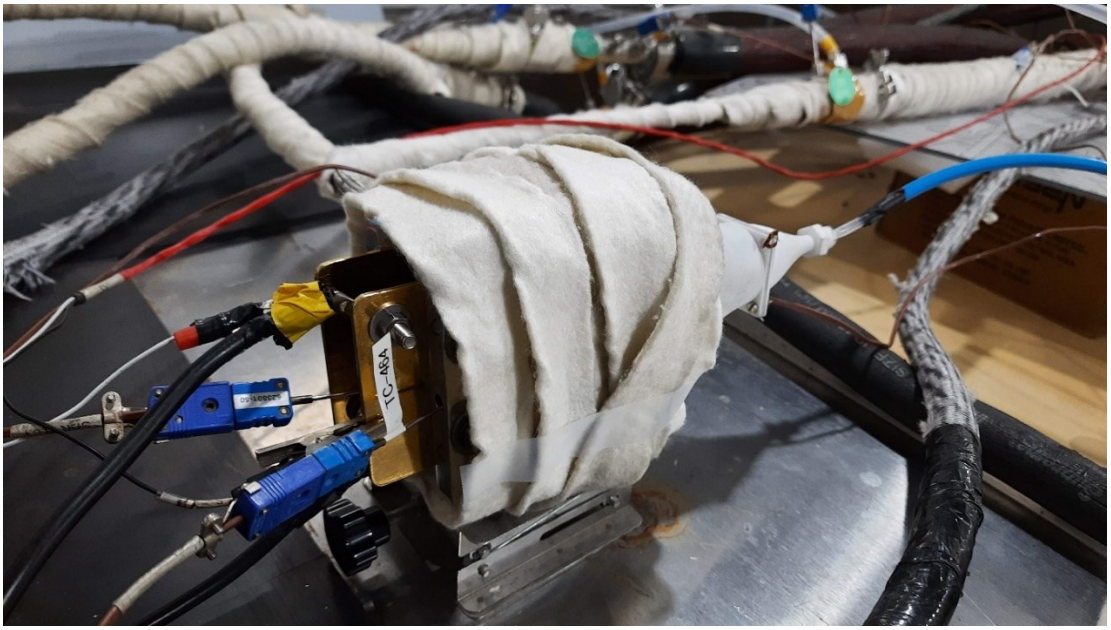

Figure 8. Experimental setup of single-cell open-cathode PEMFC.

Test station details and conditioning of MEAs

The various MEAs prepared were first conditioned on a Greenlight Innovation G60 test station using a closed-cathode setup. In the closed-cathode setup, the open-channel cathode plate is replaced by a closed cathode plate having parallel channels with the same active area, and the airflow onto the cell is in a conventional pressurized form. The conditioning step includes end-plate heaters on both sides for heating the cell hardware to maintain a constant cell temperature. The G60 test station shown in Figure 9 is a fully automated testbed for testing PEMFCs up to 1 kW and is equipped with humidifiers on anode and cathode gas lines to maintain controlled humidity levels. The temperature is also monitored at the inlet and outlet and can be maintained as per user input. The current and voltage sensors are provided to measure these data up to two decimal points accuracy. For the conditioning step, the MEAs were put to fully humidified conditions on both the anode and cathode sides with inlet RH in the range of 95-100%. The inlet gas temperature and cell temperature were maintained at 60^{o}C. The conditioning procedure involved holding at constant current (at 0.6 V) for 6-8 hrs followed by three cycles of polarization (OCV to 0.3 V) and 100 cyclic voltammetry (CV) scans at 50 mV/s. This conditioning procedure was repeated three times for each MEA to get the final conditioned

MEA for further testing and evaluation. The anode flow rate was maintained at 0.5 normal liters per minute (nlpm) and the cathode flow rate at 2.5 nlpm for the conditioning step.

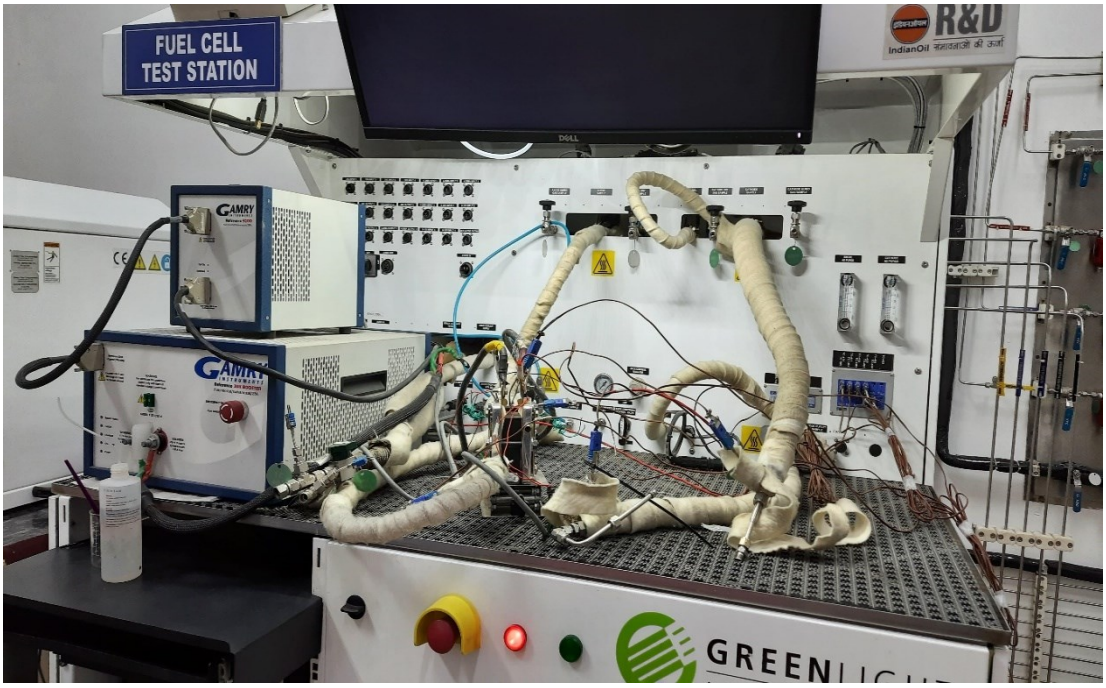

Figure 9. Greenlight Innovation G60 fuel cell test station setup at IOC R&D Centre.

Test protocols

Single cell fuel cells with fully conditioned MEAs were tested on a Greenlight Innovation G400 test station for open-cathode testing conditions. The G400 test station has similar features as a G60 test station and is capable of testing larger stacks up to 10 kW. The G400 is used for testing open-cathode cells since it is attached to an environmental chamber that can maintain ambient temperature and humidity, unlike the G60 test station. The *Espec* environmental chamber has the capability of maintaining temperature in the range of -30 ^{o}C to 70 ^{o}C and RH between 0-100%. A small air suction device is kept in the environmental chamber to suck the air and provide it to the open-cathode setup. A manually operated rotameter is attached to the outlet of the suction device so that the airflow can be controlled by the user while running tests for open-cathode setup.

For each of the MEAs, the open-cathode test data are recorded at 0.6 V and 0.4 V potentiostatic conditions. H_2 is supplied to the anode side using the G400 gas lines at a temperature of 40 ^{o}C and 60% RH with the flow rate of 0.5 nlpm. This RH condition is used

to mimic an actual dead-end operation mode for such systems [147]. The cathode airflow rate on the other side is maintained by adjusting the rotameter attached to the suction device at a fixed flow rate of 2.5 nlpm. The temperature and RH of the environmental chamber are maintained at 40 ^{o}C and 40% RH, respectively. Leak tests are performed using Swagelok leak detectors from the hose connecting the rotameter to the duct opening so that no leakage is ensured. The open-cathode setup is wrapped using glass wool to ensure that no heat is lost to the ambient and the self-heating of the cell can take place. At each of the cell voltages (0.6 V and 0.4 V), the system is kept in fixed condition for an extended time period to reach and ensure thermal equilibrium. The thermocouples TC1, TC2, and TC3 are inserted at the central open channel on the cathode flow plate, the center of the cathode flow plate thickness, and at the cathode end plate. The three temperatures are monitored continuously and once a thermal equilibrium is achieved; the fuel cell data are recorded for each fuel cell test. After recording the fuel cell data, the cell is allowed to cool down and the same procedure is followed to record the next set of fuel cell data for reproducibility. A total of three data sets are collected at both cell voltages for each MEA. Electrochemical impedance spectroscopy (EIS) scans are also measured after reaching thermal equilibrium in each cycle using a Gamry 3000 Reference potentiostat and Gamry 3000 booster for evaluating and diagnosing the membrane hydration and cell kinetics. EIS scans are measured using a frequency range of 1 kHz to 0.1 Hz with 10 points/decade at an alternating current (AC) with a root mean square (RMS) voltage of 10 mV.

Chapter 3.

Summary of Contributions

3.1 A computational analysis on the operational behaviour of open-cathode polymer electrolyte membrane fuel cells

The open-cathode PEMFC is the focus area of the dissertation work being presented here. The knowledge about conventional PEMFC systems which are based on liquid-cooling is sufficiently available in the literature covering the various aspects of such systems ranging from material selection, design selection, computational analysis, testing and durability studies, characterization studies, and system-level integration and handling to name a few. On contrary, the area of open-cathode PEMFC research and development is relatively new, and therefore understanding the architecture, operational behaviour, and its response to various operating environments is the motivation behind this study. The advantage of open-cathode PEMFCs over conventional PEMFCs in terms of smaller system design, easy operation, and lower cost are the driving force towards investigating these systems in detail and coming up with an efficient design [1-2]. The comparative system design of a conventional liquid-cooled PEMFC versus an open-cathode PEMFC is described in Chapter 1.3.

A computational approach is followed to understand the operational behaviour of open-cathode PEMFCs. A three-dimensional single-cell model is developed in COMSOL Multiphysics 5.4 to understand the dynamics of a PEMFC with various governing physics included in the model. The model includes the various transport phenomenon occurring at the cell level with the detailed coupling of mass transport, momentum transport, heat transport, species transport, and cell potential conservation infused with specific boundary conditions explained in Chapter 2 [148]. Using symmetric and periodic boundary conditions a full-scale multi-cell stack is reduced to a half-channel, half-rib along with GDLs, CLs, BPPs, and PEM fitting in that active area of the MEA. This helped in reducing the computational time and complexity of solving the problem. The geometry is developed in the COMSOL Multiphysics platform representing the computational domain for which the appropriate meshing is carried out and specific governing equations are assigned with initial conditions and BCs. The grid convergence studies are duly performed to ensure the

optimum mesh quality for the model to be solved. Boundary layers are created at the inlet, outlet and other flow domains to resolve flow separation issues. The model is solved to achieve a steady-state solution following certain approximations listed in Chapter 2. The model is subdivided into different study steps solving the individual governing equations in segregated steps followed by a coupled last step where all the governing equations are solved together. This approach helped in reaching faster convergence and the relative tolerance is kept at 10^{-3} for all the study steps. The model developed is a comprehensive PEMFC model with sub-models including the thermal model, water management model, and reaction kinetics model. The full-scale model developed can be used for any type of PEMFC by changing the BCs, and geometry as per the user requirements. The same model is used first for a conventional liquid-cooled PEMFC operating at fully humidified flow conditions to generate baseline data. A single-cell experimental setup is developed with an active area of 25 cm^2 with the capability of operating in liquid-cooled mode as well as in open-cathode mode by changing the cathode plates and insertion of an external duct-fan mechanism. The details of the experimental setup are presented in Chapter 2.2. Unlike operating in liquid-cooled mode, the open-cathode mode operation is performed by noting the fuel cell data after achieving a thermal equilibrium for each operating cell voltage. The modelling results are validated with experimental results by performing one set of liquid-cooled operating conditions using the liquid-cooled setup and a total of four open-cathode operating conditions with different ambient conditions as listed in Table 3 using an open-cathode single-cell setup. A good agreement between the experimental and simulation results is obtained with the standard deviation in error falling below 5% for each of the cases as shown in Figure 10(a).

Table 3. Operating conditions used for simulating open-cathode PEMFC performance.

		Anode		Cathode	
		RH (%)	T (°C)	RH (%)	T (°C)
Open-cathode cell	Case-1	15	30	30	30
	Case-2	15	30	90	30
	Case-3	15	50	30	50
	Case-4	15	50	90	50
Liquid cooled cell	Case-5	50	50	90	50
Isothermal case	Case-6	50	50	90	50

(a)

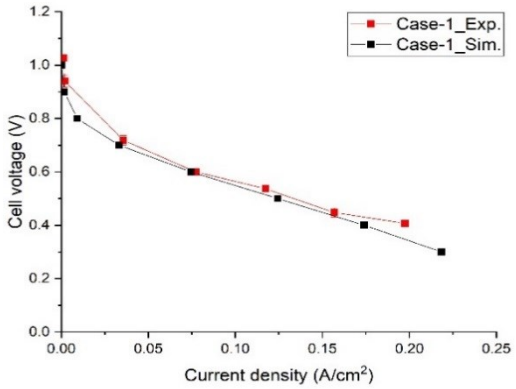

(b)

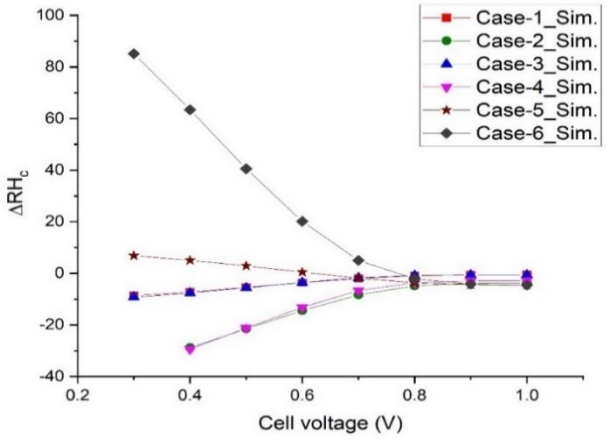

Figure 10. (a) Model validation result for case-1 and (b) RH difference between inlet and outlet in the cathode air flow as a function of cell voltage.

Overall, the liquid-cooled case showed higher cell performance than open-cathode cases as anticipated. Among the open-cathode cases, the highest cell performance is achieved at 50 ºC and 90% ambient humidity whereas the lowest performance obtained is at 50 ºC and 30% ambient humidity. Thus, the open-cathode system is found to perform better at high temperature, and high humidity conditions whereas low humidity condition are not found favourable for such systems. These trends in cell performance are analysed using the trends of cell parameters like RH, temperature, and membrane water content (λ_c) across the single cell from inlet to outlet obtained from the modelling results. The gradient in temperature across the inlet and outlet (ΔT_c) is found to be ~5 ºC for the liquid-cooled

case while operating at high current density (CD) (0.3 V), whereas the similar case for an open-cathode cell with the same cathode inlet conditions exhibited nearly a doubling in the temperature rise (ΔT_c). The area lying under the ribs of the bipolar plate is found to have the highest temperature in the MEA for the open-cathode cell, whereas the MEA temperature for the liquid-cooled cell falling under the ribs is having a temperature close to the bulk BPP temperature. The trends of RH gradient across the inlet and outlet (ΔRH_c) as shown in Figure 10(b) helped in explaining the hygral management taking place inside the cell. Positive (ΔRH_c) suggested the enhanced cell hydration for liquid-cooled cases whereas a state of supersaturation is observed for the theoretical isothermal operating case-6 where the cell temperature is not guided by the cell kinetics and is decoupled from the thermal model. However, for all the operating open-cathode cases, negative ΔRH_c is observed depicting drying in such systems despite net water production. The *in-situ* EIS analysis performed on all the experimental cases 1 to 5 also validated the simulated results obtained for these operating cases. The open-cathode cases observed high frequency resistance (HFR) by nearly three times as compared to liquid-cooled cases attributed to the increased protonic resistance across the membrane and ionomer which results in the overall drying of such systems. The charge transfer resistances are also high for dry open-cathode cell operational cases with low ambient temperature compared to other cases representing the operational difficulty for such systems. Similar trends are shown by water content (λ) distribution across the cell obtained from modelling results. Overall, the hygrothermal coupling is found to maneuver the open-cathode fuel cell performance by guiding the kinetics of the system and the ohmic resistance across the cell. Complete information and analysis can be found in Appendix A and also from Sagar *et al.* [149].

3.2 Strategic ionomer design for high performing fuel cells with open cathode

The ionomer plays a vital role in being a key ingredient of a PEMFC MEA. The protonic transport across the electrodes via the membrane is facilitated by the ionomer being distributed at the catalyst layer site on both electrodes. Thus, the ionomer design becomes critical while designing an efficient fuel cell for getting higher performance. The effect of ionomer to carbon ratio, the solvent composition of the ionomer, and the trade-off between

Pt loading and ionomer content has been covered in some of the literature for conventional liquid-cooled systems [93]. The hydrophobic treatment of the ionomer layer at the CL is found to elevate the PEM fuel cell performance. When exposed to hot dry gas while performing the hot-pressing, the ionic side chains are found to form distinct hydrophilic and hydrophobic channels at the ionomer phase. The unsaturated channels are found to contribute to higher O_2 solubility whereas the saturated channels helped in better water transport [150-151]. Besides this, only limited research has been reported on ionomer effects consideration on open-cathode systems [96].

From the previous results obtained using 3D modelling as explained in Section 3.1, the hydration of the membrane and the CCL in total is detrimental to the performance of open-cathode systems. Lower hydration levels lead to poor protonic conductance as well as poor kinetics observed from the HFR results obtained for various cases of open-cathode operation. This motivated us to further investigate determining a suitable ionomer with strategic design such as to contribute towards elevated performance for open-cathode cells. The emphasis of this work is placed on studying the effect of γ, which is discovered to affect both the thermal and the water transport across the fuel cell MEAs [149]. The same value of γ is used for modelling both liquid-cooled cells and open-cathode cells. The γ decides the rate at which water is transported between the ionomer phase and the vapour phase inside the individual catalyst layer. It can also be related to the interfacial transport happening at the ionomer site driven by the water concentration across the interface. Overall, γ corresponds to the rate of water sorption/desorption at the ionomer phase in the CL. It is assumed to be guided by the surface morphology of the ionomer layer and thus can be approximated as the interfacial resistance offered by the ionomer layer for water transport. γ is kept at 10 s^{-1} for the first part of the work to validate the experimental results obtained using the commercial MEA. The choice of γ is kept irrespective of the phase in which water is generated. The 3D model developed in COMSOL Multiphysics is used to evaluate the effect of γ on various parameters like temperature, RH, oxygen mole fraction, and water content (λ) distributed across the cell. These factors are responsible for determining the overall cell performance of the single cell being simulated in the model. The three values of γ are studied on the single cell computational model operating at an ambient temperature of 40 ^{o}C and 40% RH with the air flow rate assigned at 2.5 nlpm and H_2 flow rate at 0.5 nlpm entering at 60% RH mimicking the dead-end mode operational case [147]. The details of the baseline MEA

design being used with material properties have been explained in Chapter 2.2. The results discussed in the previous section 3.1 used the γ value of 10.0 s^{-1} and is considered as the reference case for comparing the effect of the other two values of γ at 1.0 s^{-1} and 0.1 s^{-1}.

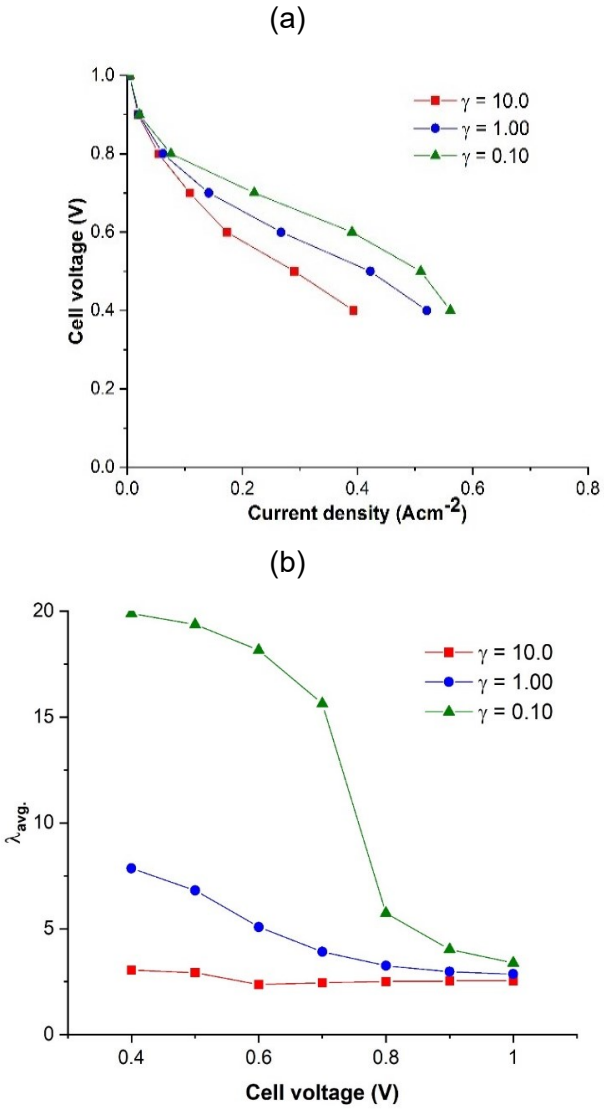

Figure 11. Effect of ionomer water sorption/desorption rate constant (γ) on the (a) polarization curve and (b) average water content at the PEM for open-cathode PEMFC systems.

The simulation results shown in Figure 11(a) depict that the cell performance of an open-cathode PEMFC increases with decreasing γ from 10.0 s^{-1} to 0.1 s^{-1}. The current density is found to increase by nearly 55% from the reference case of γ = 10 s^{-1} to γ = 1.0 s^{-1} at

0.6 V. Further, an improvement of 75% is found by decreasing the γ to 0.1 s^{-1}. The cell performance is found to increase primarily in the mid region of the polarization curve associated with ohmic transport and some increment is also observed in the mass transport region as well as the kinetic region. The temperature profiles from inlet to outlet didn't show significant changes for the three different values of γ and hence the other parameters such as the RH, λ, and O_2 mole fraction are found to be guiding the current density within the cell. The average water content ($\lambda_{avg.}$) at the PEM is also found to be increased by nearly two-fold for medium γ and eight-fold for low γ as compared to the reference case with γ = 10 s^{-1} as shown in Figure 11(b). This major change in λ_{avg} helps in increasing the overall protonic conduction across the MEA and can be attributed to the higher rate of water production at the cathode combined with the water retaining property of the ionomer achieved with low sorption/desorption rate. The average RH inside the MEA is found to be increased with a decrease in γ and the peak values of RH at the CCL are found to be at 78% and 152% respectively for γ = 1.0 s^{-1} and γ = 0.1 s^{-1} as compared to nearly 30% for the reference case with γ = 10.0 s^{-1} as shown in Figure 12. The RH is also a strong function of temperature interlinked with the saturation pressure. This trend ensures that changing γ to lower values can be helpful in overcoming the MEA dry out which is found earlier associated with an open-cathode PEMFC operation. At lower γ, oversaturation at the CCL signifies the onset of local liquid water condensation upon ionomer saturation. The consumption of O_2 is also found to increase following the increased rate of reaction with decreased γ and enhanced mass transport. Analyzing the overpotential across the cell using a voltage loss breakdown calculation reflected in reduced ohmic losses by nearly 15% for medium γ and a further decrement of 22% for lower γ at 0.1 s^{-1}. Overall, the results are found to be motivating towards an ionomer design with lesser γ equivalent to 0.1 s^{-1} suitable for a high performing open-cathode PEMFC as described in detail in Appendix B and also by Sagar *et al*. [149]. This kind of ionomer can be achieved practically by modifying the surface structure and the morphology of the existing ionomers; however, it remains out of the scope of this work and can be considered as future work. The γ values below 0.1 s^{-1} are also evaluated using the model, however significant improvement is not observed as reported in the present study and thus γ = 0.1 s^{-1} can be taken as a guiding parameter to be considered for future development of novel materials. Experimental verification of this study is performed to some extent by using an SSC ionomer replacing the high EW ionomer used conventionally which also has been reported to exhibit water retaining behaviour to some extent. The results are discussed in

Section 3.4 in more detail. The authors have limited their experimental investigation by demonstrating the effect of γ using the most suitable commercially available material, however, the scope of re-engineered new materials remains in the purview of future work. The complete design of the ionomer for achieving low gamma is out of the scope of this work. The ionomer should be re-engineered in such a way that the water transport at the cathode electrode between the ionomer phase and the gaseous phase happens at a slower rate while operating at dry ambient conditions. The production methodology of such materials along with the re-engineering is proposed to be the future work.

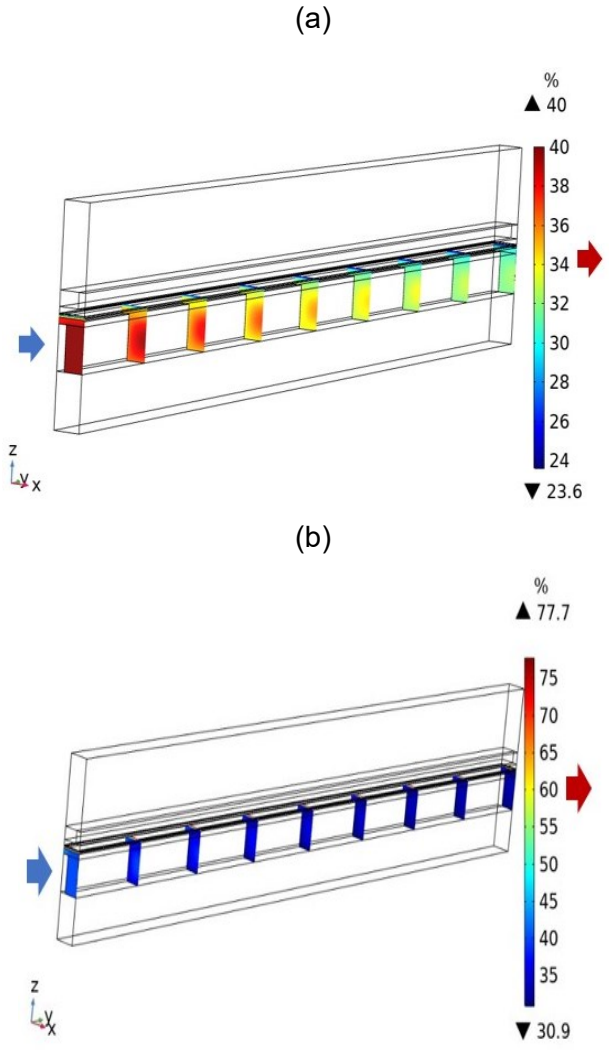

Figure 12. (a) Average RH profile at the cathode side for (a) γ = 10 s^{-1} and (b) γ = 0.1 s^{-1}.

3.3 Model driven membrane electrode assembly design for high-performing open-cathode polymer electrolyte membrane fuel cells

The strategic design of ionomer selection is covered in the previous Section 3.2. A significant improvement is achieved in cell performance operating at a high ambient temperature of 40 ^{o}C and RH of 40% primarily in the medium current density operating zone (at 0.6 V). The high current density operating region is still limited by mass transport limitations and design improvements are required for an overall effective MEA design. In the present section, the other components of the MEA namely, the PEM, CCL, and MPL are studied, and respective changes are made in their design to get a total performance boost in the performance of the open-cathode cell being operated at same ambient conditions as in Section 3.2. A set of computational iterations are performed to understand the effect of individual parameters on the overall cell performance followed by the study of the coupled effects of these components. The DoE is performed using full factorial design and ANOVA analysis to identify the interaction effects of various design parameters along with their individual effects. A total of 90 different CCL designs are evaluated using the 3D model developed in COMSOL Multiphysics with four factors of CCL design namely the thickness (t_{CCL}), porosity (ε_{CCL}), the weight percentage of ionomer (wt_{ion}), and %Pt/C being used with parametric levels detailed in Table 4. Similarly, PEM thickness effects are evaluated at three different levels and cathode side MPL changes are studied at 3 levels of discrete MPL thickness and 2 levels of MPL porosity. The 3D model is iterated for each of these cases and respective current densities are noted for operation at individual cell voltages of 0.6 V and 0.4 V. The individual cases which result in very high Pt loading (above 1 $mg_{Pt}\,cm^{-2}$) are discarded considering the cost implication. Thus, a total of 40 cases out of the 90 cases are evaluated for CCL design optimization. The details are presented in Appendix C. The CD for each of these 40 cases is evaluated and compared with the reference case taken from the previous section. For all the studies performed in this section, the γ is taken as 0.1 s^{-1} and considered as the base case with other MEA specifications as modelled in the previous section. The model is also simulated iteratively for different designs of the PEM and the MPL on the cathode side as mentioned above.

Table 4. Parametric design of MEA components for simulation and performance comparison of open-cathode PEMFCs.

Layer	Parameter (unit)	Parametric levels
Cathode catalyst layer (CCL)	t_{CCL} (μm)	15, 30
	ε_{CCL} (%)	20, 40, 60
	wt_{ion} (%)	20, 40, 60
	Pt/C (%)	20, 40, 60
Polymer electrolyte membrane (PEM)	t_{PEM} (μm)	10, 25, 50
Cathode microporous layer (CMPL)	t_{CMPL} (μm)	30, 60, 90
	ε_{CMPL} (%)	40, 60

With the decrease in PEM thickness from 50 μm to 10 μm keeping other design levels as constant brings an increment of 7.12% in the CD at 0.6 V. This is attributed to the decreased ohmic resistance offered by reduced PEM thickness, however, is limited by other design constraints of CCL and CMPL which remains at the reference design level. The best-case CCL design is found to have a CD increment of nearly 30% at 0.6 V. The T, RH, and O_2 mole fractions are analysed for each of these cases to understand the effect of these design changes on the overall performance. A voltage loss breakdown analysis is also performed to evaluate the change in different losses with the change in the design of different components of the MEA. For the CCL, the increase in CD is influenced by achieving a high Pt loading obtained by tuning t_{CCL} and ε_{CCL}. However, the increase in available Pt surface area for cell kinetics is not always economically favourable considering the high-cost implication with increased Pt loading. The increase in wt_{ion} from 20% to 40% provides improved proton conductivity whereas the Pt/C increment from 20% to 60% aids the ORR which in turn leads to higher CD and thereby increased temperature. Overall, the CCL design with $t_{CCL} = 15\ \mu m$, $\varepsilon_{CCL} = 40\%$, $wt_{ion} = 40\%$, and $Pt/C = 60\%$ gives the highest CD of 0.45 A cm^{-2} at 0.6 V as compared to 0.34 A cm^{-2} which is achieved for the baseline case shown in Figure 13(a). The indicating parameters like T, RH, and oxygen mole fraction are also found to be favourable towards an overall increase in cell performance for the best CCL. Similarly, thinner CMPL with high porosity is found to

support the open-cathode performance. The CMPL with 30 μm thickness and 60% porosity gave the highest performance as depicted in Figure 13(b) and is considered the best CMPL design. The CD change at 0.6 V remains negligible for the best CMPL design compared to the baseline MEA design whereas at 0.4 V the CD increases by up to 88%. The individual effects of CMPL thickness and CMPL porosity are found to impact the overall performance in a similar fashion quantitatively. The O_2 availability is increased both by decreasing the CMPL thickness and increasing the CMPL porosity thereby decreasing the overall diffusional resistance for O_2. Interestingly, the drying is evident with individual changes in the CMPL design with reference to the baseline case, however, sufficient saturation is achieved by elevating the CMPL design which helped in boosting the overall cell performance.

(a)

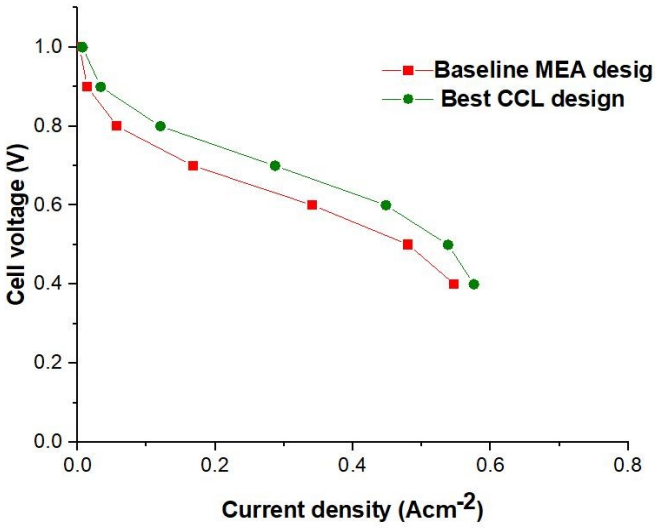

(b)

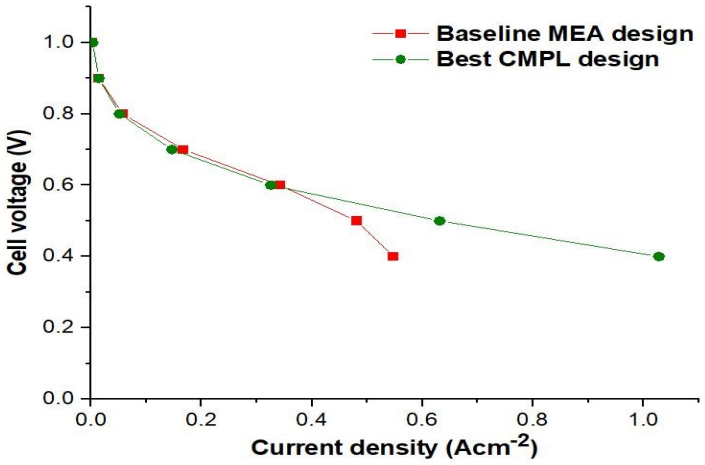

Figure 13. Comparative polarization curves for the baseline MEA design and the parametrically modified MEAs with (a) best CCL design and (b) best CMPL design.

Once the individual parametric studies are completed, a full factorial DoE analysis is performed using statistical software (Minitab 17) for three MEA design variables termed as factors namely, PEM, CCL, and CMPL with two levels at high (H) and low (L) as per Table 5. The maximum and minimum performing design cases obtained from the parametric evaluation of the three individual layers namely, the PEM, CCL, and CMPL are taken as the two distinct levels termed H and L, respectively. A total of eight simulations are run at these design levels and the resultant CD is used as the response to evaluate the main and interaction effects of these factors using a full factorial design. Figure 14 depicts the change in CD at 0.6 V when the MEA design is improved by only changing the enhanced version of the membrane, CCL, and CMPL one at a time and keeping other components at the same level denoted as '1'- '4'. The optimal MEA design shown as '5' is found to have the CD increased by nearly 120% as compared to the baseline MEA design which consists of the best design levels for an individual component of the MEA. ANOVA analysis is performed with a confidence interval of 0.95 at 0.6 V and 0.4 V each to find the significance of these designs at each operating current density. At medium current density (0.6 V), the effect of CCL design is maximum followed by CMPL and PEM in terms of main effects, all three being statistically significant. Also, from the pareto chart in Figure 15(a) the CCL and CMPL interaction effect is found significant as compared to less significant

PEM and CMPL interaction. The DoE results at high current density (0.4 V) show the CMPL main effect to be heavily dominant as compared to those of the CCL and PEM, with the main effect of PEM being negligible as shown in Figure 15(b). The interaction of CCL and CMPL is dominant among the two-way interactions, which is consistent with the outcome at 0.6 V, whereas the other two-way interactions are insignificant and hence neglected from the final DoE analysis at 0.4 V. Interestingly, this outcome suggests that the open-cathode cell performance at 0.4 V is statistically independent of the PEM thickness (10-50 μm) within the present scope of the DoE. This outcome is however influenced by the very strong impact of the CMPL design.

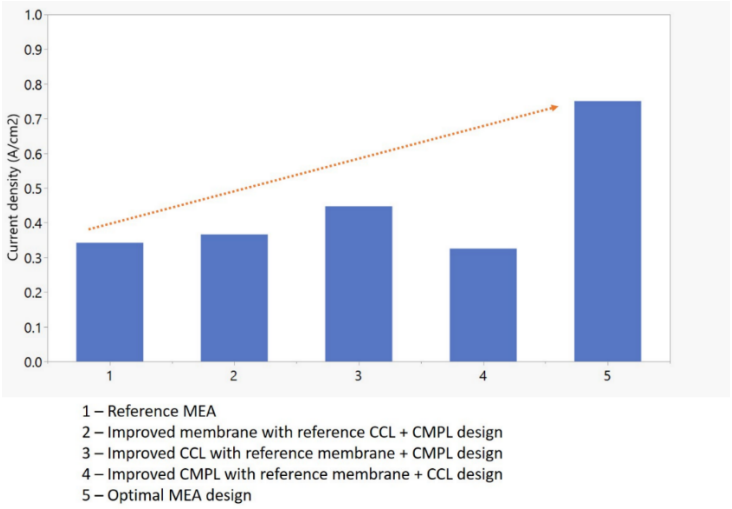

Figure 14. CD trend for the MEA design changes at 0.6 V.

Table 5. List of DoE design factors and levels.

Design Factor	Level (High)	Level (Low)
PEM Design	$t_{PEM} = 10\ \mu m$	$t_{PEM} = 50\ \mu m$
CCL Design	$t_{CCL} = 15\ \mu m$ $\varepsilon_{CCL} = 40\%$ $wt_{ion} = 40\%$ $per_{Pt/C} = 60\%$	$t_{CCL} = 15\ \mu m$ $\varepsilon_{CCL} = 20\%$ $wt_{ion} = 20\%$ $per_{Pt/C} = 20\%$
CMPL Design	$t_{CMPL} = 30\ \mu m$ $\varepsilon_{CMPL} = 60\%$	$t_{CMPL} = 90\ \mu m$ $\varepsilon_{CMPL} = 40\%$

Checking with the γ effect on the best MEA optimal design, by changing γ from 10 s^{-1} to 0.1 s^{-1} individually brought a change in CD by up to 130% at 0.6 V and 57% at 0.4 V. Thus, with the combined effect of γ change and improvised MEA design the CD is found to be increased by 224% at 0.6 V and 100% at 0.4 V respectively as compared to the baseline design defined in Section 3.1 with γ = 10 s^{-1}. Thus, the combination of improving the overall MEA design following the various parameters discussed in this section along with the ionomer design changes as discussed in Section 3.2 greatly improves the overall cell performance for open-cathode PEMFC. The optimal thermal and water management is achieved with these design changes and the gap between conventional liquid-cooled PEMFC design and open-cathode PEMFC design can be narrowed. More in depth analysis and discussion can be referred to Appendix C.

(a)

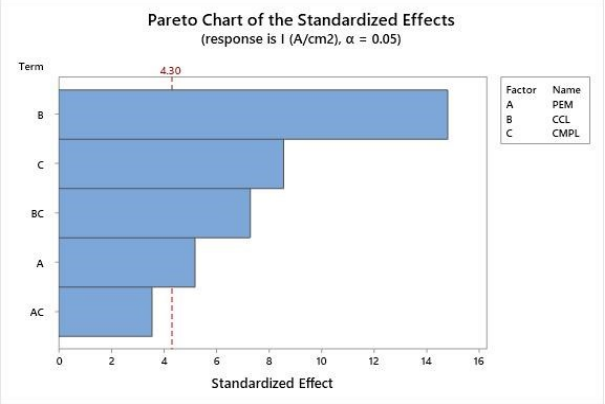

(b)

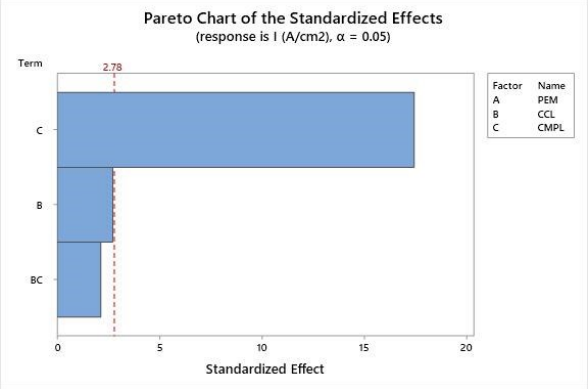

Figure 15. (a) Pareto charts obtained from ANOVA analysis at (a) 0.6 V and (b) 0.4 V.

3.4 Experimental design of high performing open cathode polymer electrolyte membrane fuel cells

From the previous sections, using a 3D computational model developed in COMSOL Multiphysics the open-cathode PEMFC is analysed first based on the operational conditions and its response towards various hygrothermal conditions (Section 3.1). The limitations of the open-cathode cell performance in terms of MEA drying, overheating, and high charge transfer resistance are established using the model developed. Section 3.2 and 3.3 then covers the strategies for improving the cell performance by redesigning the ionomer, MPL, PEM, and CCL using the same model. The objective of the present section is to verify the trends in the various component changes observed from the modelling results obtained. Experimental analysis is performed by testing several MEAs with a strategic selection of individual components like the ionomer, PEM, and GDL. A 25 cm^2 open-cathode single cell is developed in-house with bipolar plates designed indigenously as shown in Chapter 2. The anode side is having single serpentine flow channels engraved on the graphite plate whereas open channels are fabricated on the cathode side flow plate with the dimensions mentioned in Table 1 (Chapter 2). The single-cell test setup shown in Chapter 2.2 is installed inside an *Espec* environmental chamber connected with the Greenlight Innovation G400 test station for fuel cell testing. A small air compression unit is also installed inside the environmental chamber which sucks the air within the chamber and provides it to the cell through the duct connected with this device using a manual rotameter to control the air flow. A total of five MEAs are tested using this test setup with the first MEA being a commercial MEA from Ion Power Inc. This MEA is tested at the ambient operating condition of 40 ^oC and 40% RH which is chosen to be fitting the Indian summer conditions and is considered a particularly challenging condition for fuel cell operation. The H_2 is provided with a 60% RH mimicking an actual dead-end mode condition reported in real case operations [147]. The results obtained for the commercial MEA are taken as the baseline data and a further four MEAs are fabricated in-house by changing individual components one at a time. The detailed specifications of the MEAs are listed in Table 6. Each of the MEAs is pre- conditioned before the open-cathode testing

and thermal equilibrium is established to collect actual fuel cell data relatable to a full-scale fuel cell stack operating at individual current densities. *In-situ* EIS data are also collected to analyse the test data and establish the cause of performance changes with respect to the change in individual MEA compositions. The details are presented in Appendix D.

Table 6. Details of the different MEAs prepared for open-cathode fuel cell testing.

	Anode	**Cathode**	**PEM**
MEA-1 (Commercial)	m_{Pt} = 0.5 mg cm^{-2} GDL - SGL 29BC Ionomer – Nafion® (D521- 1100 EW)	m_{Pt} = 0.5 mg cm^{-2} GDL - SGL 29BC Ionomer – Nafion® (D521- 1100 EW)	Nafion® 212
MEA-2	m_{Pt} = 0.5 mg cm^{-2} GDL - SGL 29BC Ionomer – Nafion® (D521- 1100 EW)	m_{Pt} = 0.5 mg cm^{-2} GDL - SGL 29BC Ionomer – Nafion® (D521- 1100 EW)	Nafion® 212
MEA-3	m_{Pt} = 0.5 mg cm^{-2} GDL - SGL 29BC Ionomer – Aquivion (D72-25BS)	m_{Pt} = 0.5 mg cm^{-2} GDL - SGL 29BC Ionomer – Aquivion (D72-25BS)	Nafion® 212
MEA-4	m_{Pt} = 0.5 mg cm^{-2} GDL - SGL 29BC Ionomer – Aquivion (D72-25BS)	m_{Pt} = 0.5 mg cm^{-2} GDL - SGL 29BC Ionomer – Aquivion (D72-25BS)	Aquivion – 720-20
MEA-5	m_{Pt} = 0.5 mg cm^{-2} GDL - SGL 29BC Ionomer – Aquivion (D72-25BS)	m_{Pt} = 0.5 mg cm^{-2} GDL - SGL 22BB Ionomer – Aquivion (D72-25BS)	Aquivion – 720-20

From Figure 16(a), the cell performance of MEA-2 is found comparable to MEA-1 as expected pertaining to the same component design for both the MEAs with MEA-1 being procured commercially and MEA-2 being prepared in-house. The slight difference in the cell performance can be attributed to the change in the MEA preparation method from MEA-1 to MEA-2. The increment in CD for MEA-3 is observed to be 31.2% at 0.6 V and 30.0% at 0.4 V with reference to the CD obtained for the base case of MEA-1. This change in CD is mostly due to the change in ionomer from Nafion® D521 with an EW of 1100 which possess a long side chain (LSC) structure, unlike the Aquivion ionomer D72-25BS which is used for MEA-3 and has short side chain (SSC). The improvement in the CD is attributed to the better water retention capability shown by MEA-3 which is supported by the improved hydration level at MEAs with high water content. This trend is attributed to the higher water sorption property of the MEA-3 ionomer as compared to the baseline MEA. This trend verifies the modelling results in Section 3.2 where low γ is found to boost the cell performance significantly by providing water retention capabilities at the interfacial site of the ionomers dispersed in the CL. However, the incremental change in cell performance obtained from Section 3.2 for γ changes from 10 s^{-1} to 0.1 s^{-1} couldn't be exactly achieved experimentally and required re-engineered ionomer development which is out of the scope of the present work. In MEA-4, the change in the PEM from Nafion® 212 with 50 μm thickness to Aquivion with 20 μm thickness in conjunction with ionomer changes to Aquivion D72-25BS lead to a further boost in CD by nearly 75% at 0.6 V and 37.5% at 0.4 V respectively as shown in Figure 16(a) with reference to the base case. This is attributed to the decreased ohmic resistance for the MEA-4 configuration achieved by the strategic selection of ionomer and PEM as compared to the conventional design for MEA-1. These trends match the modelling predictions reported in Sections 3.2 and 3.3. The rise in the CD at 0.4 V for MEA-4 as compared to MEA-3 is however less significant than at 0.6 V due to mass transport limitations. Changing the cathode GDL from MEA-4 to MEA-5 from the previously used SGL 29BC to SGL 22BB helped in a further boost in CD by 12.5% at 0.6 V and 15.0% at 0.4 V respectively. This increment in CD is attributed to the decrease in GDL thickness from 235 μm to 215 μm and a decrease in areal weight from 90 g/m^2 to 70 g/m^2 which is corresponding to an overall increase in porosity. These trends verify the modelling results obtained with similar changes made at the MPL level. Since the GDLs used for the experimentation are commercial ones no specific data is available on whether the thickness and porosity changes are in the backing layer or in the MPL. However, the trends found experimentally assert the modelling results, and the

increment in CD is attributed to the lowering of O_2 transport resistance as validated by the experimental EIS data. The EIS data obtained at 0.6 V operation for each of the MEAs falls in line with the trends observed in terms of CD changes with respect to component changes as depicted in Figure 16(b). The HFR decreases from MEA-2 to MEA-3 validating the lowering of ohmic resistance by change of ionomer towards low γ or an equivalent lowering of EW and use of SSC. Additional decrement in HFR values is reported for Aquivion based thinner membrane in conjunction with Aquivion ionomer as reported for MEA-4 which justifies the lowering of PEM thickness to be beneficial for the overall MEA design for open-cathode PEMFC operation as per the modelling results. Finally, the decrease in charge transfer resistance for MEA-5 compared to MEA-4 from Figure 16(b) is attributed to the thinner GDL selection with high porosity and verifies our modelling results obtained in Section 3.3. The in-depth discussion and analysis are presented in Appendix D.

(a)

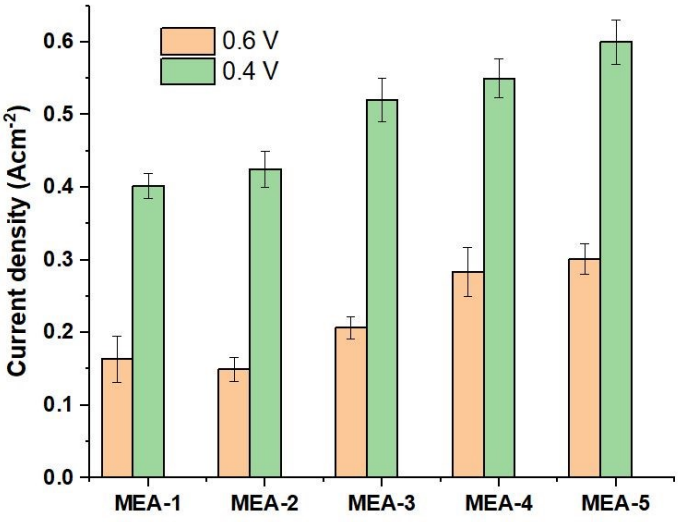

(b)

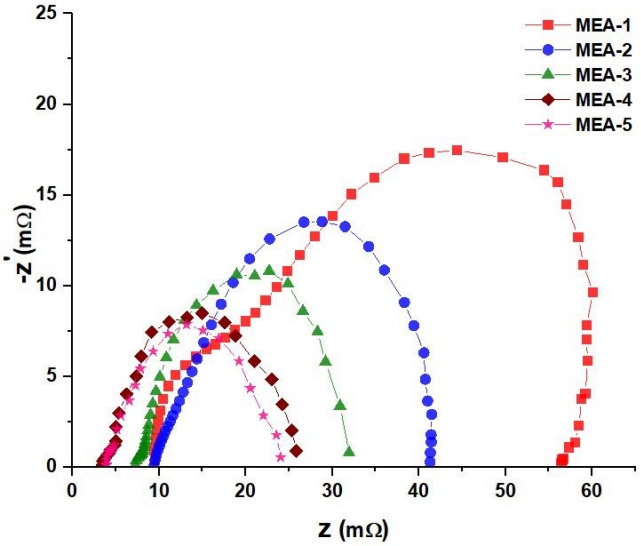

Figure 16. (a) Current density for the five MEAs operated at cell voltages of 0.6 V and 0.4 V at steady state, following thermal equilibration and (b) Comparative Nyquist plot of impedance for the five MEAs obtained by in-situ EIS on the single cell open-cathode fuel cell operated at 0.6 V.

Chapter 4.

Conclusions and Future work

4.1 Conclusions

The present thesis addresses the limitations associated with open-cathode PEMFCs which are detrimental to the low cell performance possessed by them as compared to conventional liquid-cooled systems. A computational approach is followed in understanding the behaviour of such systems at various operational conditions and a comparison is done with the conventional liquid-cooled system to draw a distinction between the two systems in terms of operational behaviour and response to given operating conditions. The individual component design primarily the ionomer, CCL, PEM, and CMPL are found crucial in determining the overall cell performance of such systems and thus computational studies are performed to study their individual and coupled effect on the system performance. Improved design for all these components is found out which are suitable for designing a high-performing open-cathode PEMFC system. These computational results are verified by conducting single cell experiments using in-house fabricated MEAs. The key contributions and findings are summarised below.

- The development of a robust three-dimensional model for open-cathode PEMFCs which can cover the wide operational regime and complex gradients of such systems is a major contribution of this thesis. The model developed in this work is a flexible model and can be used for liquid-cooled cells as well as open-cathode cells by changing a few boundary conditions to be chosen by the user. The model is also validated on a large set of data based on different operating conditions for both kinds of systems and thus serves as a guiding tool for further studies in terms of designing individual components. The two-phase water transport between the dissolved phase and the vapour phase is implemented in an efficient way which is crucial to the overall water management inside open-cathode PEMFCs.

- In the initial phase of this work, the focus is to determine the operational behaviour of such open-cathode systems in various operating environments. The

hygrothermal analysis is performed with several data points to establish the effect of change in cell performance with respect to ambient air conditions. This approach is also followed to distinguish the operational behaviour of such systems with respect to conventional liquid-cooled systems and point out key issues leading to lower performance of open-cathode PEMFCs. Drying, overheating, and high charge transfer resistance are found evident in such systems, unlike conventional liquid-cooled systems where humidification levels are maintained properly throughout the operational regime.

- With the help of the computational model, it is found that the well posed thermal and hygral modulation across the system for the liquid-cooled PEMFCs results in a boost of cell performance across low to high current densities, whereas, for the open-cathode PEMFCs the cell, performance is greatly dependent on the ambient air stream quality and determined by the unique hygrothermal characteristics of the cell. The slow electrochemical kinetics and high ohmic resistance are attributed to the primary underlying reasons for the low performance of open-cathode PEMFCs. The poor membrane hydration at different ambient operating cases is shown to possess high membrane ionic resistance which results in high ohmic losses. This is also verified experimentally by high frequency resistance measurements. The low ambient temperature cases are found to show lower cell kinetics by virtue of temperature whereas poor ionomer hydration is responsible for diminishing cell kinetics for cases with higher ambient temperature operation. Conclusively, improved ambient relative humidity at higher temperatures is found to boost the overall cell performance of open-cathode PEMFCs through increased membrane water content and decreased charge transfer resistance.

- The ionomer selection and design are also found very critical in deciding the overall cell performance of such open-cathode fuel cell systems. The change in γ is found to be very sensitive to the overall open-cathode cell performance. With lowering the γ value to 0.1 s^{-1} from the baseline value of 10.0 s^{-1} the CD is found to be remarkably impacted and is increased by 130% with respect to the baseline CD. Lowering γ is attributed to resulting in enhanced water retention at the ionomer phase of the CLs and PEM. This is found to be achieved by inversion of the through-plane relative humidity gradient at the MEA level, pointing to the indicative

rate of water production at the CCL surpassing the relative rate of drying incurred due to self-heating. The protonic conductivity is increased because of the improved ionomer hydration at elevated temperatures leading to a reduction in ohmic overpotential by nearly 37% which drives the overall cell performance shifted to a kinetically controlled regime.

- The PEM thickness showed the least sensitivity towards the CD as the MEA performance metric of interest out of parametric screening for PEM, CCL, and CMPL changes. For the CCL, out of 40 design cases evaluated with Pt loading below 1 mg cm^{-2}, the most influential factors were high ionomer loading to improve proton conductance and high Pt/C ratio to enhance the oxygen reduction kinetics which collectively led to higher CD and thereby increased cell temperature. Overall, the thin CCL design with moderate porosity and ionomer loading and high Pt/C ratio gave the highest CD of 0.45 A cm-2 at 0.6 V as compared to 0.34 A cm-2 for the baseline design. Similarly, a thin CMPL design with high porosity was found to enhance the CD by means of lower oxygen diffusion resistance, with the strongest effect observed at 0.4 V. This design was able to sustain good oxygen availability at the CCL despite the higher CD and rate of oxygen conversion. The kinetics were also promoted by the higher internal cell temperature reached due to the increased heat generation within the cell at elevated CD. However, drying of the membrane was also evident because of this, which restricted the overall performance.

- At 0.6 V, the CCL showed the maximum significance over the CMPL and PEM factors in terms of individual effect whereas the CCL and CMPL interaction was the most significant interaction effect. A synergistic benefit was observed from the combination of high-performing CCL and CMPL designs, which can be attributed to concurrent improvements in reaction kinetics and reduced ohmic resistance. On the other hand, at 0.4 V, the CMPL showed the strongest individual effect while the CCL and CMPL interaction was yet again the key interaction effect of significance. This was attributed to the well-managed oxygen transport and self-heating achieved with the thin, highly porous CMPL design as compared to the inferior baseline design. Overall, the strategic MEA design that leverages the jointly improved CCL, CMPL, and PEM designs was shown to more than double the CD performance at both 0.6 and 0.4 V, as the collective benefits of this MEA design

were able to induce simultaneous improvements in kinetic, ohmic, and mass transport properties aided by elevated cell temperature while retaining sufficient moisture to maintain good membrane hydration. A low rate of water sorption/desorption at the ionomer was also shown to be beneficial for the overall cell performance by virtue of improved water retention at the CCL under the relatively dry operating environment experienced by open-cathode PEMFCs.

- The effect of experimentally tuned membrane electrode assembly design was evaluated in this work for a 25 cm^2 single-cell open-cathode setup operated at the ambient condition of 40˚C and 40% RH. A total of five MEAs were tested at the given operating condition with a commercial MEA taken as the baseline. The other four MEAs were fabricated in-house and the subsequent effects of ionomer, membrane, and GDL changes were analyzed by comparing the average current densities obtained at fixed cell voltages of 0.6 V and 0.4 V. The three MEAs having SSC ionomer with low EW consistently achieved major performance improvement for the open-cathode cell by inducing better water retention capability at the CCL site which leads to improved protonic conduction in an otherwise dry environment. The subsequent introduction of a thinner membrane with the same low-EW SSC ionomer contributed a further CD increment of 44% at 0.6 V owing to drastically reduced ohmic cell resistance as measured by EIS.

- Experimentally, a thinner GDL with a more porous structure was found to elevate the cell performance by an additional 15% at 0.4 V through improved oxygen transport and thus lead to a suitable MEA design for high-performing open cathode PEMFCs. Importantly, the tuned MEA designs were able to leverage the incremental temperature rise at high CDs toward improved kinetics, as manifested by reduced charge transfer resistance measured by EIS. This capability was enabled by the improved water retention of the modified ionomer and membrane to avoid or delay membrane dry out. The results obtained experimentally in this work were also corroborated by theoretical predictions from computational modelling results for similarly designed and operated open-cathode fuel cells.

- Overall, a strategically optimized MEA design with a thinner membrane, lower γ, thin CCL with moderate porosity, increased ionomer loading, and high Pt/C ratio is

found to boost the cell performance for open-cathode PEMFCs along with thinner and high porous CMPL. The CCL design is found to be influencing the cell performance at medium operating cell voltages whereas the CMPL design influences more at lower cell voltages.

4.2 Future work

Due to the complexity of handling open-cathode experiments following the long hours towards achieving thermal equilibrium for each operating current density, the data set generated is limited and most experiments reported herein were performed to verify the trends of simulation results obtained from the computational model. The experimentation is limited to single cell to avoid complexity in the system and to minimize the cost of the experimental setup. As a recommendation for future work, a greater number of experiments can be performed using several MEAs on a larger stack to further investigate and scale-up the proposed design strategies. Operation of open-cathode stacks in recirculation mode with dead-ended anode needs also to be evaluated to understand the operational complexity of such systems in real world scenarios.

The 3D computational model is limited to two-phase water transport which is found apt for this system of open-cathode modelling. However, as per the improved design achieved for the open-cathode cell, liquid water presence can become significant, and more work will be required to capture that phenomenon inside the model. Thus, the present model can be extended to a three-phase model with liquid water addition which will be more suitable to capture high performing systems. Estimation of new correlations will be required in future work to model more membranes accurately with in-depth analysis to determine their material properties. The accuracy of the model greatly depends on the precision of the individual material data of components being used for testing. However, with a new range of materials being added continuously for the fuel cell operation all the material related data are not easily available in the literature or elsewhere which creates trouble in modelling those new materials. Thus, more work should be done to help the computational researchers with a wide range of material data sets for selection and implementation.

The low γ ionomer suggested in this study for significant improvement in open-cathode fuel cell performance leads to the development of novel materials matching these specific requirements. Due to the limitation in the scope of the study, this work only verified the results with commercially available Aquivion ionomer which follows the trend and is useful in giving more insight into the study. However, the actual increment in CD is not achieved using this ionomer and there is a huge scope for improvement as suggested by the modelling results which can be achieved by synthesizing such novel materials. Efforts can be made in developing such ionomers with strategic interfacial modifications to match the performance boost expected by $\gamma = 0.1\ s^{-1}$. Similarly, for the MPL design, there are quite limited options available commercially. Thus, the targeted MPL could be explored by fabricating in-house MPLs using precision instruments and equipment required for such synthesis and then evaluated experimentally with a setup such as the one developed in this work. The long-term testing and durability studies should also be performed on the improved MEA design possessing high-performance for open-cathode PEMFCs. Standard protocols for open-cathode durability testing are also not defined clearly by the Department of Energy or other reputed organizations to be followed and remains a challenge in this area of research. Thus, efforts can be laid out in determining such durability protocols and performing long term testing to achieve long lasting MEAs for open-cathode cell operations. The present study can also be extrapolated to a larger active area of the individual MEAs to understand its effect in such scenarios. Detailed characterization studies on the MEAs can also be performed to visualize *in-situ* changes happening at the MEA level for such open-cathode systems.

References

[1] J. O. Abe, A. P. I. Popoola, E. Ajenifuja, and O. M. Popoola, "Hydrogen energy, economy and storage: Review and recommendation," *Int. J. Hydrogen Energy*, vol. 44, no. 29, pp. 15072–15086, 2019.

[2] H. B. Aditiya and M. Aziz, "Prospect of hydrogen energy in Asia-Pacific: A perspective review on techno-socio-economy nexus," *Int. J. Hydrogen Energy*, vol. 46, no. 71, pp. 35027–35056, 2021.

[3] R. Yukesh Kannah, S. Kavitha, Preethi, O. Parthiba Karthikeyan, G. Kumar, N. V. Dai-Viet, and J. Rajesh Banu, "Techno-economic assessment of various hydrogen production methods – A review," *Bioresour. Technol.*, vol. 319, p. 124175, 2021.

[4] NRCan, "Seizing the Opportunities for Hydrogen," 2020.

[5] MNRE GoI, "National Hydrogen Mission," 2022.

[6] Y. Wang, K. S. Chen, J. Mishler, S. C. Cho, and X. C. Adroher, "A review of polymer electrolyte membrane fuel cells: Technology, applications, and needs on fundamental research," *Appl. Energy*, vol. 88, no. 4, pp. 981–1007, 2011.

[7] M. M. Mench, *Fuel Cell Engines*. 2008.

[8] R. O'hayre, S.-W. Cha, W. Colella, and F. B. Prinz, *Fuel cell fundamentals*. John Wiley & Sons, 2016.

[9] I. Bar-On, R. Kirchain, and R. Roth, "Technical cost analysis for PEM fuel cells," *J. Power Sources*, vol. 109, no. 1, pp. 71–75, 2002.

[10] E. J. Carlson, P. Kopf, J. Sinha, S. Sriramulu, and Y. Yang, "Cost Analysis of PEM Fuel Cell Systems for Transportation," *Natl. Renew. Energy Lab.*, no. December, p. NREL/SR-560-39104, 2005.

[11] J. Wu, S. Galli, I. Lagana, A. Pozio, G. Monteleone, X. Z. Yuan, J. Martin, and H. Wang, "An air-cooled proton exchange membrane fuel cell with combined oxidant and coolant flow," *J. Power Sources*, vol. 188, no. 1, pp. 199–204, 2009.

[12] . P. R. B., "a Review on Fuel Cell and Its Applications," *Int. J. Res. Eng. Technol.*, vol. 03, no. 03, pp. 562–565, 2014.

[13] J.-H. Wee, "Applications of proton exchange membrane fuel cell systems," *Renew. Sustain. Energy Rev.*, vol. 11, no. 8, pp. 1720–1738, 2007.

[14] H. Wang, H. Li, and X.-Z. Yuan, *PEM fuel cell failure mode analysis*, vol. 1. CRC Press, 2011.

[15] F. Tiss, R. Chouikh, and A. Guizani, "Dynamic modeling of a PEM fuel cell with temperature effects," *Int. J. Hydrogen Energy*, vol. 38, no. 20, pp. 8532–8541, 2013.

[16] P. Zhou, C. W. Wu, and G. J. Ma, “Influence of clamping force on the performance of PEMFCs,” *J. Power Sources*, vol. 163, no. 2, pp. 874–881, 2007.

[17] W. R. W. Daud, R. E. Rosli, E. H. Majlan, S. A. A. Hamid, R. Mohamed, and T. Husaini, “PEM fuel cell system control: A review,” *Renew. Energy*, vol. 113, pp. 620–638, 2017.

[18] A. Z. Weber, R. L. Borup, R. M. Darling, P. K. Das, T. J. Dursch, W. Gu, D. Harvey, A. Kusoglu, S. Litster, M. M. Mench, *et al.*, “A Critical Review of Modeling Transport Phenomena in Polymer-Electrolyte Fuel Cells,” *J. Electrochem. Soc.*, 2014.

[19] G. Zhang and S. G. Kandlikar, “A critical review of cooling techniques in proton exchange membrane fuel cell stacks,” *Int. J. Hydrogen Energy*, vol. 37, no. 3, pp. 2412–2429, 2012.

[20] M. A. R. S. Al-Baghdadi, “Modelling of proton exchange membrane fuel cell performance based on semi-empirical equations,” *Renew. Energy*, vol. 30, no. 10, pp. 1587–1599, 2005.

[21] R. Roshandel, B. Farhanieh, and E. Saievar-Iranizad, “The effects of porosity distribution variation on PEM fuel cell performance,” *Renew. Energy*, vol. 30, no. 10, pp. 1557–1572, 2005.

[22] R. Jiang, C. K. Mittelsteadt, and C. S. Gittleman, “Through-Plane Proton Transport Resistance of Membrane and Ohmic Resistance Distribution in Fuel Cells,” pp. 1440–1446, 2009.

[23] S. Yuvarajan and D. Yu, “Characteristics and modeling of PEM fuel cells,” 2004, vol. 5, pp. 7–10.

[24] S. M. Rahgoshay, A. A. Ranjbar, A. Ramiar, and E. Alizadeh, “Thermal investigation of a PEM fuel cell with cooling flow field,” *Energy*, vol. 134, pp. 61–73, 2017.

[25] A. de las Heras, F. J. Vivas, F. Segura, and J. M. Andújar, “How the BoP configuration affects the performance in an air-cooled polymer electrolyte fuel cell. Keys to design the best configuration,” *Int. J. Hydrogen Energy*, vol. 42, no. 17, pp. 12841–12855, 2017.

[26] Y. Wang, Y. Wang, and G. Chen, “Robust composite adaptive neural network control for air management system of PEM fuel cell based on high-gain observer,” *Neural Comput. Appl.*, vol. 32, no. 14, pp. 10229–10243, 2020.

[27] S. G. Kandlikar and Z. Lu, “Thermal management issues in a PEMFC stack - A brief review of current status,” *Appl. Therm. Eng.*, vol. 29, no. 7, pp. 1276–1280, 2009.

[28] R. Flückiger, A. Tiefenauer, M. Ruge, C. Aebi, A. Wokaun, and F. N. Büchi, “Thermal analysis and optimization of a portable, edge-air-cooled PEFC stack,” *J. Power Sources*, vol. 172, no. 1, pp. 324–333, 2007.

[29] H. S. Han, C. Cho, S. Y. Kim, and J. M. Hyun, “Performance evaluation of a polymer electrolyte membrane fuel cell system for powering portable freezer,” *Appl. Energy*, vol. 105, pp. 125–137, 2013.

[30] W. A. N. W. Mohamed, R. Atan, and A. A. Ismail, “Heat Transfer Simulation of a Single Channel Air- Cooled Polymer Electrolyte Membrane Fuel Cell Stack with Extended Cooling Surface,” no. Cssr, pp. 91–96, 2010.

[31] Y. Zhang, A. Mawardi, and R. Pitchumani, “Numerical studies on an air-breathing proton exchange membrane (PEM) fuel cell stack,” *J. Power Sources*, vol. 173, no. 1, pp. 264–276, 2007.

[32] P. Manoj Kumar and V. Parthasarathy, “A passive method of water management for an air-breathing proton exchange membrane fuel cell,” *Energy*, vol. 51, pp. 457–461, 2013.

[33] C. Mahjoubi, J.-C. Olivier, S. Skander-mustapha, M. Machmoum, and I. Slama-belkhodja, “An improved thermal control of open cathode proton exchange membrane fuel cell,” *Int. J. Hydrogen Energy*, vol. 44, no. 22, pp. 11332–11345, 2019.

[34] J. Ishaku, N. Lotfi, H. Zomorodi, and R. G. Landers, “Control-oriented modeling for open-cathode fuel cell systems,” 2014, pp. 268–273.

[35] J. C. Kurnia, B. A. Chaedir, A. P. Sasmito, and T. Shamim, “Progress on open cathode proton exchange membrane fuel cell: Performance, designs, challenges and future directions,” *Appl. Energy*, vol. 283, no. November 2020, p. 116359, 2021.

[36] F. Barreras, A. M. López, A. Lozano, and J. E. Barranco, “Experimental study of the pressure drop in the cathode side of air-forced Open-cathode proton exchange membrane fuel cells,” *Int. J. Hydrogen Energy*, vol. 36, no. 13, pp. 7612–7620, 2011.

[37] A. P. Sasmito, E. Birgersson, K. W. Lum, and A. S. Mujumdar, “Fan selection and stack design for open-cathode polymer electrolyte fuel cell stacks,” *Renew. Energy*, vol. 37, no. 1, pp. 325–332, 2012.

[38] C. Y. Ling, H. Cao, Y. Chen, M. Han, and E. Birgersson, “Compact open cathode feed system for PEMFCs,” *Appl. Energy*, vol. 164, pp. 670–675, 2016.

[39] T. Zeng, C. Zhang, Z. Huang, M. Li, S. H. Chan, Q. Li, and X. Wu, “Experimental investigation on the mechanism of variable fan speed control in Open cathode PEM fuel cell,” *Int. J. Hydrogen Energy*, vol. 44, no. 43, pp. 24017–24027, 2019.

[40] A. De las Heras, F. J. Vivas, F. Segura, M. J. Redondo, and J. M. Andújar, “Air-cooled fuel cells: Keys to design and build the oxidant/cooling system,” *Renew. Energy*, vol. 125, pp. 1–20, Sep. 2018.

[41] S. Kiattamrong and A. Sripakagorn, *Effects of the Geometry of the Air Flowfield on the Performance of an Open-Cathode PEMFC - Transient Load Operation*, vol. 79.

Elsevier B.V., 2015.

[42] C. Zhao, S. Xing, M. Chen, W. Liu, and H. Wang, “Optimal design of cathode flow channel for air-cooled PEMFC with open cathode,” *Int. J. Hydrogen Energy*, vol. 45, no. 35, pp. 17771–17781, 2020.

[43] F. Barreras, A. Lozano, J. Barroso, V. Roda, and M. Maza, “Theoretical model for the optimal design of air cooling systems of polymer electrolyte fuel cells. Application to a high-temperature PEMFC,” *Fuel Cells*, vol. 13, no. 2, pp. 227–237, 2013.

[44] H. Al-Zeyoudi, A. P. Sasmito, and T. Shamim, “Performance evaluation of an open-cathode PEM fuel cell stack under ambient conditions: Case study of United Arab Emirates,” *Energy Convers. Manag.*, 2015.

[45] A. Alanazi, “Performance evaluation of air breathing PEMFC under Saudi Arabia ’ s ambient conditions using three-dimensional FEM model,” pp. 1–14, 2017.

[46] D. T. Santa Rosa, D. G. Pinto, V. S. Silva, R. A. Silva, and C. M. Rangel, “High performance PEMFC stack with open-cathode at ambient pressure and temperature conditions,” *Int. J. Hydrogen Energy*, vol. 32, no. 17, pp. 4350–4357, 2007.

[47] K. S. Dhathathreyan, N. Rajalakshmi, K. Jayakumar, and S. Pandian, “Forced Air-Breathing PEMFC Stacks,” *Int. J. Electrochem.*, vol. 2012, pp. 1–7, 2012.

[48] G. Bin Jung, K. F. Lo, A. Su, F. B. Weng, C. H. Tu, T. F. Yang, and S. H. Chan, “Experimental evaluation of an ambient forced-feed air-supply PEM fuel cell,” *Int. J. Hydrogen Energy*, vol. 33, no. 12, pp. 2980–2985, 2008.

[49] C. Zhao, S. Xing, W. Liu, and H. Wang, “Comprehensive Anode Parameter Study for an Open-Cathode PEMFC,” *Energy and Fuels*, vol. 34, no. 6, pp. 7582–7590, 2020.

[50] W. M. Yan, M. S. Zeng, T. F. Yang, C. Y. Chen, M. Amani, and P. Amani, “Performance improvement of air-breathing proton exchange membrane fuel cell stacks by thermal management,” *Int. J. Hydrogen Energy*, vol. 45, no. 42, pp. 22324–22339, 2020.

[51] Y. J. Sohn, G. G. Park, T. H. Yang, Y. G. Yoon, W. Y. Lee, S. D. Yim, and C. S. Kim, “Operating characteristics of an air-cooling PEMFC for portable applications,” *J. Power Sources*, 2005.

[52] Y.-G. Yoon, W.-Y. Lee, T.-H. Yang, G.-G. Park, and C.-S. Kim, “Current distribution in a single cell of PEMFC,” *J. Power Sources*, vol. 118, no. 1, pp. 193–199, 2003.

[53] S. Park and B. N. Popov, “Effect of a GDL based on carbon paper or carbon cloth on PEM fuel cell performance,” *Fuel*, vol. 90, no. 1, pp. 436–440, 2011.

[54] D. H. Ahmed, H. J. Sung, and J. Bae, “Effect of GDL permeability on water and

thermal management in PEMFCs—II. Clamping force," *Int. J. Hydrogen Energy*, vol. 33, no. 14, pp. 3786–3800, 2008.

[55] N. Alhazmi, D. B. Ingham, M. S. Ismail, K. J. Hughes, L. Ma, and M. Pourkashanian, "Effect of the anisotropic thermal conductivity of GDL on the performance of PEM fuel cells," *Int. J. Hydrogen Energy*, vol. 38, no. 1, pp. 603–611, 2013.

[56] J. C. Lin, H. R. Jnutz, and J. M. Fenton, *Handbook of Fuel Cells/Eds. W. Vielstich, A. Lamm, HA Gasteiger*. New York, John Wiley & Sons Ltd, 2003.

[57] J. Yablecki and A. Bazylak, "Determining the effective thermal conductivity of compressed PEMFC GDLs through thermal resistance modelling," *J. Power Sources*, vol. 217, pp. 470–478, 2012.

[58] P. M. Wilde, M. Mändle, M. Murata, and N. Berg, "Structural and physical properties of GDL and GDL/BPP combinations and their influence on PEMFC performance," *Fuel Cells*, vol. 4, no. 3, pp. 180–184, 2004.

[59] R. R. Rashapov and J. T. Gostick, "Gas-diffusion-layer structural properties under compression via X-ray tomography," *J. Power Sources*, vol. 115, no. 3, pp. 411–433, 2016.

[60] I. V. Zenyuk, D. Y. Parkinson, L. G. Connolly, and A. Z. Weber, "Gas-diffusion-layer structural properties under compression via X-ray tomography," *J. Power Sources*, vol. 328, pp. 364–376, 2016.

[61] Q. Meyer, S. Ashton, P. Boillat, M. Cochet, E. Engebretsen, D. P. Finegan, X. Lu, J. J. Bailey, N. Mansor, R. Abdulaziz, *et al.*, "Effect of gas diffusion layer properties on water distribution across air-cooled, open-cathode polymer electrolyte fuel cells: A combined ex-situ X-ray tomography and in-operando neutron imaging study," *Electrochim. Acta*, 2016.

[62] E. Antolini, L. Giorgi, and A. Pozio, "Development of gas diffusion electrodes for polymer electrolyte fuel cells," *Mater. Technol.*, vol. 13, no. 2, pp. 67–68, 1998.

[63] S. Park, J.-W. Lee, and B. N. Popov, "Effect of PTFE content in microporous layer on water management in PEM fuel cells," *J. Power Sources*, vol. 177, no. 2, pp. 457–463, Mar. 2008.

[64] O. S. Burheim, J. G. Pharoah, H. Lampert, P. J. S. Vie, and S. Kjelstrup, "Through-plane thermal conductivity of PEMFC porous transport layers," *J. Fuel Cell Sci. Technol.*, vol. 8, no. 2, pp. 1–11, 2011.

[65] R. R. Rashapov, J. Unno, and J. T. Gostick, "Characterization of PEMFC Gas Diffusion Layer Porosity," *J. Electrochem. Soc.*, vol. 162, no. 6, pp. F603–F612, 2015.

[66] S. Yu, X. Li, J. Li, S. Liu, W. Lu, Z. Shao, and B. Yi, "Study on hydrophobicity degradation of gas diffusion layer in proton exchange membrane fuel cells," *Energy*

Convers. Manag., vol. 76, pp. 301–306, 2013.

[67] A. Nanjundappa, A. S. Alavijeh, M. El Hannach, D. Harvey, and E. Kjeang, "A customized framework for 3-D morphological characterization of microporous layers," *Electrochim. Acta*, vol. 110, pp. 349–357, 2013.

[68] R. W. Atkinson, J. A. Rodgers, M. W. Hazard, R. O. Stroman, and B. D. Gould, "Influence of cathode gas diffusion media porosity on open-cathode fuel cells," *J. Electrochem. Soc.*, vol. 165, no. 11, pp. F1002–F1011, 2018.

[69] C. Zhao, S. Xing, W. Liu, M. Chen, and H. Wang, "Performance improvement for air-cooled open-cathode proton exchange membrane fuel cell with different design parameters of the gas diffusion layer," *Prog. Nat. Sci. Mater. Int.*, vol. 7, no. 2, pp. 1–16, Oct. 2020.

[70] T. Chen, S. Liu, J. Zhang, and M. Tang, "Study on the characteristics of GDL with different PTFE content and its effect on the performance of PEMFC," *Int. J. Heat Mass Transf.*, vol. 128, pp. 1168–1174, 2019.

[71] T. Kitahara, H. Nakajima, and K. Mori, "Hydrophilic and hydrophobic double microporous layer coated gas diffusion layer for enhancing performance of polymer electrolyte fuel cells under no-humidification at the cathode," *J. Power Sources*, vol. 199, pp. 29–36, 2012.

[72] Z. Xiong, S. Liao, D. Dang, X. Tian, S. Hou, F. Liu, H. Peng, and Z. Fu, "Enhanced water management in the cathode of an air-breathing PEMFC using a dual catalyst layer and optimizing the gas diffusion and microporous layers," *Int. J. Hydrogen Energy*, vol. 40, no. 10, pp. 3961–3967, Mar. 2015.

[73] J. H. Chun, K. T. Park, D. H. Jo, J. Y. Lee, S. G. Kim, S. H. Park, E. S. Lee, J. Y. Jyoung, and S. H. Kim, "Development of a novel hydrophobic/hydrophilic double micro porous layer for use in a cathode gas diffusion layer in PEMFC," *Int. J. Hydrogen Energy*, vol. 36, no. 14, pp. 8422–8428, 2011.

[74] F. S. Nanadegani, E. N. Lay, and B. Sunden, "Effects of an MPL on water and thermal management in a PEMFC," *Int. J. Energy Res.*, vol. 43, no. 1, pp. 274–296, 2019.

[75] P. Satjaritanun, S. Hirano, I. V. Zenyuk, J. W. Weidner, N. Tippayawong, and S. Shimpalee, "Numerical Study of Electrochemical Kinetics and Mass Transport inside Nano-Structural Catalyst Layer of PEMFC Using Lattice Boltzmann Agglomeration Method," *J. Electrochem. Soc.*, vol. 167, no. 1, p. 013516, 2020.

[76] P. Berg, A. Novruzi, and O. Volkov, "Reaction Kinetics at the Triple-Phase Boundary in PEM Fuel Cells," *J. Fuel Cell Sci. Technol.*, vol. 5, no. 2, Apr. 2008.

[77] E. Billy, F. Maillard, A. Morin, L. Guetaz, F. Emieux, C. Thurier, P. Doppelt, S. Donet, and S. Mailley, "Impact of ultra-low Pt loadings on the performance of anode/cathode in a proton-exchange membrane fuel cell," *J. Power Sources*, vol.

195, no. 9, pp. 2737–2746, 2010.

[78] W. Wang, S. Chen, J. Li, and W. Wang, “Fabrication of catalyst coated membrane with screen printing method in a proton exchange membrane fuel cell,” *Int. J. Hydrogen Energy*, vol. 40, no. 13, pp. 4649–4658, 2015.

[79] S. Thanasilp and M. Hunsom, “Effect of MEA fabrication techniques on the cell performance of Pt–Pd/C electrocatalyst for oxygen reduction in PEM fuel cell,” *Fuel*, vol. 89, no. 12, pp. 3847–3852, 2010.

[80] A.-L. Ong, G.-B. Jung, C.-C. Wu, and W.-M. Yan, “Single-step fabrication of ABPBI-based GDE and study of its MEA characteristics for high-temperature PEM fuel cells,” *Int. J. Hydrogen Energy*, vol. 35, no. 15, pp. 7866–7873, 2010.

[81] I. Fouzaï, S. Gentil, V. C. Bassetto, W. O. Silva, R. Maher, and H. H. Girault, “Catalytic layer-membrane electrode assembly methods for optimum triple phase boundaries and fuel cell performances,” *J. Mater. Chem. A*, vol. 9, no. 18, pp. 11096–11123, 2021.

[82] Y. Guo, F. Pan, W. Chen, Z. Ding, D. Yang, B. Li, P. Ming, and C. Zhang, *The Controllable Design of Catalyst Inks to Enhance PEMFC Performance: A Review*, vol. 4, no. 1. Springer Singapore, 2021.

[83] E. H. Majlan, D. Rohendi, W. R. W. Daud, T. Husaini, and M. A. Haque, “Electrode for proton exchange membrane fuel cells: A review,” *Renew. Sustain. Energy Rev.*, vol. 89, no. June 2017, pp. 117–134, 2018.

[84] C. Lei, F. Yang, N. Macauley, M. Spinetta, G. Purdy, J. Jankovic, D. A. Cullen, K. L. More, Y. S. Kim, and H. Xu, “Impact of Catalyst Ink Dispersing Solvent on PEM Fuel Cell Performance and Durability,” *J. Electrochem. Soc.*, vol. 168, no. 4, p. 44517, 2021.

[85] W. Liu, L. Wan, J. Liu, M. Zhao, and Z. Zou, “Performance improvement of the open-cathode proton exchange membrane fuel cell by optimizing membrane electrode assemblies,” *Int. J. Hydrogen Energy*, 2015.

[86] J. Marquis and M.-O. Coppens, “Achieving ultra-high platinum utilization via optimization of PEM fuel cell cathode catalyst layer microstructure,” *Chem. Eng. Sci.*, vol. 102, pp. 151–162, Oct. 2013.

[87] M. B. Sassin, Y. Garsany, R. W. Atkinson, R. M. E. Hjelm, and K. E. Swider-Lyons, “Understanding the interplay between cathode catalyst layer porosity and thickness on transport limitations en route to high-performance PEMFCs,” *Int. J. Hydrogen Energy*, vol. 44, no. 31, pp. 16944–16955, Jun. 2019.

[88] Y. Liu, M. W. Murphy, D. R. Baker, W. Gu, C. Ji, J. Jorne, and H. A. Gasteiger, “Proton Conduction and Oxygen Reduction Kinetics in PEM Fuel Cell Cathodes: Effects of Ionomer-to-Carbon Ratio and Relative Humidity,” *J. Electrochem. Soc.*, vol. 156, no. 8, p. B970, 2009.

[89] M. Eguchi, K. Baba, T. Onuma, K. Yoshida, K. Iwasawa, Y. Kobayashi, K. Uno, K. Komatsu, M. Kobori, M. Nishitani-Gamo, *et al.*, "Influence of ionomer/carbon ratio on the performance of a polymer electrolyte fuel cell," *Polymers (Basel).*, vol. 4, no. 4, pp. 1645–1656, 2012.

[90] M. Uchida, Y. C. Park, K. Kakinuma, H. Yano, D. A. Tryk, T. Kamino, H. Uchida, and M. Watanabe, "Effect of the state of distribution of supported Pt nanoparticles on effective Pt utilization in polymer electrolyte fuel cells," *Phys. Chem. Chem. Phys.*, vol. 15, no. 27, pp. 11236–11247, 2013.

[91] M. Lee, M. Uchida, H. Yano, D. A. Tryk, H. Uchida, and M. Watanabe, "New evaluation method for the effectiveness of platinum/carbon electrocatalysts under operating conditions," *Electrochim. Acta*, vol. 55, no. 28, pp. 8504–8512, 2010.

[92] M. Lopez-Haro, L. Guétaz, T. Printemps, A. Morin, S. Escribano, P. H. Jouneau, P. Bayle-Guillemaud, F. Chandezon, and G. Gebel, "Three-dimensional analysis of Nafion layers in fuel cell electrodes," *Nat. Commun.*, vol. 5, pp. 1–6, 2014.

[93] Y. Liu, C. Ji, W. Gu, J. Jorne, and H. A. Gasteiger, "Effects of Catalyst Carbon Support on Proton Conduction and Cathode Performance in PEM Fuel Cells," *J. Electrochem. Soc.*, vol. 158, no. 6, p. B614, 2011.

[94] W. G. Grot, "Perfluorinated ion exchange polymers and their use in research and industry," *Macromol. Symp.*, vol. 82, no. 1, pp. 161–172, 1994.

[95] N. H. Jalani, K. Dunn, and R. Datta, "Synthesis and characterization of Nafion®-MO2 (M=Zr, Si, Ti) nanocomposite membranes for higher temperature PEM fuel cells," *Electrochim. Acta*, vol. 51, no. 3, pp. 553–560, 2005.

[96] R. W. Atkinson, Y. Garsany, J. A. Rodgers, M. W. Hazard, R. O. Stroman, and B. D. Gould, "Influence of Cathode Catalyst Layer Ionomer on Air-Cooled, Open-Cathode Fuel Cells," *ECS Trans.*, vol. 80, no. 8, pp. 461–475, 2017.

[97] Y. Garsany, M. B. Sassin, B. D. Gould, R. Marielle, E. Hjelm, and K. Swider-lyons, "Influence of Short-Side-Chain Perfluorosulfonic Acid Ionomer As Binders on the Performance of Fuel Cell Cathode Catalyst Layers," 2017, vol. MA2017-02, no. 1469, pp. 33–35.

[98] S. Poojary, M. N. Islam, U. N. Shrivastava, E. P. L. Roberts, and K. Karan, "Transport and Electrochemical Interface Properties of Ionomers in Low-Pt Loading Catalyst Layers: Effect of Ionomer Equivalent Weight and Relative Humidity," *Molecules*, vol. 25, no. 15, p. 3387, Jul. 2020.

[99] Y. Ono, A. Ohma, K. Shinohara, and K. Fushinobu, "Influence of Equivalent Weight of Ionomer on Local Oxygen Transport Resistance in Cathode Catalyst Layers," *J. Electrochem. Soc.*, vol. 160, no. 8, pp. F779–F787, 2013.

[100] S. Ma, Q. Chen, F. H. Jøgensen, P. C. Stein, and E. M. Skou, "19F NMR studies of Nafion^{TM} ionomer adsorption on PEMFC catalysts and supporting carbons," *Solid*

State Ionics, vol. 178, no. 29–30, pp. 1568–1575, 2007.

[101] Y. Wang, D. F. Ruiz Diaz, K. S. Chen, Z. Wang, and X. C. Adroher, "Materials, technological status, and fundamentals of PEM fuel cells – A review," *Mater. Today*, vol. 32, no. February, pp. 178–203, 2020.

[102] S. M. Haile, "Fuel cell materials and components," *Acta Mater.*, vol. 51, no. 19, pp. 5981–6000, 2003.

[103] D. D. Jones, B. T. Gaudette, J. R. Wilmore, I. Chernova, A. Bortnick, B. M. Weiss, and D. Allman, "MTOR has distinct functions in generating versus sustaining humoral immunity," *J. Clin. Invest.*, vol. 126, no. 11, pp. 4250–4261, 2016.

[104] B. Kienitz, J. Kolde, S. Priester, C. Baczkowski, and M. Crum, "Ultra-Thin Reinforced Ionomer Membranes to Meet Next Generation Fuel Cell Targets," *ECS Trans.*, vol. 41, no. 1, p. 1521, 2011.

[105] W. Liu, Y. Xie, J. Liu, X. Jie, J. Gu, and Z. Zou, "Experimental study of proton exchange membrane fuel cells using Nafion 212 and Nafion 211 for portable application at ambient pressure and temperature conditions," *Int. J. Hydrogen Energy*, vol. 37, no. 5, pp. 4673–4677, 2012.

[106] A. A. Shah, K. H. Luo, T. R. Ralph, and F. C. Walsh, "Recent trends and developments in polymer electrolyte membrane fuel cell modelling," *Electrochim. Acta*, vol. 56, no. 11, pp. 3731–3757, 2011.

[107] D. M. Bernardi and M. W. Verbrugge, "Mathematical model of a gas diffusion electrode bonded to a polymer electrolyte," *AIChE J.*, vol. 37, no. 8, pp. 1151–1163, 1991.

[108] D. M. Bernardi and M. W. Verbrugge, "A Mathematical Model of the Solid-Polymer-Electrolyte Fuel Cell," *J. Electrochem. Soc.*, vol. 139, no. 9, pp. 2477–2491, 1992.

[109] I. Terada and H. Nakagawa, "Polymer Electrolyte Fuel Cell," *Kobunshi*, vol. 57, no. 7, pp. 498–501, 2008.

[110] T. F. Fuller and J. Newman, "Water and Thermal Management in Solid-Polymer-Electrolyte Fuel Cells," *J. Electrochem. Soc.*, vol. 140, no. 5, pp. 1218–1225, 1993.

[111] M. Wöhr, K. Bolwin, W. Schnurnberger, M. Fischer, W. Neubrand, and G. Eigenberger, "Dynamic modelling and simulation of a polymer membrane fuel cell including mass transport limitation," *Int. J. Hydrogen Energy*, vol. 23, no. 3, pp. 213–218, 1998.

[112] N. Djilali and D. Lu, "Influence of heat transfer on gas and water transport in fuel cells," *Int. J. Therm. Sci.*, vol. 41, no. 1, pp. 29–40, 2002.

[113] J. J. Baschuk and X. Li, "Modelling of polymer electrolyte membrane fuel cells with variable degrees of water flooding," *J. Power Sources*, vol. 86, no. 1, pp. 181–196,

2000.

[114] T. Berning, D. M. Lu, and N. Djilali, “Three-dimensional computational analysis of transport phenomena in a PEM fuel cell,” 2002, vol. 106, no. 1–2, pp. 284–294.

[115] S. Dutta, S. Shimpalee, and J. W. Van Zee, “Three-dimensional numerical simulation of straight channel PEM fuel cells,” *J. Appl. Electrochem.*, vol. 30, no. 2, pp. 135–146, 2000.

[116] A. Z. Weber and J. Newman, “Effects of Microporous Layers in Polymer Electrolyte Fuel Cells,” *J. Electrochem. Soc.*, vol. 152, no. 4, p. A677, 2005.

[117] G. H. Guvelioglu and H. G. Stenger, “Computational fluid dynamics modeling of polymer electrolyte membrane fuel cells,” *J. Power Sources*, vol. 147, no. 1–2, pp. 95–106, 2005.

[118] V. Gurau, H. Liu, and S. Kakaç, “Two-dimensional model for proton exchange membrane fuel cells,” *AIChE J.*, vol. 44, no. 11, pp. 2410–2422, 1998.

[119] A. A. Shah, G. S. Kim, W. Gervais, A. Young, K. Promislow, J. Li, and S. Ye, “The effects of water and microstructure on the performance of polymer electrolyte fuel cells,” *J. Power Sources*, vol. 160, no. 2 SPEC. ISS., pp. 1251–1268, 2006.

[120] R. Roshandel and B. Farhanieh, “The effects of non-uniform distribution of catalyst loading on polymer electrolyte membrane fuel cell performance,” *Int. J. Hydrogen Energy*, vol. 32, no. 17, pp. 4424–4437, 2007.

[121] S. Shimpalee, S. Greenway, and J. W. Van Zee, “The impact of channel path length on PEMFC flow-field design,” *J. Power Sources*, vol. 160, no. 1, pp. 398–406, 2006.

[122] S.-W. Cha, R. O’Hayre, S. J. Lee, Y. Saito, and F. B. Prinz, “Geometric Scale Effect of Flow Channels on Performance of Fuel Cells,” *J. Electrochem. Soc.*, vol. 151, no. 11, p. A1856, 2004.

[123] H. Ju, H. Meng, and C. Y. Wang, “A single-phase, non-isothermal model for PEM fuel cells,” *Int. J. Heat Mass Transf.*, vol. 48, no. 7, pp. 1303–1315, 2005.

[124] H. Ju, C.-Y. Wang, S. Cleghorn, and U. Beuscher, “Nonisothermal Modeling of Polymer Electrolyte Fuel Cells,” *J. Electrochem. Soc.*, vol. 153, no. 2, p. A249, 2006.

[125] H. Meng, “A PEM fuel cell model for cold-start simulations,” *J. Power Sources*, vol. 178, no. 1, pp. 141–150, 2008.

[126] L. Mao and C.-Y. Wang, “Analysis of Cold Start in Polymer Electrolyte Fuel Cells,” *J. Electrochem. Soc.*, vol. 154, no. 2, p. B139, 2007.

[127] A. Z. Weber and J. Newman, “Transport in Polymer-Electrolyte Membranes,” *J. Electrochem. Soc.*, vol. 150, no. 7, p. A1008, 2003.

[128] H. Meng, “Numerical investigation of transient responses of a PEM fuel cell using

a two-phase non-isothermal mixed-domain model," *J. Power Sources*, vol. 171, no. 2, pp. 738–746, 2007.

[129] Y. Wang and C.-Y. Wang, "Two-Phase Transients of Polymer Electrolyte Fuel Cells," *J. Electrochem. Soc.*, vol. 154, no. 7, p. B636, 2007.

[130] A. Theodorakakos, T. Ous, M. Gavaises, J. M. Nouri, N. Nikolopoulos, and H. Yanagihara, "Dynamics of water droplets detached from porous surfaces of relevance to PEM fuel cells," *J. Colloid Interface Sci.*, vol. 300, no. 2, pp. 673–687, 2006.

[131] X. G. Yang, F. Y. Zhang, A. L. Lubawy, and C. Y. Wang, "Visualization of Liquid Water Transport in a PEFC," *Electrochem. Solid-State Lett.*, vol. 7, no. 11, p. A408, 2004.

[132] J. U. Brackbill, D. B. Kothe, and C. Zemach, "A continuum method for modeling surface tension," *J. Comput. Phys.*, vol. 100, no. 2, pp. 335–354, 1992.

[133] P. J. Sarma, C. L. Gardner, S. Chugh, A. Sharma, and E. Kjeang, "Strategic implementation of pulsed oxidation for mitigation of CO poisoning in polymer electrolyte fuel cells," *J. Power Sources*, vol. 468, no. June, p. 228352, 2020.

[134] A. P. Sasmito, K. W. Lum, E. Birgersson, and A. S. Mujumdar, "Computational study of forced air-convection in open-cathode polymer electrolyte fuel cell stacks," *J. Power Sources*, 2010.

[135] A. P. Sasmito, E. Birgersson, and A. S. Mujumdar, "A novel flow reversal concept for improved thermal management in polymer electrolyte fuel cell stacks," *Int. J. Therm. Sci.*, vol. 54, pp. 242–252, 2012.

[136] A. P. Sasmito, K. W. Lum, E. Birgersson, and A. S. Mujumdar, "Computational study of forced air-convection in open-cathode polymer electrolyte fuel cell stacks," *J. Power Sources*, vol. 195, no. 17, pp. 5550–5563, 2010.

[137] S. Shahsavari, M. Bahrami, and E. Kjeang, "Computational analysis of heat transfer in air-cooled fuel cells," 2011, pp. 799–808.

[138] S. Shahsavari, A. Desouza, M. Bahrami, and E. Kjeang, "Thermal analysis of air-cooled PEM fuel cells," *Int. J. Hydrogen Energy*, vol. 37, no. 23, pp. 18261–18271, 2012.

[139] M. A. Tadbir, S. Shahsavari, M. Bahrami, and E. Kjeang, "Thermal management of an air-cooled PEM fuel cell: Cell level simulation," 2012, pp. 453–459.

[140] M. Andisheh-Tadbir, A. Desouza, M. Bahrami, and E. Kjeang, "Cell level modeling of the hygrothermal characteristics of open cathode polymer electrolyte membrane fuel cells," *Int. J. Hydrogen Energy*, vol. 39, no. 27, pp. 14993–15004, 2014.

[141] Q. Meyer, A. Himeur, S. Ashton, O. Curnick, R. Clague, T. Reisch, P. Adcock, P. R. Shearing, and D. J. L. Brett, "System-level electro-thermal optimisation of air-

cooled open-cathode polymer electrolyte fuel cells: Air blower parasitic load and schemes for dynamic operation," 2015, vol. 40, no. 46, pp. 16760–16766.

[142] Q. Meyer, K. Ronaszegi, J. B. Robinson, M. Noorkami, O. Curnick, S. Ashton, A. Danelyan, T. Reisch, P. Adcock, R. Kraume, *et al.*, "Combined current and temperature mapping in an air-cooled, open-cathode polymer electrolyte fuel cell under steady-state and dynamic conditions," *J. Power Sources*, vol. 297, pp. 315–322, 2015.

[143] Q. Meyer, K. Ronaszegi, G. Pei-June, O. Curnick, S. Ashton, T. Reisch, P. Adcock, P. R. Shearing, and D. J. L. Brett, "Optimisation of air cooled, open-cathode fuel cells: Current of lowest resistance and electro-thermal performance mapping," *J. Power Sources*, 2015.

[144] R. Flückiger, A. Tiefenauer, M. Ruge, C. Aebi, A. Wokaun, and F. N. Büchi, "Thermal analysis and optimization of a portable, edge-air-cooled PEFC stack," *J. Power Sources*, vol. 172, no. 1, pp. 324–333, 2007.

[145] N. Khajeh-Hosseini-Dalasm, M. J. Kermani, D. G. Moghaddam, and J. M. Stockie, "A parametric study of cathode catalyst layer structural parameters on the performance of a PEM fuel cell," *Int. J. Hydrogen Energy*, vol. 35, no. 6, pp. 2417–2427, 2010.

[146] H. Wu, P. Berg, and X. Li, "Steady and unsteady 3D non-isothermal modeling of PEM fuel cells with the effect of non-equilibrium phase transfer," *Appl. Energy*, vol. 87, no. 9, pp. 2778–2784, 2010.

[147] F. Brèque, J. Ramousse, Y. Dubé, K. Agbossou, and P. Adzakpa, "Sensibility study of flooding and drying issues to the operating conditions in PEM Fuel Cells," *Int. J. Energy Environ. IJEE*, vol. 1, no. 1, pp. 1–20, 2010.

[148] A. Sagar, S. Chugh, K. Sonkar, A. Sharma, and E. Kjeang, "A computational analysis on the operational behaviour of open-cathode polymer electrolyte membrane fuel cells," *Int. J. Hydrogen Energy*, vol. 45, no. 58, pp. 34125–34138, Oct. 2020.

[149] A. Sagar, S. Chugh, A. Sharma, and E. Kjeang, "Strategic ionomer design for high performing fuel cells with open cathode," *Int. J. Hydrogen Energy*, vol. 47, no. 3, pp. 1940–1946, 2022.

[150] Y. Li, N. Linnell Schwab, R. M. Briber, J. A. Dura, and T. Van Nguyen, "Modification of Nafion's nanostructure for the water management of PEM fuel cells," *J. Polym. Sci.*, vol. 61, no. 8, pp. 709–722, 2023.

[151] Y. Li and T. Van Nguyen, "A One-Dimensional Model of a PEM Fuel Cell with the Cathode Catalyst Layer Hydrophobically Treated for Water Management," *J. Electrochem. Soc.*, vol. 169, no. 11, p. 114505, 2022.

Appendices

Appendix A

A computational analysis on the operational behaviour of open-cathode polymer electrolyte membrane fuel cells

Available online at www.sciencedirect.com

ScienceDirect

journal homepage: www.elsevier.com/locate/he

A computational analysis on the operational behaviour of open-cathode polymer electrolyte membrane fuel cells

Anand Sagar [a,b], *Sachin Chugh* [b], *Kapil Sonkar* [b], *Alok Sharma* [b], *Erik Kjeang* [a,*]

[a] *School of Mechatronic Systems Engineering, Simon Fraser University, 250-13450 102 Avenue, Surrey, BC, V3T 0A3, Canada*

[b] *Alternative Energy Department, Indian Oil R&D Centre, Sector-13, Faridabad, 121002, India*

HIGHLIGHTS

- A 3D computational model is developed and validated for open-cathode fuel cells.
- The model reveals the unique hygrothermal characteristics of open-cathode cells.
- Specific differences between liquid cooled and open-cathode cells are investigated.
- Membrane drying and slow kinetics cause inferior performance in open-cathode cells.

GRAPHICAL ABSTRACT

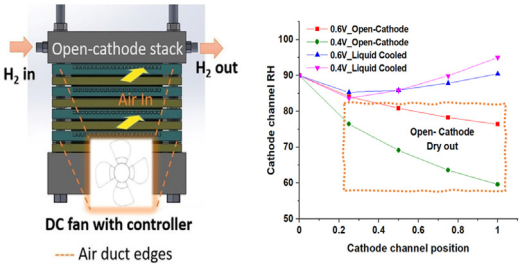

ARTICLE INFO

Article history:
Received 2 June 2020
Received in revised form
11 September 2020
Accepted 17 September 2020
Available online 12 October 2020

Keywords:
Fuel cell
Open cathode
Air cooling
Performance
Modelling
Simulation

ABSTRACT

In the present work, a comprehensive, three-dimensional computational fuel cell model is developed, validated, and utilized to study the operational and hygrothermal behaviour of an open-cathode (air cooled) polymer electrolyte membrane fuel cell at various ambient conditions compared to conventional liquid cooled cells and a hypothetical isothermal case. The spatial distributions of relative humidity, temperature, and membrane water content are analysed during operation of the cell and the strong hygrothermal characteristic of the open-cathode fuel cell system is established. The high temperature and relative humidity gradients inside the cell are found to limit the cell performance for open-cathode cells unlike the other operational cases. Moderate self-heating followed by membrane drying is found to be the key factor limiting the net cell performance while in operation at moderate-to-high current densities and high air flow rates. The open-cathode fuel cell is also found to perform better at high temperature and high relative humidity ambient conditions; however, in contrast to liquid cooled cells, the performance is restricted by inefficient thermal and water management.

* *Corresponding author.*
E-mail address: ekjeang@sfu.ca (E. Kjeang).

https://doi.org/10.1016/j.ijhydene.2020.09.133

Introduction

Polymer electrolyte membrane fuel cells (PEMFCs) are as the most commonly used fuel cell technology due to their low temperature operational regime, high efficiency and power density, and convenient stacking for various applications ranging from portable to automotive and stationary power. The PEMFC technology features significant environmental benefits and generates heat and water as the only by-products in contrast to the severe emissions produced by internal combustion engines. However, the present cost of the PEMFC system is currently a constraint for its propagation in commercial markets due to the high cost of membrane electrode assembly (MEA) materials, bipolar plates (BPPs), as well as balance of plant (BOP) components. The BOP components have been found to add nearly 34% of the overall system cost designed for transportation applications [1]. The cost incurred by the gas humidifiers [2], air compressor, heat exchanger, and liquid coolant loop in a generic liquid cooled PEMFC system contributes a major portion of the overall BOP cost. Alternatively, an open-cathode system which uses ambient air as both oxidant and coolant may considerably reduce the cost by eliminating several BOP components and offer a simplified system design [3].

Open-cathode fuel cells generally operate without air humidification and compression using a fan or blower to supply ambient air to the stack. The relatively low performance of an open-cathode cell compared to a conventional pressurized cell has been attributed to the low operating air pressure provided by the fan, which results in reduced reaction rate and increased cathode activation overpotential due to lower oxygen partial pressure [4]. The open-cathode stack performance was also reported to be influenced by the ambient air temperature [5]; where elevated temperature resulted in improved electrochemical reaction kinetics and mass transport rates. However, at the same time the excess generated reaction heat resulted in dehydration of the membrane. Thus, operating an open-cathode system at moderate temperature was suggested. A case study considering the monthly ambient air conditions of UAE in terms of varying temperature and humidity was reported by Zeyoudi et al. [6]. The stack temperature for an open-cathode system was dependent on the ambient temperature with hot and humid ambient conditions giving highest cell performance due to increased reaction kinetics and optimum membrane hydration, whereas hot and arid ambient conditions caused the lowest performance due to membrane drying. The gas diffusion layer (GDL) properties were reported to affect the mass transport performance of open-cathode cells; the porosity influenced the rate of gas phase mass transport, whereas the water removal from the catalyst layer (CL) to the flow channel was limited by the Polytetrafluoroethylene (PTFE) content [7]. The use of higher air flow rate was found to improve the water removal, though the excess air flow could cause membrane dehydration due to water evaporation from the membrane resulting in reduced stack performance. Hence, optimization of GDL porosity along with PTFE content and air flow rate was recommended as a strategy to enhance open-cathode performance. The water management in the open-cathode system was studied by Liu et al. [8] considering the effects of different CL composition, carbon loading in the microporous layer (MPL), and membrane thickness. The thicker CL with lower Pt loading was found to inhibit the cell performance due to reduced proton conductivity and mass transport. However, increased carbon loading in the MPL along with thinner membrane was found to aid the cell performance due to improved water retention. The use of less porous gas diffusion media for an open-cathode cell was also reported to increase current density due to reduced ohmic cell resistance [9]. The operation of open-cathode cells is also influenced by the cathode channel dimensions [10]. An increased channel width improved the water removal rate because of higher evaporation rate and increased air flow rate. However, at lower operating temperatures flooding was found to be the limiting factor for cell performance.

The two-dimensional computational model for open-cathode PEMFCs developed by Sasmito et al. demonstrated the strong impact of fan power and pressure drop on cell performance. Simulations also suggested that periodic flow reversal by dual fans operated in blowing and suction mode may enhance cell performance by improved thermal management [11–13]. Shahsavari et al. [14,15] developed a 3D numerical thermal model to establish the thermal analysis of open-cathode PEMFCs; the model was simplified by considering a periodic channel/rib domain and treating the cathode as a heat source without modelling fuel cell performance. Following experimental validation of the model, they reported critical coupling between temperature and humidity distribution in open-cathode cells and significant temperature gradients in the flow direction. Using a larger modelling domain, Andisheh-Tadbir et al. [16,17] predicted the hygro-thermal characteristics in a full open-cathode cell. The airflow conditions and in-plane thermal conductivity of the BPP were reported to affect the temperature and humidity distributions inside the cell, while edge cooling was deemed undesirable due to higher lateral gradients of temperature and humidity within the cell. The use of an electro-thermal performance mapping concept was illustrated by Meyer et al. [18–20] using current density and temperature data obtained with a sensor embedded plate. They concluded that the reactant consumption gradients guide the current density distribution in the low current density regime, whereas the cell temperature dictates the current density distribution in the high current density regime. Increased air flow rate was found to raise cell performance by providing increased oxygen supply and improved stack cooling. Additionally, lower temperature and

higher flow rate were determined to improve membrane hydration [21].

Given the intricate coupling of open-cathode fuel cell performance with operating conditions, thermal and water management, and complex gradients within the cell, further research in this field would benefit from a systematic, comprehensive modelling effort using a complete three-dimensional fuel cell model. The objective of the present work is therefore to develop and validate a 3D open-cathode fuel cell model that can resolve the coupling of electrochemical cell performance and hygrothermal conditions while also capturing the key gradients across the cell. This model will subsequently be used to investigate and explain the peculiar operational characteristics of open-cathode cells compared to conventional liquid-cooled cells and determine the underlying fundamental phenomena and key factors responsible for their relatively low performance. Experimental testing of open-cathode fuel cells with hygrothermal diagnostics is also performed in order to adequately validate the model and provide inferences for the operational characteristics predicted by the model.

Model development

A three-dimensional computational model is developed in the present work to understand the operational behaviour of an open-cathode PEMFC and to analyse the impact of operating conditions on cell performance. The model developed is a generic three-dimensional PEM fuel cell model and can alternatively be used to simulate liquid-cooled or open-cathode cell performance based on discrete boundary conditions provided to the model. Similarly to liquid-cooled fuel cells, the open-cathode stack consists of repetitive cells with repetitive reactant gas channels normally aligned in parallel. The main interest of the study lies in investigating the key parameters responsible for the inferior performance of an open-cathode system as compared to a similar liquid-cooled system and identify any localized drying/hot zones present in the system for various operating environments. Hence, a periodic, representative unit cell domain is defined, comprising of a single pair of central cathode and anode channels with plate and MEA within a central cell in the stack. Taking symmetry of the fuel cell geometry into account, half channel and half rib parts on each side of the MEA are resolved and considered as the computational domain, as depicted in Fig. 1.

Open-cathode PEMFCs are generally operated at higher air flow rates corresponding to higher stoichiometry, where the air to the cell is provided by means of a fan/blower attached to the cell assembly connected by a duct/air-plenum. Assuming that the fan/blower provides uniform flow at the entrance of the cell, the corresponding air flow rate is provided as an input condition to the model. The computational domain is divided into nine subdomains with upper part being anode and lower part as cathode, as described in Fig. 1(c). The BPP is also featured in the model since it contributes to heat modulation. The MEA is configured between closed anode flow channels and open-cathode flow channels. The MEA further comprises of anode and cathode GDLs and CLs with polymeric membrane sandwiched in between. The flow configuration can be decided by the user based on the inlet and outlet conditions provided to the model. However, in the present study the flow is assumed to be in co-flow mode. Table 1 lists the dimensions of the different domains described.

Model assumptions

The steady state model development is based on the following main assumptions:

1. The flow is incompressible and laminar because of low Re.
2. The gaseous mixtures are assumed to be ideal gases.
3. The crossover of fuel from anode to cathode side is assumed to be negligible considering impermeable membrane.
4. The contact resistances between respective interfaces are considered minimal and hence neglected.
5. The product water formed is assumed to be produced in vapour phase given the low relative humidity (RH) of the gases.

Governing equations

The conservation of mass, momentum, and species equations as described by (1), (2), and (3), respectively, are solved where applicable across the various subdomains.

$$\nabla.(\rho u) = S_{mass} \tag{1}$$

$$\rho u.\nabla u = -\nabla P + \mu\nabla^2 u + S_{mom} \tag{2}$$

$$u.\nabla c_i = \nabla.\left(D_{eff}\nabla c_i\right) + S_{mol} \tag{3}$$

Here, 'ρ' is the mixture density, 'u' is the velocity vector, 'S_{mass}' is the mass source term, 'P' is the pressure, 'μ' is the kinematic viscosity, 'S_{mom}' is the momentum source term, 'c_i' is the molar concentration of each chemical species, 'D_{eff}' is the effective gas diffusivity, and 'S_{mol}' is the molar source term for generation/consumption of different species in the respective domains.

$$\nabla.(\sigma_s\nabla\varphi_s) = -j_s \tag{4}$$

$$\nabla.(\sigma_m\nabla\varphi_m) = -j_m \tag{5}$$

The charge conservation described by (4) and (5) is simultaneously solved in the porous electrodes (GDLs and CLs) on both sides where 'σ_s' is the electrode electrical conductivity and 'σ_m' is the electrolyte phase ionic conductivity. 'φ_s', 'j_s' are the electrode potential and current density; whereas 'φ_m', 'j_m' are the electrolyte potential and current density respectively. In the membrane phase only (5) is being solved. The different modes of heat transport by conduction and convection are solved in the full domain by solving energy conservation according to (6) where 'T' is the local temperature, 'C_p' is the specific heat of the fluid, 'k_{eff}' is the effective thermal conductivity, and 'S_T' is the heat source term which constitutes heat generation inside the cell via entropic heat of reaction, irreversible heat of electrochemical reactions, and heat dissipation due to ohmic losses.

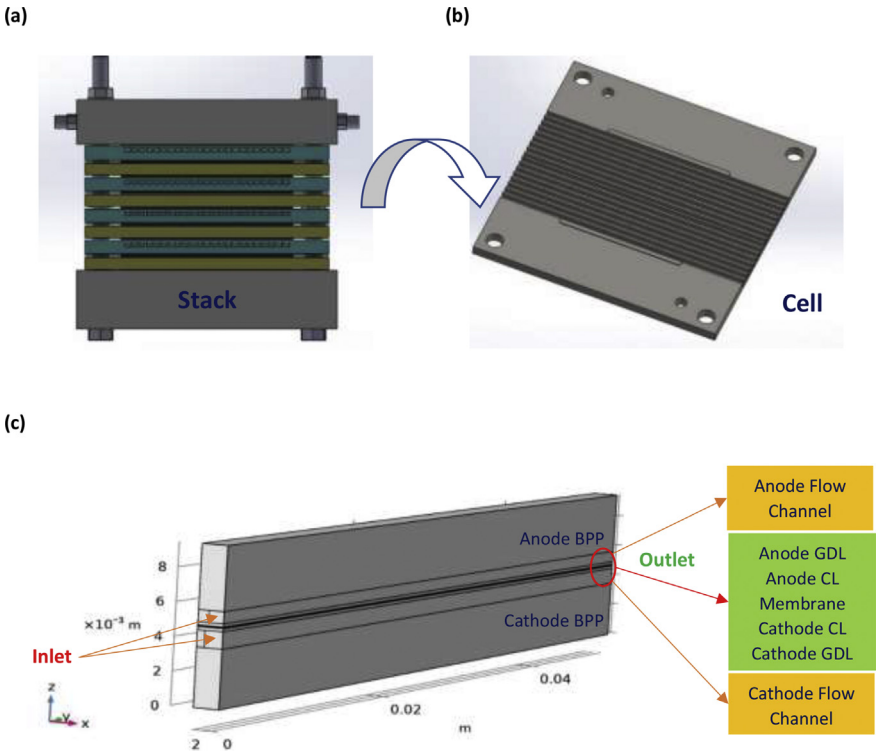

Fig. 1 – Schematics of an open-cathode fuel cell (a) stack and (b) cell. (c) The central channel pair of the central cell from the stack is designated as the computational domain for the present work.

$$\rho C_p u.\nabla T = \nabla.(k_{eff}\nabla T) + S_T \quad (6)$$

$$\nabla.(-D_d\nabla C_d) + \nabla.\left(\frac{n_d}{F}j_m\right) = S_d \quad (7)$$

Two-phase water transport is adopted with vapour and dissolved phase (in ionomer) being the two phases in which water can be present. Liquid phase water is neglected, provided that RH is kept below 100%. The vapour phase water transport is solved in gas channels, GDLs, and CLs whereas dissolved phase water transport is solved in CLs and membrane. The water balance is governed by (7) where 'n_d' is the electro-osmotic drag coefficient, 'j_m' is the electrolyte current density, 'D_d' is the back-diffusion coefficient, 'S_d' is the source term, and 'C_d' is the net water concentration in the dissolved phase being calculated from the water content 'λ', membrane density 'ρ_m', and membrane equivalent weight 'EW' using (8).

The local water content in the CLs and membrane is calculated based on the net osmotic drag and diffusion between anode and cathode CLs. The water uptake by the ionomer phase present in the CLs is calculated by (9) which is proportional to the gradient of local water content 'λ' and equilibrium water content 'λ_e' which is a function of vapour phase saturation 'a' as described in (10). 'γ_a' and 'γ_c' are the sorption/desorption rate constants respectively on anode CL and cathode CL. The vapour phase saturation is dependent on the local saturation pressure 'P_{sat}' and calculated using (11) and (12) where 'x_{H_2O}' is the local water mole fraction, 'P' is the local pressure and 'T' is the local temperature [22–24]. The source terms are defined in Table 2.

$$C_d = \frac{\lambda^* \rho_m}{EW} \quad (8)$$

Table 1 – Geometrical details of the computational domain.

Domain	Open-cathode cell			Liquid-cooled cell		
	Dimension			Dimension		
	Length (mm)	Width (mm)	Height (mm)	Length (mm)	Width (mm)	Height (mm)
Flow Channel (Anode/Cathode)	50	0.825/1.0	0.7/1.0	50	0.5/0.5	0.7/1.0
GDL (Anode/Cathode)	50	1.425	0.19	50	1.0	0.19
CL (Anode/Cathode)	50	1.425	0.015	50	1.0	0.015
Membrane	50	1.425	0.05	50	1.0	0.05
Ribs (Anode/Cathode)	50	0.6/0.425	0.7/1.0	50	0.5/0.5	0.7/1.0
BPP (Anode/Cathode)	50	1.425	3.8/3.5	50	1.0	3.8/3.5

Table 2 – Source terms used in the computational model.

	GDLs	Anode CL	Cathode CL	PEM
S_{mass}		$S_{mass,H_2} = S_{mol,H_2} * M_{H_2}$ $S_{mass,H_2O} = S_{mol,H_2O} * M_{H_2O}$	$S_{mass,O_2} = S_{mol,O_2} * M_{O_2}$ $S_{mass,H_2O} = S_{mol,H_2O} * M_{H_2O}$	
S_{mom}		$-\frac{\mu . u_a}{K}$	$-\frac{\mu . u_c}{K}$	
S_{mol}		$S_{mol,H_2} = -\frac{j_{s,a}}{2F}$	$S_{mol,O_2} = -\frac{j_{s,c}}{4F}$	
S_T	$\sigma_{s,eff} {\varphi_s}^2$	$S_{mol,H_2O} = -S_{d,a}$ $\sigma_{s,eff} {\varphi_s}^2$	$S_{mol,H_2O} = -\frac{j_{s,c}}{2F} - S_{d,c}$ $\sigma_{s,eff} {\varphi_s}^2$	$\sigma_{m,eff} {\varphi_m}^2$
S_d		$S_{d,a} = \gamma_a \frac{\rho_m}{EW} (\lambda_e - \lambda)$	$S_{d,c} = \gamma_c \frac{\rho_m}{EW} (\lambda_e - \lambda)$	

$$S_d = \begin{cases} S_{d,a} = \gamma_a \frac{\rho_m}{EW} (\lambda_e - \lambda) \\ S_{d,c} = \gamma_c \frac{\rho_m}{EW} (\lambda_e - \lambda) \end{cases} \quad (9)$$

$$\lambda_e = \begin{cases} 0.3 + 10.8\, a - 16\, a^2 + 14.1\, a^3 & a \le 1 \\ 14 + 1.4\,(a - 1) & 1 < a \le 3 \end{cases} \quad (10)$$

$$a = \frac{x_{H_2O} . P}{P_{sat}} \quad (11)$$

$$P_{sat} = -2846.4 + 411.24 * T(^\circ C) - 10.544 * T(^\circ C)^2 + 0.16636 * T(^\circ C)^3 \quad (12)$$

The electrochemical reactions at the anode and cathode CLs are modelled by calculating the electrode current densities as '$j_{s,a}$' and '$j_{s,c}$'. These terms are further deduced using the Butler-Volmer kinetics as described through (13) and (14) where 'α' is the charge transfer coefficient, 'R' is the gas constant, and 'η' is the electrode overpotential. The volumetric current densities '$j_{v,a}$' and '$j_{v,c}$' are calculated using (15) where 'a_v' is the active specific surface area [25]. In (16), 'ε_l' is the effective Pt surface area ratio, 'm_{Pt}' is the Pt loading, 'S_{Pt}' is the specific active area of Pt, 't_{CL}' is the CL thickness, and 'ε_{CL}' is the CL porosity.

$$j_{s,a} = j_{a_0} \left(\frac{C_{H_2}}{C_{H_{2,ref}}} \right)^{0.5} \left(e^{\frac{\alpha_a F \eta_a}{RT}} - e^{\frac{-\alpha_c F \eta_a}{RT}} \right) \quad (13)$$

$$j_{s,c} = j_{c_0} \left(\frac{C_{O_2}}{C_{O_{2,ref}}} \right) \left(e^{\frac{\alpha_a F \eta_c}{RT}} - e^{\frac{-\alpha_c F \eta_c}{RT}} \right) \quad (14)$$

$$j_{v,a} = j_{s,a} * a_v \; ; \; j_{v,c} = j_{s,c} * a_v \quad (15)$$

$$a_v = \frac{\varepsilon_l m_{Pt} S_{Pt}}{t_{CL}(1 - \varepsilon_{CL})} \quad (16)$$

Boundary conditions

The external boundaries of the computational model are subjected to boundary conditions relevant to the fuel cell operating conditions and periodic nature of the selected domain. The anode and cathode inlets are assigned fixed flow rate based on the stoichiometry of fuel and oxidant at the respective inlet temperatures. The full set of boundary conditions for the model is described in Table 3.

Other details

The various modelling parameters are taken from manufacturer's data of respective components/materials used for MEA preparation and BPP machining as listed in Table 4. With the model details as described above, the simulations are run on a Dell PC with Intel-Xenon 2.3 GHz processor using COMSOL Multiphysics 5.4. The Batteries and Fuel Cells Module in COMSOL is used to setup the governing physics and assign boundary conditions. The initial conditions are set to zero velocity and pressure, near inlet mole fraction and temperature across all domains, and potential equal to cell voltage on cathode side and ground potential on anode side as starting point for solution. The governing equations with boundary conditions are solved to achieve steady state solution for cell operation at a designated cell voltage. The steps for solution include individual segregated steps for each dependent variable and a fully coupled step for simultaneous solving of all governing equations. The adopted solver is a Direct segregated solver with relative convergence criterion of 10^{-3} for each dependent variable in the coupled step. The computational domain is meshed with 80% hexahedral and 20% quad mesh elements. The total number of degrees of freedom being solved for is 816529.

Grid-independence study

Grid independence is verified by solving the parametric case study (OCV to 0.3 V) for the open-cathode PEMFC with ambient air condition at 50 °C and 90% RH for three different mesh sizes, as listed in Table 5. The number of elements is quadrupled from case-I to case-III and the computational time is increased by nearly six times. However, the local temperature and RH are found to deviate by less than 0.05%. Hence, case-I with 33852 elements is considered to provide mesh-independent results for this study and is used for all further simulations reported in this work.

Experimental details

A single-cell open-cathode experimental setup with net active area of 25 cm^2 is assembled to measure the fuel cell performance at various operating conditions as described in Table 6. The single cell setup consists of two aluminium based end-plates, gold plated current collectors, graphite-based flow field

Table 3 – Boundary conditions for the computational model.

Governing Equation	Anode			Cathode		
	Inlet	Outlet	Other Boundaries	Inlet	Outlet	Other Boundaries
(2)	$\dot{V} = \dot{V}_{in,a}$	P = 1 atm	No flux	$\dot{V} = \dot{V}_{in,c}$	P = 1 atm	No flux
(3)	$x_{H_2,in} = 1 - \frac{P_{sat}}{P_{in,a}} \times RH_a \times RH_a$	Outflow	No flux	$x_{O_2,in} = 0.21 \times (1 - x_{H_2O,in})$ $x_{H_2O,in} = \frac{P_{sat}}{P_{in,c}} \times RH_c$	Outflow	No flux
(6)	$T = T_{in,a}$	Outflux	No flux	$T = T_{in,c}$	Outflux	No flux
	Periodic BC: $T_{top,\ anode\ side\ BPP} = T_{bottom,\ cathode\ side\ BPP}$					
(4)	GDL-BPP Interface: 0 V			GDL-BPP Interface: V_{cell}		
	Other Boundaries: No flux			Other Boundaries: No flux		

plates, and an MEA sandwiched in between. The flow field plates are machined with parallel flow configuration with closed anode channels and open cathode channels at the respective half-cells. The MEA consists of a Nafion NRE-212 membrane coated with 60% Pt/C catalyst with effective loading of 0.5 mg/cm^2 and ionomer loading of 30% (wt/wt %) on both sides supported by a Sigracet 29BC GDL. A 12V PWM-controlled Delta DC fan is attached to the cell assembly via an ABS plastic based duct as shown in Fig. 2(a) and operated by a power supply from the test bench. The whole setup is installed inside an environmental chamber in order for the DC axial fan to provide ambient air of desired temperature and humidity levels to the cell. The air flow rate provided by the DC fan is measured using a Testo 605i thermal anemometer by profiling the flow distribution across the duct outlet. The environmental chamber is connected to a Greenlight Innovation G60 PEMFC test station which maintains the desired inlet gas temperature, pressure, and humidification and records various data related to cell operation. The dry hydrogen on the anode side is provided to the cell using the same facility. Since the present work focuses on the effects of cathode airflow conditions on the operational behaviour of open-cathode cells, the anode side fuel is kept dry in order to replicate the expected operating environments of open-cathode systems without external humidifiers.

Thermal equilibrium

Thermal equilibrium for the open-cathode single cell experiments is ensured at each operating current density in order to achieve a self-heating scenario equivalent to full-scale stack operation. Three T-type thermocouples are inserted at different parts of the setup to monitor the local temperature: TC1 is placed in the central cathode flow channel at the cathode GDL interface; TC2 is inserted into the BPP perpendicularly to the cathode flow channels; and TC3 is inserted into the aluminium based endplate. While operating at individual currents from 1 to 5 A, various temperature data are recorded for TC1, TC2, and TC3 in the form of T1, T2, and T3 respectively. The system is insulated with glass wool wrapped around the outer periphery of the setup exposing only the cathode flow channels to the ambient. Fig. 2(b) shows the trends of T1, T2, and T3 for case-2 operated at 5 A with T1 > T2 > T3 indicating the direction of heat transfer outwards from the MEA to the flow channels and subsequently toward the BPP and endplate. The system is equilibrated for 30 min and the temperature rise is found to be less than 0.05 °C min^{-1}; hence achieving adequate thermal equilibrium for the purposes of the present work.

Operating conditions

The experimental setup is tested at different ambient conditions to establish the hygrothermal effect on the operational behaviour of the open-cathode system as listed in Table 6 (Case −1 to 4). The anode side H_2 with purity of 99.999% is kept relatively dry with 15% RH and the temperature is kept at the respective ambient temperature to demonstrate a physical cell operating condition. The anode flow rate is kept at 2.2 nlpm based on minimum mass flow constraints at the test station whereas the air flow rate is kept at 35 nlpm by the PWM controller. The cell is operated in co-flow mode for all experimental conditions. Current is extracted from the cell using a load bank and the polarization behaviour of the cell in operation is recorded. Electrochemical impedance spectroscopy (EIS) is performed in potentiostatic mode at 0.6 V (medium current density) sweeping between 15 kHz and 0.1 Hz with AC perturbation voltage of 5 mV to measure the combined ohmic cell resistance for each test condition using a Gamry Reference 3000 potentiostat interfaced with the test station.

In addition to cases-1 to 4; case-5 is operated on a liquid cooled setup with closed plates on both anode and cathode and additional water coolant plate on top of the cathode plate. To enrich the hygrothermal investigation, a hypothetical case-6 with isothermal conditions is also simulated to compare against the five experimental cases. The cell performance is recorded experimentally by polarization curve measurement in constant current mode starting from open circuit voltage (OCV) up to a maximum current density of 0.2 A cm^{-2} (5 A) with a step size of 1 A and hold time of 20 min at each step. Each polarization curve measurement is repeated three times in order to calculate average cell voltage and standard deviation, as represented through error bars.

Model validation

The experimental conditions in terms of MEA specifications, gas inlet conditions, and operating cell voltage are entered as input conditions into the computational model. The cell

Table 4 – List of modelling parameters.

Physical Property	Value	Units
Dynamic viscosity at anode	9.5×10^{-6}	Pa s
Dynamic viscosity at cathode	1.96×10^{-5}	Pa s
GDL Porosity	80	%
GDL Permeability	1.9×10^{-12} (IP)/7.0×10^{-12} (TP)	m^2
CL Porosity	30	%
CL Permeability	1.0×10^{-14}	m^2
CL electrical conductivity	450	S m^{-1}
GDL electrical conductivity	17500 (IP)/230 (TP)	S m^{-1}
Electrolyte volume fraction	0.2723	
Binary diffusion coefficient of H_2 –H_2O	0.915×10^{-4}	m^2 s^{-1}
Binary diffusion coefficient of N_2 –H_2O	0.256×10^{-4}	m^2 s^{-1}
Binary diffusion coefficient of O_2 –N_2	0.22×10^{-4}	m^2 s^{-1}
Binary diffusion coefficient of O_2 –H_2O	0.282×10^{-4}	m^2 s^{-1}
Exchange current density at anode electrode	50	A m^{-2}
Exchange current density at cathode electrode	1.2×10^{-4}	A m^{-2}
Effective platinum surface area ratio (ε_l)	0.6	
Platinum loading (m_{Pt})	0.5	mg cm^{-2}
Specific active area of platinum (S_{Pt})	30	m^2 g^{-1}
Charge transfer coefficient	0.5	
Thermal conductivity of fluid at anode	0.18	W m^{-1} K^{-1}
Thermal conductivity of fluid at cathode	0.03	W m^{-1} K^{-1}
Heat capacity at constant pressure of fluid at anode	1.44×10^4	J kg^{-1} K^{-1}
Heat capacity at constant pressure of fluid at cathode	1.01×10^3	J kg^{-1} K^{-1}
Ratio of specific heats of fluid at anode	1.41	
Ratio of specific heats of fluid at cathode	1.4	
Thermal conductivity of porous matrix GDL	21 (IP)/0.5 (TP)	W m^{-1} K^{-1}
Thermal conductivity of porous matrix CL	1.5	W m^{-1} K^{-1}
Density of porous matrix GDL	2.2×10^3	kg m^{-3}
Density of porous matrix CL	2.2×10^3	kg m^{-3}
Specific heat capacity of porous matrix GDL/CL	1.05×10^3	J kg^{-1} K^{-1}
Thermal conductivity of solid membrane	1.5	W m^{-1} K^{-1}
Thermal conductivity of anode/cathode BPP	75 (IP)/30 (TP)	W m^{-1} K^{-1}
Density of solid membrane	1.98×10^3	kg m^{-3}
Density of anode/cathode BPP	1.78	g cm^{-3}
Heat capacity at constant pressure of solid membrane	4.197×10^3	J kg^{-1} K^{-1}
Heat capacity at constant pressure of anode/cathode BPP	0.71×10^3	J kg^{-1} K^{-1}

IP – In-plane/TP – Through-plane.

voltage is varied from OCV to 0.3 V for cases- 1, 3, and 5 and to 0.4 V for cases- 2 and 4, respectively. The experiments are repeated for reproducibility and the experimental results with error bars are plotted together with the simulated results

Table 5 – Details of grid-independence test.

	Elements	Computational Time	Avg. Cathode Outlet RH (%) at 0.6 V	Avg. Cathode Outlet T (°C) at 0.6 V
Case-I	33852	39 min	76.832	52.841
Case-II	70308	1 h 35 min	76.854	52.834
Case-III	140616	3 h 39 min	76.87	52.83

obtained from the model in Fig. 3. The experimental variability is consistently less than 10%; as a reference, the standard deviation for case-2 at 0.6 V is 5 mV. The simulated results show consistent trends for most of the cases with good agreement with experimental results. For cases- 3 and 4 at 50 °C ambient temperature, the slight deviation (5–10%) between experimental and simulated results is attributed to the absorption/desorption rate constants for the membrane which were taken at room temperature. The simulated results for the liquid-cooled case shown in Fig. 3(e) are also in good agreement with the experimental results, with slight deviation in the mass transport region. The liquid water generated in this case (liquid-cooled) at the considerably higher current densities could be better captured with three phase water modelling, which is beyond the present scope on open-cathode cell operation where low current densities and dry conditions are prevalent.

Results and discussion

The polarization curve data for open-cathode (cases-1 to 4) and liquid-cooled PEMFC operation (case-5) obtained experimentally along with the simulated hypothetical isothermal case data (case-6) are compared in Fig. 4(a). The highest fuel cell performance across most cell voltages is achieved with the simulated isothermal case, which represents optimal thermal management within the cell at universally held temperature. Next, the second highest performance is accomplished with the liquid-cooled cell where the heat generated in the system is well managed by the water coolant which modulates the BPP temperature and extracts the heat efficiently. However, in all four cases of open-cathode PEMFC operation the thermal management is restricted by relatively

Table 6 – Operating conditions used for experimental evaluation of open-cathode fuel cells.

		Anode		Cathode	
		RH (%)	T (°C)	RH (%)	T (°C)
Open-cathode cell	Case-1	15	30	30	30
	Case-2	15	30	90	30
	Case-3	15	50	30	50
	Case-4	15	50	90	50
Liquid cooled cell	Case-5	50	50	90	50
Isothermal case	Case-6	50	50	90	50

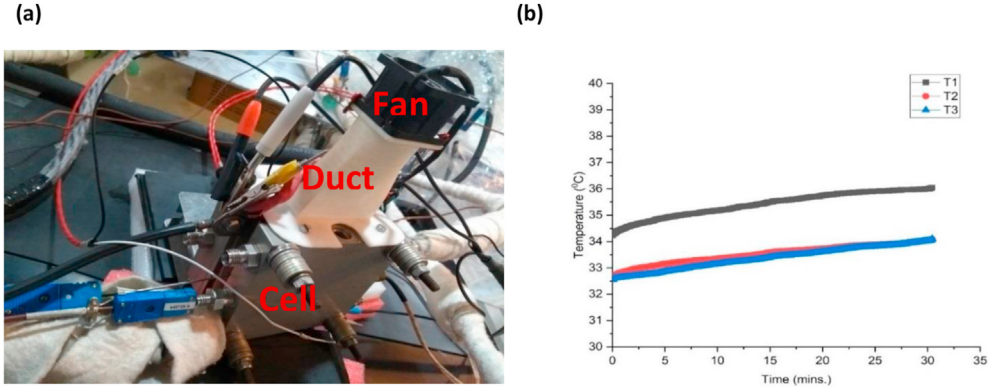

Fig. 2 – (a) Experimental setup for open-cathode fuel cell testing and (b) thermal equilibrium curves for case-2 operated at 5 A cell current.

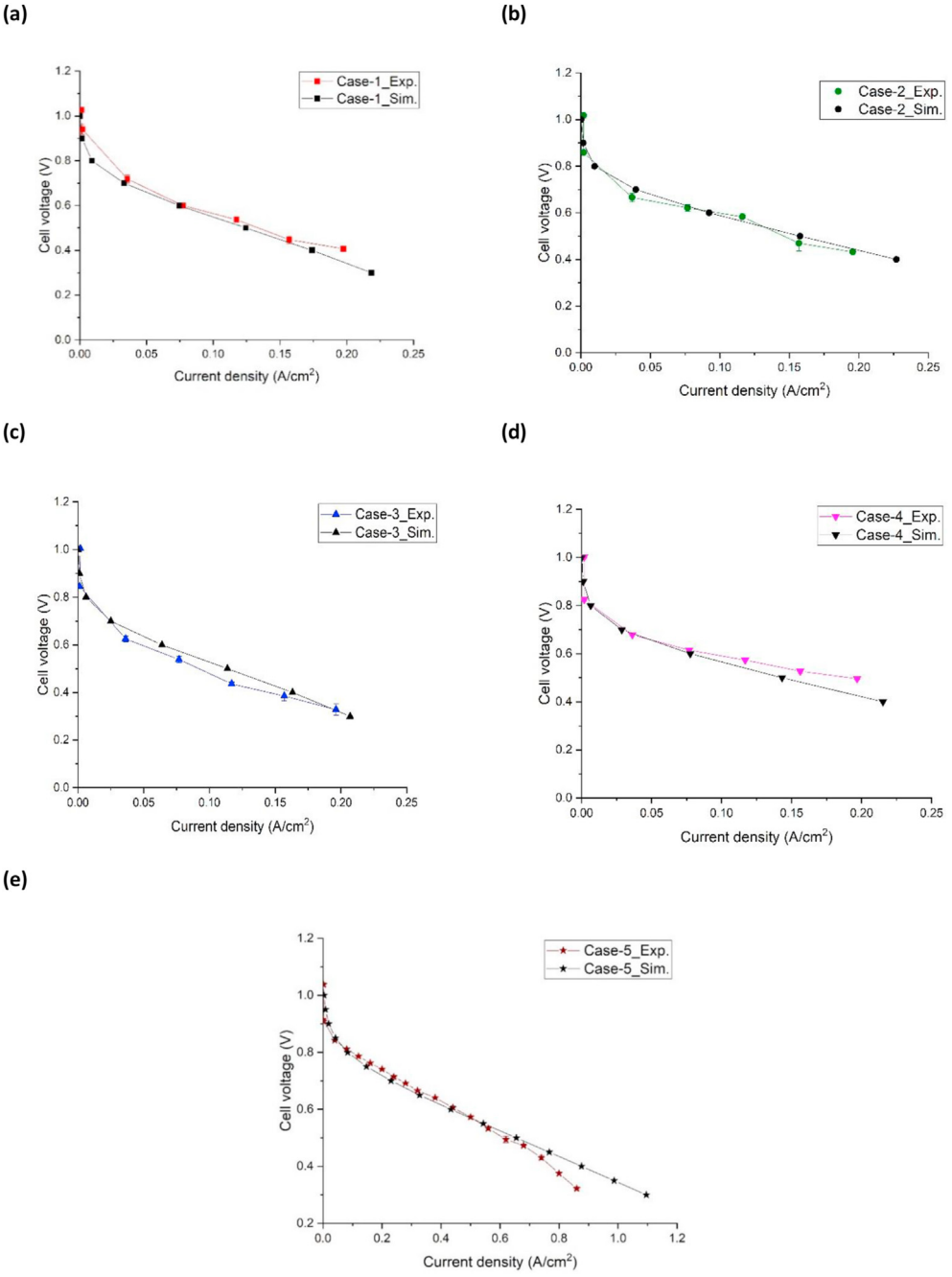

Fig. 3 – Model validation results for (a) case-1, (b) case-2, (c) case-3, (d) case-4, and (e) case-5.

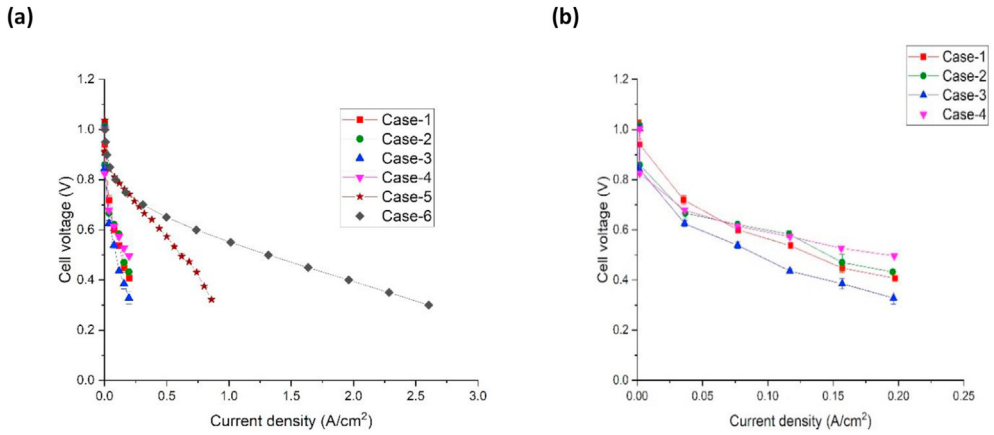

Fig. 4 – Comparative fuel cell polarization curves for (a) all cases studied and (b) open-cathode cases-1 to 4.

inefficient heat extraction and leads to inferior cell performance as compared to the other cases. The effect of ambient temperature and humidity on open-cathode cell performance is further illustrated in Fig. 4(b) where cases-1 to 4 are compared. The open-cathode cell generally reaches higher performance with increased air humidity at both 30 °C and 50 °C. The highest cell performance is achieved at 50 °C and 90% ambient humidity whereas the lowest performance is obtained for 50 °C and 30% ambient humidity. At low humidity, namely at 30%, the cell performs better at the lower ambient temperature of 30 °C than at 50 °C because of slightly improved hydration. These trends are further investigated in the subsequent sections in order to determine the underlying hygrothermal behaviour of the open-cathode cells and the fundamental reasons for their performance limitations compared to liquid-cooled cells.

Three hygrothermal metrics are selected to analyse and understand the cell dynamics, namely, the three gradients of RH (ΔRH_c), temperature (ΔT_c), and membrane water content ($\Delta\lambda_m$) from cathode inlet to outlet. These parameters are calculated in the validated computational model for all cases under study, except for the isothermal case which does not contain any temperature gradients. ΔT_c along the cathode channel, as depicted in Fig. 5, remains positive for all operating conditions, indicating that the air flow is absorbing heat

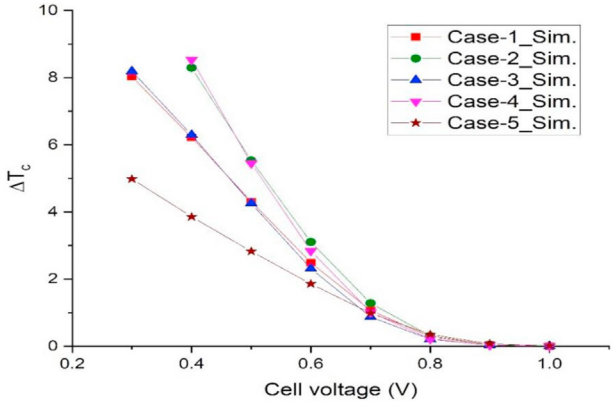

Fig. 5 – Temperature difference between inlet and outlet in the cathode air flow as a function of cell voltage.

from the cell. As expected, the lowest ΔT_c is observed for the liquid-cooled cell with a maximum value of ~5 °C at high current density operation (0.3 V). The comparable open-cathode result for case-4, having the same cathode inlet conditions, exhibits nearly a doubling in the temperature rise from inlet to outlet. The ΔT_c can be very high for open-cathode cells, particularly at low flow rates, given that the air flow is the primary heat dissipation mechanism for the cell. In the present study, however, the temperature rise was limited by the high air flow rate and the associated advective cooling effect. The higher ΔT_c for 90% RH condition leads to higher overall cell temperature which also helps in enhancing the cell kinetics as compared to cases of 30% inlet RH. This results in higher cell performance at higher inlet RH conditions.

The cell temperature profiles for cases-4 and 5 operated at medium current density (0.6 V) are shown in Fig. 6(b). The maximum cell temperature for the equivalent cases of open-cathode and liquid-cooled cells designated by cases-4 and 5, respectively, are comparable; however, the temperature distribution within the cell differs considerably in the two cases. In case-4, the open-cathode cell is operated at high flow rate of 35 nlpm and significant cooling is achieved which maintained the cell temperature within the 50–60 °C range whereas for case-5 a similar cell temperature range is maintained with lower flow rates. The highest temperature in the open-cathode cell is observed in the MEA under the rib and increases toward the outlet, whereas the MEA temperature under the rib for the liquid-cooled cell is close to the bulk BPP temperature.

The tip of the thermocouple 'TC1' is inserted in the central cathode channel at a distance of 3.2 cm from the inlet at the channel-GDL interface. The temperature 'T1' recorded experimentally is compared with the simulated average temperature in the cathode channel at the same location for each operating case at 5 A for the open-cathode cell. Fig. 7 shows the comparison which displays good overall agreement between model and experiment. The deviation between measured and simulated data is generally below 3.5 °C except for case-3 where the simulated temperature is nearly 7.5 °C higher than the experimental value. This deviation can be attributed to more drying observed in simulated case-3 as compared to experimental

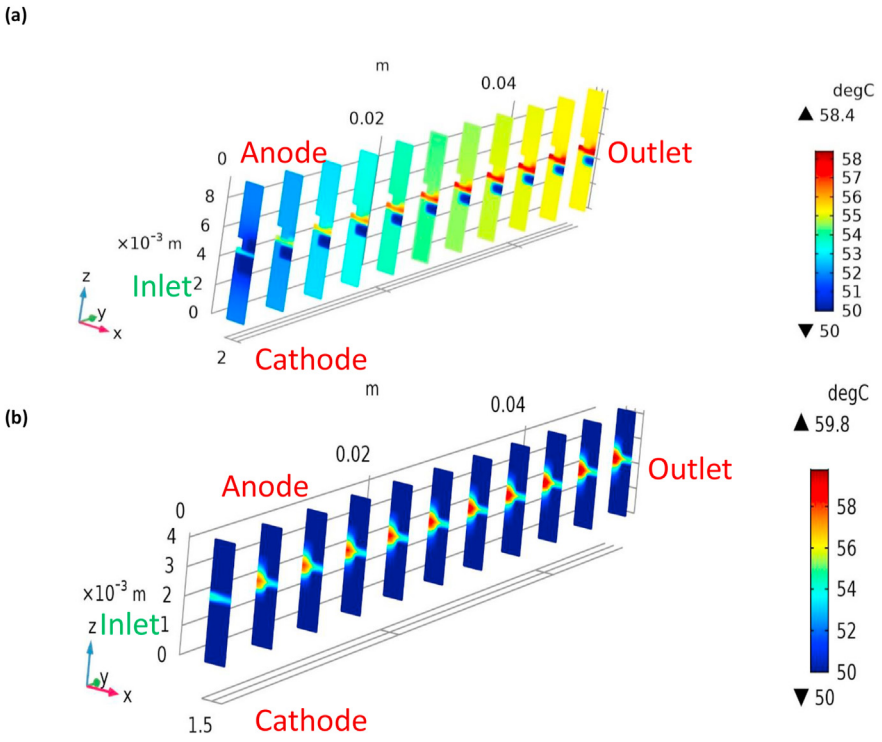

Fig. 6 – Cell temperature profiles for (a) case-4 and (b) case-5 at 0.6 V.

case-3 which is also evident from the deviation in the two polarization curves in Fig. 3(c).

ΔRH_c is calculated as the difference between average inlet and outlet RH in the cathode air flow, which is a strong indicator of hygral management of the cell as it shows the net direction and magnitude of water transport. A positive ΔRH_c corresponds to increased humidity level toward the outlet which suggests increased cell hydration, whereas negative ΔRH_c suggests drying in the cell. The trends shown in Fig. 8 reveal positive ΔRH_c for liquid-cooled and hypothetical isothermal cell operation at most cell voltages which results in enhanced cell hydration and even supersaturation in the latter case. Whereas, the opposite effect of negative ΔRH_c is observed for all open-cathode cases, which suggests drying in such systems despite net water production.

Fig. 9 illustrates the corresponding cathode RH distribution for cases-4 and 5 at 0.6 V. For case-4 of open-cathode operation with 90% inlet RH, the MEA part is relatively dry and there is no liquid water accumulation in the cell. The high air flow in this case helps maintain reasonable RH in the flow channel and contributes to cooling the cell; however, the other parts of the cell remain humidity deficient. Whereas, for liquid-cooled case-5 the cell remains hydrated throughout with local supersaturation under the cathode rib, where liquid water condensation and accumulation is likely. The combined effect

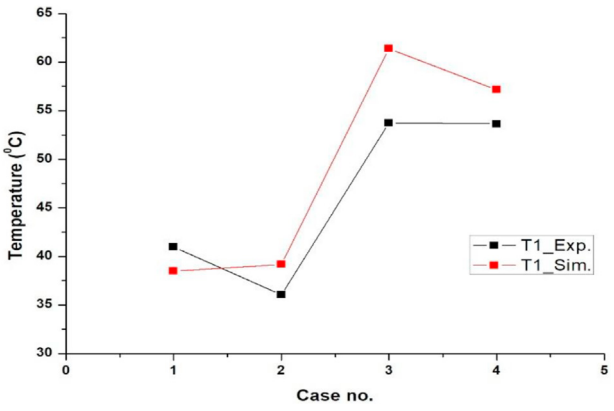

Fig. 7 – Measured and simulated temperature at location 'TC1' in the cathode channel, 3.2 cm from the inlet at the channel-GDL interface, for the four different open-cathode cases under study.

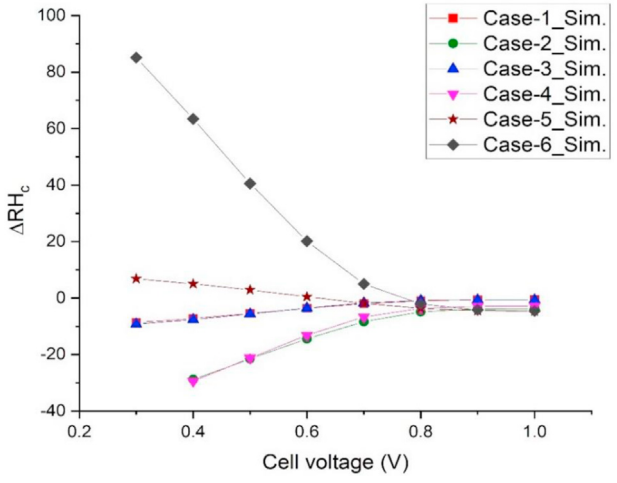

Fig. 8 – RH difference between inlet and outlet in the cathode air flow as a function of cell voltage.

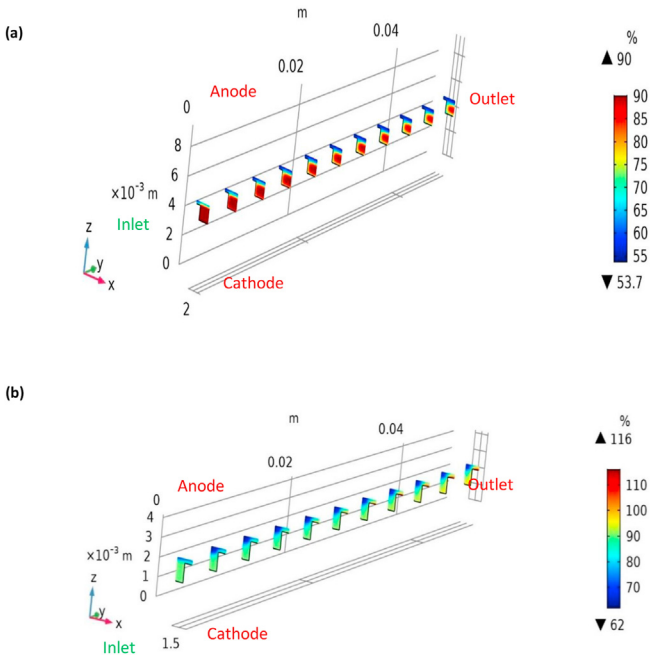

Fig. 9 – RH distribution profile for cathode flow channel, GDL, and CL for (a) case-4 and (b) case-5 at 0.6 V.

of ΔRH_c and ΔT_c leads to maximum cell performance for the 50 °C, 90% RH condition supported by enhanced cell kinetics and optimum saturation as reported in Fig. 4(b).

EIS measurements are taken for all cases at different current densities while obtaining the polarization data at the end of every current step. The impedance measurement data at 0.6 V (medium current density operation) are depicted in Fig. 10(a). The high frequency resistance (HFR) is recorded from the first (high frequency) x-axis intercept of the Nyquist plot, with data shown in Fig. 10(b). The HFR represents the combined ohmic cell resistance for the system which includes all ionic and electronic resistances. The electronic resistances being similar for all operating cases, the differences observed in the HFR data, as well as the changes with current density, are attributed to the membrane resistance and ionomer resistance in CLs. The ionic conductivity of Nafion membranes is strongly dependent on the cell temperature and membrane hydration; it increases exponentially with temperature and linearly with water content in the membrane [26].

Fig. 10(b) describes the quantitative trends of HFR for various operating cases which is directly related to the net water transport across the fuel cell. For cases-1 and 3 where the cathode stream is dry, the HFR is generally high and shows a steep decrement with increase in operating current density,

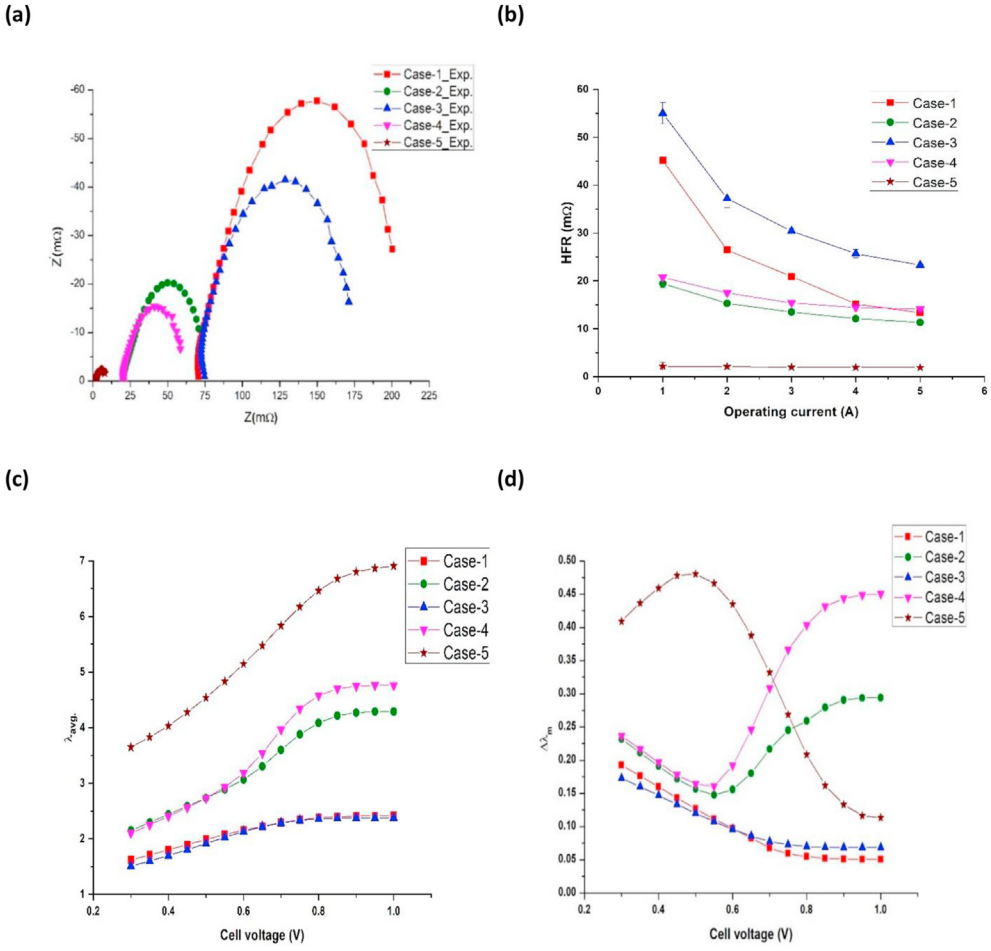

Fig. 10 – Impedance measurement through EIS: (a) Nyquist plot recorded at 0.6 V; and (b) high frequency resistance (HFR). Related modelling results for cases-1 to 5: (c) average water content in the membrane; and (d) water content gradient across the membrane as a function of cell voltage.

whereas the HFR drop is less significant for cases-2 and 4 with fully humidified cathode stream. A similar trend is also seen for case-5, where the HFR remains nearly constant at all operating currents. Collectively, these results demonstrate that a fully humidified cathode stream is sufficient to ensure membrane hydration regardless of the cell current, while for the dry cathode stream, a moderate to high current with substantial rate of water production is required in order to achieve sufficient ionomer and membrane hydration.

The simulated average membrane water content (λ_{avg}), as depicted in Fig. 10(c), also follows the HFR trends from Fig. 10(b); as expected, the liquid-cooled case-5 has the highest membrane water content followed by the humidified cases-2 and 4, whereas the dry cathode stream cases-1 and 3 have considerably lower λ_{avg}. The water content gradient ($\Delta\lambda_m$) between the cathode and anode sides of the membrane is calculated by taking the difference of their average values, with results shown in Fig. 10(d). The consistently positive gradient represents higher water content on the cathode side compared to the anode side, which is a result of the relatively dry hydrogen used in this work. The dry anode thus consistently suppresses membrane hydration by evaporative water loss into the anode stream for all cases studied here. However, back-diffusion of water to the anode may to some extent also aid membrane hydration compared to direct water loss from the cathode catalyst layer into the cathode air stream. For the humidified cases-2 and 4, back-diffusion is particularly high at low current densities (high cell voltages), whereas the water-cooled case-5 experiences the highest back-diffusion at high current densities with more water production at the cathode side. In contrast, cases-1 and 3 have relatively low rate of back-diffusion due to the dry cathode air stream which absorbs more water than for the other cases. Here, the dry anode and cathode streams both contribute to the overall inferior membrane hydration across all current densities.

The diameter of the semi-circle of the Nyquist plot as shown in Fig. 10(a) quantifies the charge transfer resistance (R_{ct}) possessed by the system at 0.6 V while operating at various ambient conditions. The liquid-cooled case-5 has the least R_{ct} followed by the humidified open-cathode cases-2 and 4 while the highest R_{ct} is observed for the dry cases-1 and 3. The low R_{ct} for case-5 is attributed to its much higher current density as well as its thermal and hygral modulation. The moderate R_{ct} of cases-2 and 4 also benefited from elevated temperature combined with reasonable hydration characteristics, whereas the poor hydration for cases-1 and 3 resulted in high R_{ct} and inferior overall performance. It is hence inferred that both elevated temperature and good hydration are required for open-cathode PEMFCs to achieve low R_{ct}. Overall, these experimental and simulated findings highlight the coupling of thermal and hygral distributions inside the cell and their joint effects on fuel cell performance by guiding the ohmic resistance and kinetics of the system.

Conclusions

In the present work, a two-phase three-dimensional computational model was developed and validated experimentally in order to investigate the coupling of transport phenomena and cell performance in open-cathode PEMFCs. The same model was also used to evaluate the cell performance behaviour of a liquid-cooled PEMFC and later compared with open-cathode PEMFC performance at similar operating conditions. As expected, the open-cathode PEMFC performance was found to be inferior compared to liquid-cooled operation. This gap in cell performance was further evaluated based on modelling results for thermal and hygral distributions within the cell and water content in the membrane. The boost in cell performance for the liquid-cooled condition was attributed to well posed temperature and hydration modulation in the system across low to high current densities, whereas for the open-cathode system the cell performance was highly dependent on the ambient conditions of the air stream and controlled by the unique hygrothermal characteristics of the cell. The primary underlying reasons for low open-cathode cell performance were ascribed to relatively high ohmic resistance and slow electrochemical kinetics. The high ohmic loss was associated with high membrane ionic resistance due to poor membrane hydration at all cases under study, which was verified experimentally by high frequency resistance measurements. The kinetics were found to be negatively affected by low cell temperature in the cases of low ambient air temperature and by poor ionomer hydration in the cases for which higher cell temperature was achieved. Consequently, increased ambient relative humidity at elevated temperature was found to enhance the cell performance by decreasing the charge transfer resistance and increasing the water content of the membrane. Moreover, the anode RH was also found to be important in determining the overall hydration level in the cell and needs to be considered for design and operation of open-cathode PEMFCs. In our future work, various operational and design strategies will be investigated to bridge the performance gap between open-cathode and liquid-cooled fuel cells by means of enhanced thermal and water management of the system.

CRediT authorship contribution statement

Anand Sagar: Writing - original draft, Methodology, Investigation, Validation, Formal analysis. **Sachin Chugh:** Conceptualization, Resources, Supervision, Funding acquisition. **Kapil Sonkar:** Methodology, Validation. **Alok Sharma:** Project administration, Funding acquisition. **Erik Kjeang:** Writing - review & editing, Conceptualization, Resources, Supervision, Funding acquisition.

Declaration of competing interest

The authors declare that they have no known competing financial interests or personal relationships that could have appeared to influence the work reported in this paper.

Acknowledgments

This work was supported by Indian Oil R&D Centre, Faridabad, India and Simon Fraser University, Canada under the SFU-

IOCL joint PhD program in clean energy. This research was undertaken, in part, thanks to funding from the Canada Research Chairs program.

REFERENCES

[1] Carlson EJ, Kopf P, Sinha J, Sriramulu S, Yang Y. Cost analysis of PEM fuel cell systems for transportation. Natl Renew Energy Lab 2005;(December). https://doi.org/10.2172/862302. NREL/SR-560-39104.

[2] Kim BJ, Kim MS. Studies on the cathode humidification by exhaust gas recirculation for PEM fuel cell. Int J Hydrogen Energy Mar. 2012;37(5):4290–9. https://doi.org/10.1016/j.ijhydene.2011.11.103.

[3] Zhang G, Kandlikar SG. A critical review of cooling techniques in proton exchange membrane fuel cell stacks. Int J Hydrogen Energy 2012;37(3):2412–29. https://doi.org/10.1016/j.ijhydene.2011.11.010.

[4] Wu J, Galli S, Lagana I, Pozio A, Monteleone G, Yuan XZ, Martin J, Wang H. An air-cooled proton exchange membrane fuel cell with combined oxidant and coolant flow. J Power Sources 2009;188(1):199–204. https://doi.org/10.1016/j.jpowsour.2008.11.078.

[5] Santa Rosa DT, Pinto DG, Silva VS, Silva RA, Rangel CM. High performance PEMFC stack with open-cathode at ambient pressure and temperature conditions. Int J Hydrogen Energy 2007;32(17):4350–7. https://doi.org/10.1016/j.ijhydene.2007.05.042.

[6] Al-Zeyoudi H, Sasmito AP, Shamim T. Performance evaluation of an open-cathode PEM fuel cell stack under ambient conditions: case study of United Arab Emirates. Energy Convers Manag 2015;105:798–809. https://doi.org/10.1016/j.enconman.2015.07.082.

[7] Pei H, Shen J, Cai Y, Tu Z, Wan Z, Liu Z, Liu W. Operation characteristics of air-cooled proton exchange membrane fuel cell stacks under ambient pressure. Appl Therm Eng 2014;63(1):227–33. https://doi.org/10.1016/j.applthermaleng.2013.11.012.

[8] Liu W, Wan L, Liu J, Zhao M, Zou Z. Performance improvement of the open-cathode proton exchange membrane fuel cell by optimizing membrane electrode assemblies. Int J Hydrogen Energy 2015;40(22):7159–67. https://doi.org/10.1016/j.ijhydene.2015.04.025.

[9] Atkinson RW, Rodgers JA, Hazard MW, Stroman RO, Gould BD. Influence of cathode gas diffusion media porosity on open-cathode fuel cells. J Electrochem Soc 2018;165(11):F1002–11. https://doi.org/10.1149/2.0041813jes.

[10] Kim B, Lee Y, Woo A, Kim Y. Effects of cathode channel size and operating conditions on the performance of air-blowing PEMFCs. Appl Energy 2013;111:441–8. https://doi.org/10.1016/j.apenergy.2013.04.091.

[11] Sasmito AP, Lum KW, Birgersson E, Mujumdar AS. Computational study of forced air-convection in open-cathode polymer electrolyte fuel cell stacks. J Power Sources 2010;195(17):5550–63. https://doi.org/10.1016/j.jpowsour.2010.02.083.

[12] Sasmito AP, Birgersson E, Lum KW, Mujumdar AS. Fan selection and stack design for open-cathode polymer electrolyte fuel cell stacks. Renew Energy 2012;37(1):325–32. https://doi.org/10.1016/j.renene.2011.06.037.

[13] Sasmito AP, Birgersson E, Mujumdar AS. A novel flow reversal concept for improved thermal management in polymer electrolyte fuel cell stacks. Int J Therm Sci 2012;54:242–52. https://doi.org/10.1016/j.ijthermalsci.2011.11.020.

[14] Shahsavari S, Desouza A, Bahrami M, Kjeang E. Thermal analysis of air-cooled PEM fuel cells. Int J Hydrogen Energy 2012;37(23):18261–71. https://doi.org/10.1016/j.ijhydene.2012.09.075.

[15] Shahsavari S, Bahrami M, Kjeang E. Computational analysis of heat transfer in air-cooled fuel cells. In: ASME 2011 9th international conference on fuel cell science, engineering and technology. Collocated with ASME 2011 5th international conference on energy sustainability, vol. 2011. Fuel Cell; 2011. p. 799–808. https://doi.org/10.1115/FuelCell2011-54794.

[16] Tadbir MA, Shahsavari S, Bahrami M, Kjeang E. Thermal management of an air-cooled PEM fuel cell: cell level simulation. In: ASME 2012 10th international conference on fuel cell science, engineering and technology collocated with the ASME 2012 6th international conference on energy sustainability, vol. 2012. FUELCELL; 2012. p. 453–9. https://doi.org/10.1115/FuelCell2012-91440.

[17] Andisheh-Tadbir M, Desouza A, Bahrami M, Kjeang E. Cell level modeling of the hygrothermal characteristics of open cathode polymer electrolyte membrane fuel cells. Int J Hydrogen Energy 2014;39(27):14993–5004. https://doi.org/10.1016/j.ijhydene.2014.07.049.

[18] Meyer Q, Ronaszegi K, Robinson JB, Noorkami M, Curnick O, Ashton S, Danelyan A, Reisch T, Adcock P, Kraume R, et al. Combined current and temperature mapping in an air-cooled, open-cathode polymer electrolyte fuel cell under steady-state and dynamic conditions. J Power Sources 2015;297:315–22. https://doi.org/10.1016/j.jpowsour.2015.07.069.

[19] Meyer Q, Ronaszegi K, Pei-June G, Curnick O, Ashton S, Reisch T, Adcock P, Shearing PR, Brett DJL. Optimisation of air cooled, open-cathode fuel cells: current of lowest resistance and electro-thermal performance mapping. J Power Sources 2015;291:261–9. https://doi.org/10.1016/j.jpowsour.2015.04.101.

[20] Meyer Q, Himeur A, Ashton S, Curnick O, Clague R, Reisch T, Adcock P, Shearing PR, Brett DJL. System-level electro-thermal optimisation of air-cooled open-cathode polymer electrolyte fuel cells: air blower parasitic load and schemes for dynamic operation. Int J Hydrogen Energy 2015;40(46):16760–6. https://doi.org/10.1016/j.ijhydene.2015.07.040.

[21] Springer TAZTE, Gottesfeld S. Polymer electrolyte fuel cell model. J Electrochem Soc 1990;138(8):2334. https://doi.org/10.1149/1.2085971.

[22] Cao TF, Lin H, Chen L, He YL, Tao WQ. Numerical investigation of the coupled water and thermal management in PEM fuel cell. Appl Energy 2013. https://doi.org/10.1016/j.apenergy.2013.02.031.

[23] Mench MM. Fuel cell engines. 2008.

[24] Meng H. A three-dimensional PEM fuel cell model with consistent treatment of water transport in MEA. J Power Sources 2006;162(1):426–35. https://doi.org/10.1016/j.jpowsour.2006.07.022.

[25] Chaudhary S, Sachan VK, Bhattacharya PK. Two dimensional modelling of water uptake in proton exchange membrane fuel cell. Int J Hydrogen Energy 2014;39(31):17802–18. https://doi.org/10.1016/j.ijhydene.2014.08.128.

[26] O'Hayre. Fuel cell fundamentals - Ryan O'Hayre, vol. 29; 2008. no. 34.

Nomenclature

a: Activity of water vapour
a_v: Active specific surface area (m^{-1})
C_i: Molar concentration of ith species (mol m^{-3})
$C_{i,ref}$: Reference molar concentration of ith species (mol m^{-3})

C_P: Heat capacity at constant pressure (J Kg^{-1} K^{-1})
D: Gas phase diffusivity (m s^{-1})
EW: Membrane equivalent weight (kg mol^{-1})
F: Faraday's constant (C mol^{-1})
j: Current density (A m^{-2})
j_{a_0}: Anodic exchange current density (A m^{-2})
j_{c_0}: Cathodic exchange current density (A m^{-2})
k: Thermal conductivity (W m^{-1} K^{-1})
K: Permeability (m^2)
m_{Pt}: Pt loading (mg cm^{-2})
n_d: Electro-osmotic drag coefficient
P: Pressure (Pa)
R: Gas constant (J mol^{-1} K^{-1})
S: Source
R_{ct}: Charge transfer resistance (Ω)
S_{Pt}: Specific active area of Pt (m^2 g^{-1})
t: Thickness (m)
T: Temperature (K)
u: Velocity vector (m s^{-1})
$\dot{V}$: Volumetric flow rate (m^3 s^{-1})
V_{cell}: Cell voltage (V)
x_i: Mole fraction of ith species

Greek symbols

α: Charge transfer coefficient
γ: Absorption/desorption rate constant (s^{-1})
ε_{CL}: Catalyst layer porosity
ε_l: Effective Pt surface area ratio
ε_m: Porosity of membrane
η: Overpotential (V)
λ: Water content
μ: Kinematic viscosity (m^2 s^{-1})
ρ: Density (kg m^{-3})
σ: Conductivity (S m^{-1})
ϕ: Potential (V)

Acronyms

3D: Three dimensional
atm: atmospheric
avg.: average
ABS: Acrylonitrile butadiene styrene
BC: Boundary condition
BOP: Balance of plant
BPP: Bi-polar plate
CL: Catalyst layer
DC: Direct current
EIS: Electrochemical impedance spectroscopy
Exp.: Experimental
GDL: Gas diffusion layer
HFR: High frequency resistance
MEA: Membrane electrode assembly
MPL: Microporous layer
OCV: Open circuit voltage
ORR: Oxygen reduction reaction
PEMFC: Polymer electrolyte membrane fuel cell
Pt: Platinum
PTFE: Polytetrafluoroethylene
PWM: Pulse width modulation
Re: Reynold's number
ref: Reference
RH: Relative humidity
sat: Saturation
Sim.: Simulated
TC: Thermocouple

Subscripts

a: Anode
c: Cathode
d: Dissolved phase
e: Equilibrium
eff: effective
in: inlet
m: membrane
mass: mass
mol: molar
mom: momentum
s: Solid electrode
v: Volumetric

Appendix B

Strategic Ionomer Design for High Performing Fuel Cells with Open Cathode

Available online at www.sciencedirect.com

ScienceDirect

journal homepage: www.elsevier.com/locate/he

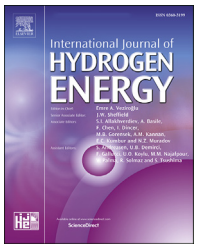

Short Communication

Strategic ionomer design for high performing fuel cells with open cathode

Anand Sagar [a,b], *Sachin Chugh* [b], *Alok Sharma* [b], *Erik Kjeang* [a,*]

[a] *Fuel Cell Research Laboratory (FCReL), Simon Fraser University, #250 13450 102 Avenue, Surrey, British Columbia, V3T 0A3, Canada*

[b] *Alternative Energy-1, R&D Centre, Indian Oil Corporation Limited, Sector-13, Faridabad, Haryana, 121007, India*

HIGHLIGHTS

- The effect of ionomer properties on open-cathode fuel cell performance is simulated.
- Lower ionomer water sorption/desorption rate constant boosts cell performance.
- Membrane drying and slow kinetics are mitigated through strategic ionomer design.

ARTICLE INFO

Article history:
Received 19 July 2021
Received in revised form
1 October 2021
Accepted 17 October 2021
Available online 12 November 2021

Keywords:
Ionomer
Model
Fuel cell
Sorption
Desorption

ABSTRACT

The performance of open-cathode fuel cell systems is limited by deficient humidification and thermal gradients within the individual cells. This work investigates ionomer design strategies to passively control hydration and thereby overcome the inherent performance limitations of such systems. An experimentally validated three-dimensional computational model is used to analyze the effect of a critical ionomer property, namely the water sorption/desorption rate constant at three levels, for cell performance and spatially resolved temperature and water activity. The current density at 0.6 V is found to increase remarkably by 130% by reducing the water sorption/desorption rate constant from 10 s^{-1} to 0.1 s^{-1} under ambient air at 40 °C and 40% relative humidity. This is accomplished through enhanced water retention and membrane hydration at elevated temperature.

Introduction

Open-cathode polymer electrolyte membrane fuel cell (PEMFC) systems that uniquely deploy ambient air as both coolant and oxidant bring significant opportunities for more convenient stacking, reduced part count, and lower balance-of-plant cost compared to conventional liquid cooled systems [1–3]. However, overheating, drying, high membrane resistance, and high charge transfer resistance are key technical challenges for such systems [4–6]. Open-cathode fuel cells rely on ambient airflow and product water for temperature regulation and passive humidification at the cathode whereas dry hydrogen is typically used at the anode.

* *Corresponding author.*
E-mail address: ekjeang@sfu.ca (E. Kjeang).

https://doi.org/10.1016/j.ijhydene.2021.10.131

The open-cathode system therefore does not require humidifiers nor liquid coolant. Within the membrane electrode assembly (MEA), the ionomer in the catalyst layers (CLs) facilitates proton transport between the electrodes and the membrane. The weight ratio of ionomer to carbon support (I/C) in the CL is an important factor for the cell performance. At low relative humidity (RH) conditions, high I/C ratio (≥0.6) was suggested by Liu et al. [7] to counter the low hydration. The solvent composition of the ionomer also affects the cell performance and water-based ionomers were reported to perform better due to lower mass-transport losses and higher electrochemical surface area (ECSA) in the CL [8]. At similar Pt loading and I/C ratio, the catalyst with higher ECSA was found to perform better at high RH conditions, whereas at dry conditions, due to increased protonic resistance even the high ECSA catalyst gave inferior performance [9]. Ionomer equivalent weight (EW) may also influence the cell performance of open-cathode systems. Atkinson et al. [10] suggested use of 1100 EW ionomer over 850 EW ionomer due to lower mass transport resistance and improved cell hydration as determined from electrochemical impedance spectroscopy studies. Additionally, CLs with short side chain ionomer have been reported to have higher ECSA and higher O_2 transport resistance compared to high EW ionomers [11,12]. Garsany et al. [13] reported such ionomers to be superior to long side chain ionomers at all RH conditions due to their different ionomer structure. The specific role of the ionomer in open-cathode systems therefore warrants further investigation.

The present research objective is to understand the effect of ionomer properties on the hygrothermal characteristics and performance of PEMFCs with open cathode. Particular emphasis is placed on the ionomer water sorption/desorption rate constant (γ), which has been reported to affect both water transport and thermal distribution in fuel cell MEAs [14]. Numerical simulations are performed using a previously validated 3D computational model of an open-cathode fuel cell to determine the influence of γ on spatially resolved temperature, RH, water content, and oxygen mole fraction as well as fuel cell performance and voltage loss breakdown. Specific ionomer design strategies for enhanced hygrothermal management and cell performance are explored.

Theoretical

The water transport in the fuel cell is resolved using a two-phase model, featuring vapour phase and dissolved (ionomer) phase. Liquid water is neglected given the predominantly dry environment of open-cathode PEMFCs [15,16]. The concentration of different species including vapour phase water is governed by Eq. (1), where u, c_i, D_{eff}, and S_{mol} are velocity, molar concentration of individual species, effective gas diffusivity, and molar source term, respectively. Water transport in the dissolved phase is governed by Eq. (2), where D_d, C_d, n_d, S_d, j_m, and F designate the back-diffusion coefficient, dissolved phase water concentration, electro-osmotic drag coefficient, source term for dissolved phase, current density in the electrolyte phase, and Faraday's constant, respectively [4].

$$u.\nabla c_i = \nabla.\left(D_{eff}\nabla c_i\right) + S_{mol} \tag{1}$$

$$\nabla.\left(-D_d\nabla C_d\right) + \nabla.\left(\frac{n_d}{F}\, j_m\right) = S_d \tag{2}$$

S_{mol} represents the molar source term at the respective electrodes as given in Eq. (3), signifying the rate of depletion/generation of various reactants and products where j is the average electrode current density. The rate of water transport between the ionomer and vapour phases in the electrodes is determined by Eq. (4).

$$\begin{aligned} &\text{Anode: } S_{mol} = -\frac{j}{2F}\,(H_2);\ -S_{d,a}\,(H_2O) \\ &\text{Cathode: } S_{mol} = -\frac{j}{4F}\,(O_2);\ -S_{d,c} + \frac{j}{2F}(H_2O) \end{aligned} \tag{3}$$

$$S_d = \begin{cases} S_{d,a} = \gamma_a \dfrac{\rho_m}{EW}\,(\lambda_e - \lambda) \\ S_{d,c} = \gamma_c \dfrac{\rho_m}{EW}\,(\lambda_e - \lambda) \end{cases} \tag{4}$$

This work aims to establish the effect of γ_a and γ_c which are model parameters associated with the ionomer properties and are anticipated to be influential for the water transport in the MEA.

Model description

This work utilizes a modified version of our previously reported 3D computational fuel cell model with two phase water transport [4] that includes all governing physics namely the mass, momentum, species, charge, and energy conservation equations with suitable assumptions. The two-phase water transport is governed by Eqs. (1) and (2) and the electrochemical reactions at the respective electrodes are governed by standard Butler–Volmer kinetics [17]. The respective electrode kinetics is dependent on the inlet and local concentrations of hydrogen and oxygen [4]. The model was comprehensively validated [4] by comparing simulated polarization results with experimental data for open-cathode fuel cell operation at various combinations of ambient temperature and RH. These experimental results were obtained after achieving thermal equilibrium at each operating current density while functioning at different ambient conditions [4]. Fig. 1(a) and (b) show two representative polarization results where the simulated open-cathode performance is in good agreement with experimental data measured at ambient temperature of 30 °C and two different RH conditions of 30% and 90%, respectively. The relative error between experimental and simulated results is below 5% for both cases and the experimental reproducibility was also ensured as inferred from the error bars. The results show reduced fuel cell performance at low RH, as expected [4,18,19]. The model was also validated against experimental data for a liquid-cooled cell to ensure robust model performance across a wide range of conditions, as reported elsewhere [4].

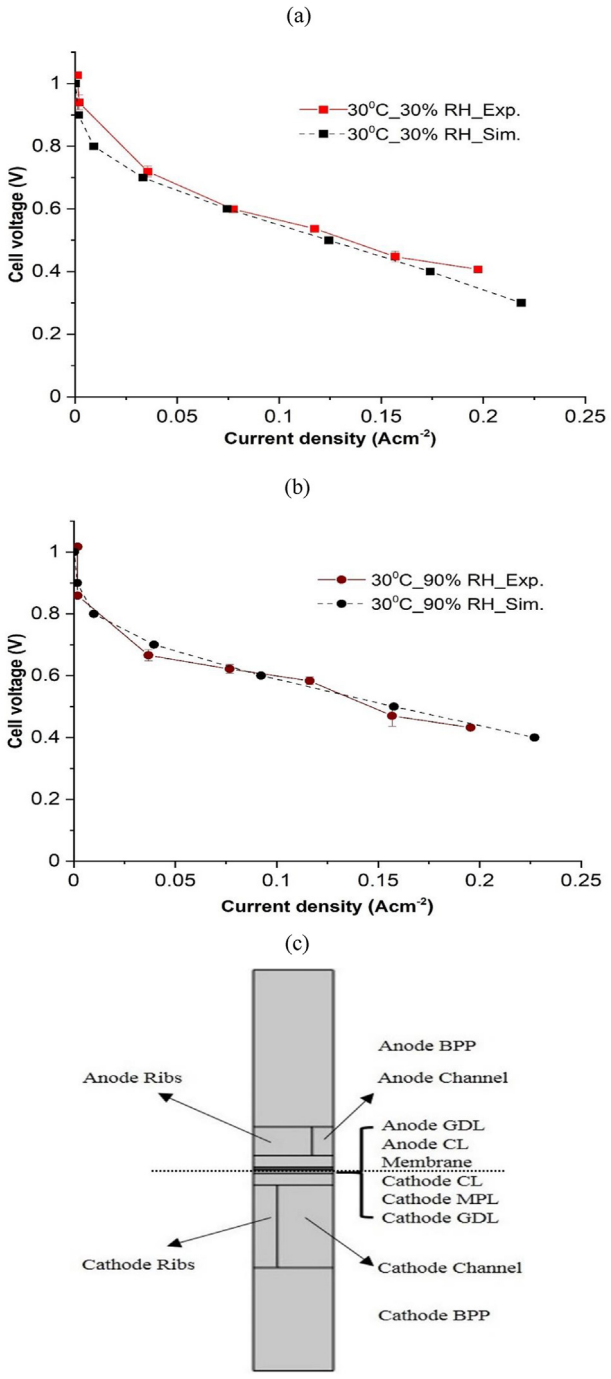

Fig. 1 – Experimental validation of the modelling results for open-cathode PEMFC operation at ambient temperature of 30 °C and RH of (a) 30% and (b) 90%. (c) Front view schematic of the computational domain.

In the present work, the cathode water formation is assumed to take place in the dissolved (ionomer) phase in order to understand the effect of ionomer properties on water transport and membrane hydration which becomes more important for an open-cathode system that operates in a relatively dry state compared to conventional liquid-cooled PEMFCs. The model domain and boundary conditions are consistent with our previous work [4] except for the addition of a microporous layer (MPL) between the cathode CL and gas diffusion layer (GDL) macroporous substrate assumed to be of 90 μm thickness and 40% porosity [20]. This layer is added to facilitate better water transport for open-cathode systems [21]. A front view schematic of the computational model domain is shown in Fig. 1(c), with geometrical details given in Ref. [4]. The model represents a half-channel, half-rib section of a full cell with axial extension from inlet to outlet. The present simulations consider hot and dry ambient air fed through a fan at the cathode inlet at 40 °C and 40% RH. The hydrogen gas supplied to the anode is assumed to have a temperature of 40 °C and RH of 60%, which is representative of dead-end mode operation [22]. The flow rates at anode and cathode inlets are 0.5 nlpm and 2.5 nlpm respectively and operate in a flow-through mode. The MEA consists of a 50 μm Nafion 212 polymeric membrane sandwiched in between anode CL having 0.1 mg cm^{-2} Pt loading and 40%wt ionomer content and cathode CL having 0.4 mg cm^{-2} Pt loading and 40%wt ionomer content. The GDL substrate used on both sides is a 190 μm thick carbon paper with 80% porosity. Additional material properties and initial conditions are reported elsewhere [4]. The steady state model solves the governing physics in segregated steps followed by the last step where all equations are solved in coupled form. The direct based solver is used in COMSOL Multiphysics 5.4 with a relative tolerance of 10^{-3} for each independent variable. The model is solved in potentiostatic mode with fuel cell voltage ranging from 1.0 V to 0.4 V in increments of 0.1 V. A parametric study is performed at three levels of ionomer water sorption/desorption rate, γ to analyze its effect on the hygrothermal characteristics and overall performance of an open-cathode fuel cell. The model was pre-validated in our previous work [4] with γ equal to 10 s^{-1}; hence, the results obtained at $\gamma = 10$ s^{-1} is considered as the reference case for this study and the results obtained at other values of γ are compared with this reference case.

Results and discussion

The simulated effect of the ionomer water sorption/desorption rate constant, γ at high, medium, and low levels (10, 1, and 0.1 s^{-1}, respectively) on the cell performance of an open-cathode PEMFC is shown in Fig. 2(a). The decrease in γ leads to a successive increment in current density at all operating cell voltages. The shift in cell performance is observed primarily in the ohmic and mass transport regions. At 0.6 V, the current density increases by 55% from the reference case of high γ to medium γ, whereas a further increment of 75% is obtained for low γ. These trends are analyzed in the subsequent discussion with the aid of hygrothermal analysis, voltage loss breakdown, and distribution of water content in the PEM. The average cathode CL (CCL) temperature at different cathode channel positions from inlet to outlet is shown as a function of cell voltage in Fig. 2(b–d). For all γ cases, the temperature increases toward the outlet as the electrochemical reaction proceeds. The temperature also increases progressively with decreasing cell voltage for all cases, with a maximum temperature rise of nearly 20 °C reached for low γ. This self-heating effect is attributed to

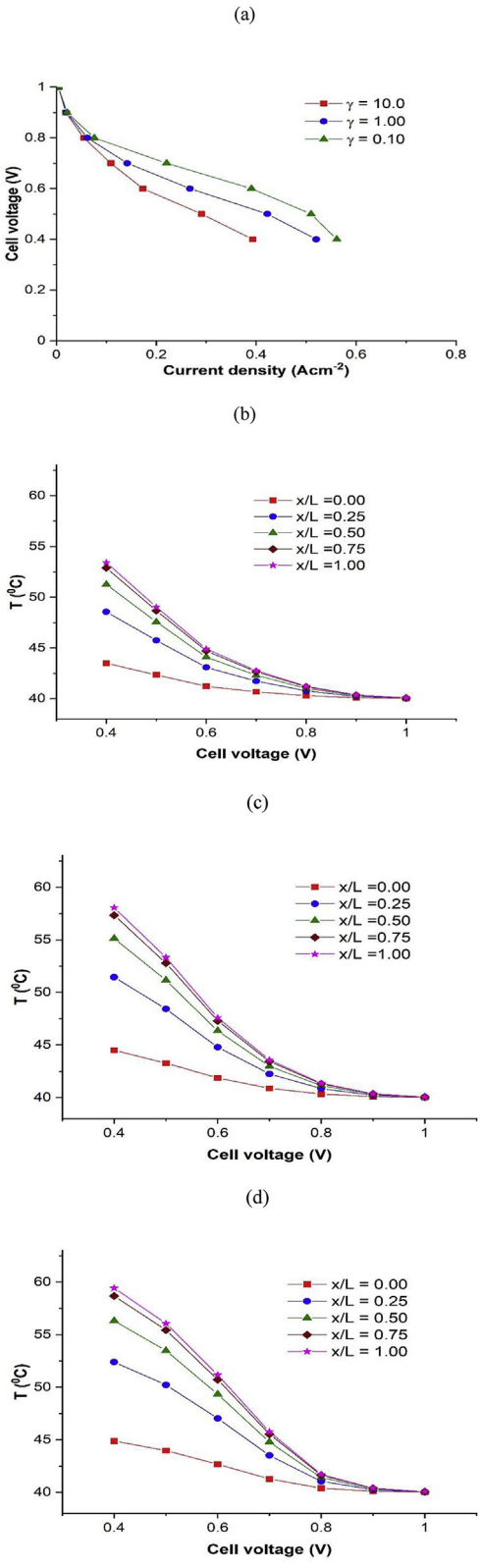

Fig. 2 – (a) Effect of ionomer water sorption/desorption rate constant (γ) on the polarization curve for open-cathode PEMFC systems. Average CCL temperature profiles for (b) $\gamma = 10\ s^{-1}$, (c) $\gamma = 1.0\ s^{-1}$, and (d) $\gamma = 0.1\ s^{-1}$ where x/L is the normalized distance in the cathode flow direction.

internal heat generation from electrochemical and ohmic processes, which can be correlated to the current density data of the cell polarization curves (Fig. 2(a)). However, the temperature rise of the three γ cases only differs by a few degrees, implying that the performance improvement with low γ may be due to other factors.

The distribution of local RH inside the cell, representing the water vapour saturation level, may also influence the overall cell performance. Fig. 3(a–f) shows the average RH profile at the cathode side for 10, 1, and 0.1 s^{-1} at 0.6 V, respectively. Across the length of the cathode flow channel, the overall RH distribution is relatively consistent between the three γ cases, as depicted in Fig. 3 (a), (c), and (e). For all three γ cases, the RH is found to decrease along the channel from inlet to outlet, which is caused by the self-heating effect discussed above. Interestingly, the RH inside the MEA does not follow the same trend, as highlighted by the average RH profile at the CCL given in Fig. 3 (b), (d), and (f) for the three γ cases. For the reference case (high γ) the RH remains at ~30% and is thus lower than in the channel, indicating overall drying of the MEA which is commonly observed for open-cathode cell operation. In contrast, the two cases of medium and low γ exhibit substantially higher RH at the CCL than at the cathode channel, with peak values of 75.4% and 152%, respectively occurring under the rib. This phenomenon of reversed through-plane humidity gradient suggests that the rate of water production at the CCL is able to overcome the relative rate of dryout due to self-heating, which is a key outcome of this work. The water retention at the MEA achieved with low γ represents drastically improved ionomer saturation concurrently with enhanced cell kinetics. The oversaturation at the CCL for low γ also signifies the onset of local liquid water condensation upon ionomer saturation.

The comparative oxygen mole fraction (x_{O_2}) in Fig. 4(a) shows a declining trend with respect to the decreased cell voltage at the CCL. This is attributed to the higher consumption of O_2 with increased current density. The consumption of O_2 is further increased with reduced γ, which supports the increased rate of electrochemical reaction as inferred in the aforementioned temperature and RH trends. The average water content ($\lambda_{avg.}$) in the PEM is displayed in Fig. 4(b) as a function of cell voltage for the three γ cases. The reference case with high γ poses an average $\lambda = 2.4$, which signifies severe membrane dryout while operating at 0.6 V. In contrast, the water content increases nearly two-fold for medium γ and eight-fold for low γ, reaching close to optimal hydration. This favourable increase in λ with decreased γ aids proton conductivity and contributes to boosting the overall cell performance for open-cathode PEMFCs (Fig. 2(a)). The observed increase in λ can be attributed to the higher rate of water production at the cathode combined with the water retaining property of the ionomer achieved with low sorption/desorption rate. The overall rate of water transport from dissolved phase to vapour phase diminishes and more water is available for improved hydration of the PEM and CCL. This trend is also supported by the RH profiles (Fig. 3(a–f)) and the reversal in water activity gradient accomplished with low γ.

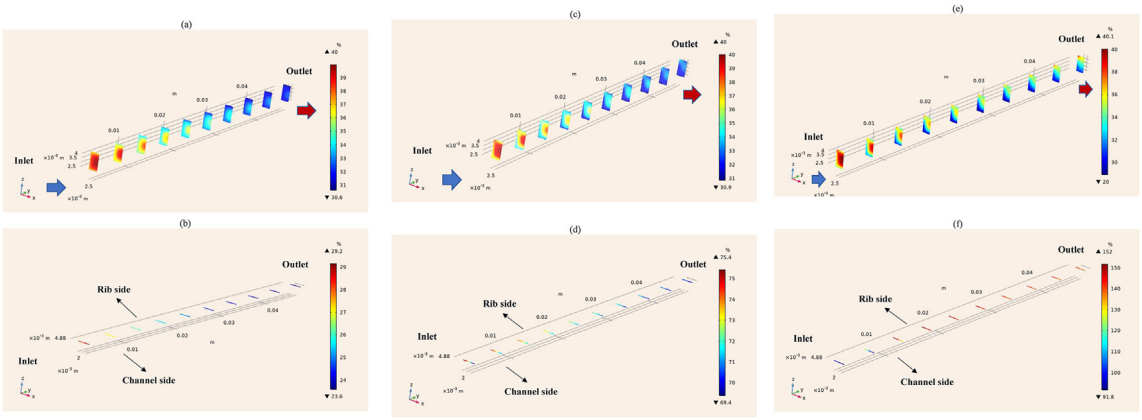

Fig. 3 – Average RH profile at the cathode flow channel and CCL, respectively, for (a, b) $\gamma = 10\ s^{-1}$, (c, d) $\gamma = 1.0\ s^{-1}$, and (e, f) $\gamma = 0.1\ s^{-1}$.

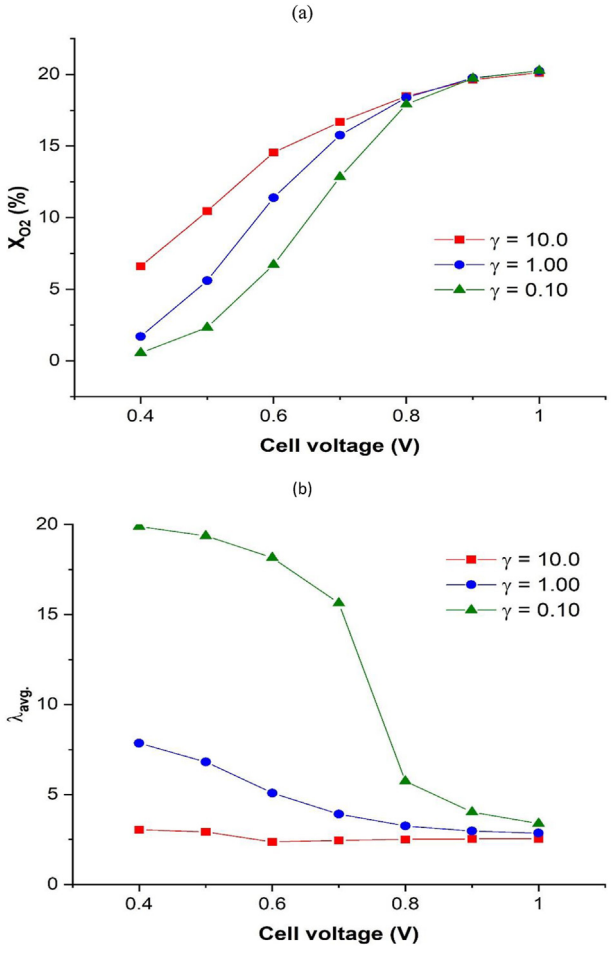

Fig. 4 – (a) Comparative oxygen mole fraction for different γ values at the mid-plane of the CCL. (b) Average water content (λavg.) in the PEM for the three γ cases.

$$\eta_{ohm,i} = \frac{t_i}{\varepsilon_{l,i} * \sigma_{m,i}} * j \quad (5)$$

The net ohmic loss for the cell is calculated by summing the individual ohmic losses of the anode CL, CCL, and PEM from Eq. (5) where $\eta_{ohm,i}$, t_i, $\varepsilon_{l,i}$, and $\sigma_{m,i}$ are the ohmic overpotential, thickness, ionomer volume fraction, and effective electrolyte conductivity, respectively for each component. The ohmic fraction of the total cell overpotential for the three γ cases indicates a declining trend with decreased γ. The ohmic loss fraction decreases by 15% for medium γ and a further 22% for low γ in comparison to the reference case of high γ at 0.6 V. The reduced ohmic loss is attributed to enhanced ionic conductivity in the more hydrated ionomer phase and higher internal cell temperature [23]. This also asserts the λ trends from Fig. 4(b) and justifies the overall improved fuel cell performance for a lower γ with optimum temperature, RH, and λ. Additional results (not included for brevity) show that further reductions in γ below 0.1 s^{-1} do not meaningfully enhance the cell performance. Therefore, $\gamma = 0.1$ s^{-1} is deemed the optimal rate constant for open-cathode fuel cells. Literature reports suggest that such rate constants can be realized with certain existing materials [24,25].

Conclusions

In this work, the ionomer material property namely the water sorption/desorption rate constant was investigated as a design strategy to overcome the low performance of open-cathode fuel cells operating at dry conditions. Three levels of the water sorption/desorption rate constant γ were evaluated using an experimentally validated 3D computational fuel cell model. The open-cathode cell performance was found to be very sensitive to γ, with the highest performance achieved with a low γ of 0.1 s^{-1}, which outperformed the baseline current density at 0.6 V by a remarkable 130%. This dramatic rise in performance was attributed to enhanced water retention in the ionomer phase of the CLs and PEM through inversion of the through-plane humidity gradient in the MEA, indicating that the rate of water production at the CCL was able to overcome the relative rate of dryout due to self-heating. The improved ionomer hydration at elevated temperature led to increased proton conductivity, contributing to a 37% reduction in ohmic voltage

loss fraction, thereby shifting the cell performance to kinetic control. In our future work, we will experimentally verify these results by preparing in-house MEAs with ionomer design suitable for high-performing open-cathode PEMFCs.

Declaration of competing interest

The authors declare that they have no known competing financial interests or personal relationships that could have appeared to influence the work reported in this paper.

Acknowledgments

The authors thank Simon Fraser University and Indian Oil Corporation Limited for joint research funding through the collaborative PhD program in clean energy. E.K. acknowledges additional support provided by Canada Research Chairs.

REFERENCES

[1] Sasmito AP, Birgersson E, Mujumdar AS. Numerical evaluation of various thermal management strategies for polymer electrolyte fuel cell stacks. Int J Hydrogen Energy 2011;36:12991–3007. https://doi.org/10.1016/j.ijhydene.2011.07.028.

[2] Al-Zeyoudi H, Sasmito AP, Shamim T. Performance evaluation of an open-cathode PEM fuel cell stack under ambient conditions: case study of United Arab Emirates. Energy Convers Manag 2015;105:798–809. https://doi.org/10.1016/j.enconman.2015.07.082.

[3] Barreras F, López AM, Lozano A, Barranco JE. Experimental study of the pressure drop in the cathode side of air-forced open-cathode proton exchange membrane fuel cells. Int J Hydrogen Energy 2011;36:7612–20. https://doi.org/10.1016/j.ijhydene.2011.03.149.

[4] Sagar A, Chugh S, Sonkar K, Sharma A, Kjeang E. A computational analysis on the operational behaviour of open-cathode polymer electrolyte membrane fuel cells. Int J Hydrogen Energy 2020;45:34125–38. https://doi.org/10.1016/j.ijhydene.2020.09.133.

[5] Shahsavari S, Desouza A, Bahrami M, Kjeang E. Thermal analysis of air-cooled PEM fuel cells. Int J Hydrogen Energy 2012;37:18261–71. https://doi.org/10.1016/j.ijhydene.2012.09.075.

[6] Andisheh-Tadbir M, Desouza A, Bahrami M, Kjeang E. Cell level modeling of the hygrothermal characteristics of open cathode polymer electrolyte membrane fuel cells. Int J Hydrogen Energy 2014;39:14993–5004. https://doi.org/10.1016/j.ijhydene.2014.07.049.

[7] Liu Y, Murphy MW, Baker DR, Gu W, Ji C, Jorne J, et al. Proton conduction and oxygen reduction kinetics in PEM fuel cell cathodes: effects of ionomer-to-carbon ratio and relative humidity. J Electrochem Soc 2009;156:B970. https://doi.org/10.1149/1.3143965.

[8] Lee MR, Lee HY, Yim SD, Kim CS, Shul YG, Kucernak A, et al. Effects of ionomer carbon ratio and ionomer dispersity on the performance and durability of MEAs. Fuel Cell 2018;18:129–36. https://doi.org/10.1002/fuce.201700178.

[9] Liu Y, Ji C, Gu W, Jorne J, Gasteiger HA. Effects of catalyst carbon support on proton conduction and cathode performance in PEM fuel cells. J Electrochem Soc 2011;158:B614. https://doi.org/10.1149/1.3562945.

[10] Atkinson RW, Garsany Y, Rodgers JA, Hazard MW, Stroman RO, Gould BD. Influence of cathode catalyst layer ionomer on air-cooled, open-cathode fuel cells. ECS Trans 2017;80:461–75. https://doi.org/10.1149/08008.0461ecst.

[11] Poojary S, Islam MN, Shrivastava UN, Roberts EPL, Karan K. Transport and electrochemical interface properties of ionomers in low-Pt loading catalyst layers: effect of ionomer equivalent weight and relative humidity. Molecules 2020;25:3387. https://doi.org/10.3390/molecules25153387.

[12] Ono Y, Ohma A, Shinohara K, Fushinobu K. Influence of equivalent weight of ionomer on local oxygen transport resistance in cathode catalyst layers. J Electrochem Soc 2013;160:F779–87. https://doi.org/10.1149/2.040308jes.

[13] Garsany Y, Sassin MB, Gould BD, Marielle R, Hjelm E, Swider-lyons K. Influence of short-side-chain perfluorosulfonic acid ionomer as binders on the performance of fuel cell cathode catalyst layers. ECS Meet Abstr 2017:33–5. https://doi.org/10.1149/MA2017-02/34/1469. MA2017- 02.

[14] Strahl S, Husar A, Serra M. Development and experimental validation of a dynamic thermal and water distribution model of an open cathode proton exchange membrane fuel cell. J Power Sources 2011;196:4251–63. https://doi.org/10.1016/j.jpowsour.2010.10.074.

[15] Wang Y, Wang C-Y. Simulation of flow and transport phenomena in a polymer electrolyte fuel cell under low-humidity operation. J Power Sources 2005;147:148–61. https://doi.org/10.1016/j.jpowsour.2005.01.047.

[16] Dutta S, Shimpalee S, Van Zee JW. Three-dimensional numerical simulation of straight channel PEM fuel cells. J Appl Electrochem 2000;30:135–46. https://doi.org/10.1023/A:1003964201327.

[17] Cao TF, Lin H, Chen L, He YL, Tao WQ. Numerical investigation of the coupled water and thermal management in PEM fuel cell. Appl Energy 2013;112:1115–25. https://doi.org/10.1016/j.apenergy.2013.02.031.

[18] Atkinson RW, Hazard MW, Rodgers JA, Stroman RO, Gould BD. An open-cathode fuel cell for atmospheric flight. J Electrochem Soc 2017;164:F46–54. https://doi.org/10.1149/2.0261702jes.

[19] Atkinson RW, Hazard MW, Rodgers JA, Stroman RO, Gould BD. Influence of gas diffusion media compression on open-cathode fuel cells. J Electrochem Soc 2019;166:F926–34. https://doi.org/10.1149/2.0021913jes.

[20] Armijo KM, Carey VP. Impact of microchannel boundary conditions and porosity variation on diffusion layer saturation and transport in fuel cells. J Fuel Cell Sci Technol 2012;9:1–8. https://doi.org/10.1115/1.4006476.

[21] Nanadegani FS, Lay EN, Sunden B. Effects of an MPL on water and thermal management in a PEMFC. Int J Energy Res 2019;43:274–96. https://doi.org/10.1002/er.4262.

[22] Brèque F, Ramousse J, Dubé Y, Agbossou K, Adzakpa P. Sensibility study of flooding and drying issues to the operating conditions in PEM Fuel Cells. Int J Energy Environ IJEE 2010;1:1–20.

[23] Ahmadi N, Rezazadeh S, Mirzaee I, Pourmahmoud N. Three-dimensional computational fluid dynamic analysis of the conventional PEM fuel cell and investigation of prominent gas diffusion layers effect. J Mech Sci Technol 2012;26:2247–57. https://doi.org/10.1007/s12206-012-0606-1.

[24] Satterfield MB, Benziger JB. Non-Fickian water vapor sorption dynamics by nafion membranes. J Phys Chem B 2008;112:3693–704. https://doi.org/10.1021/jp7103243.

[25] Wu H, Li X, Berg P. On the modeling of water transport in polymer electrolyte membrane fuel cells. Electrochim Acta 2009;54:6913–27. https://doi.org/10.1016/j.electacta.2009.06.070.

Acronyms

BPP: Bi-polar plate
CL: Catalyst layer
CCL: Cathode catalyst layer
Exp: Experimental
EW: Equivalent weight
ECSA: Electrochemical active surface area
GDL: Gas diffusion layer
I/C: Ionomer to carbon
MEA: Membrane electrode assembly
MPL: Microporous layer
PEM: Polymer electrolyte membrane
PEMFC: Polymer electrolyte membrane fuel cell
RH: Relative humidity
Sim: Simulated

Appendix C

Model driven membrane electrode assembly design for high performing open-cathode polymer electrolyte membrane fuel cells

Abstract

Despite the unique system design and challenging hygrothermal environment of open-cathode fuel cells, their membrane electrode assembly (MEA) designs are generally adopted from conventional, liquid-cooled cells. A pre-validated, three-dimensional computational model is used in the present work to determine the effects of different MEA sub-component designs namely, the polymeric membrane, composition of the cathode catalyst layer, and structure of the cathode microporous layer, on the performance of an open-cathode fuel cell. A comprehensive parametric screening study is performed by simulating a total of 90 cases with various design parameters at two different operating cell voltages of 0.6 and 0.4 V. The filtered parametric design offering the best cell performance for each sub-component is then analyzed through a full factorial design of experiments to come up with the optimal MEA design, shown to achieve twice higher power density than the original reference design. This is accomplished through strategic cathode catalyst layer (thin, high Pt/C ratio, high ionomer loading), cathode microporous layer (thin, high porosity), and membrane (thin) design enabling collective improvements in kinetics, oxygen mass transport, ohmic resistance, self-heating, and water retention in the ionomer phase. The proposed MEA design could facilitate open-cathode fuel cell stacks with higher power and lower cost.

Keywords: fuel cell; open cathode; performance; modelling; optimization; membrane electrode assembly

Introduction

Polymer electrolyte membrane fuel cells (PEMFCs) are a commonly used fuel cell type for various applications including portable, automotive, and stationary applications [1-3]. The membrane electrode assembly (MEA) which generally consists of a polymer electrolyte membrane (PEM) sandwiched in between anode and cathode electrodes (catalyst layers) backed by gas diffusion layers is an integral part of the PEMFC. The design and fabrication of suitable materials, components, and MEAs control the overall cell performance, and continuous research in this field has brought significant improvement in PEMFC efficiency [4].

The low temperature operation of PEMFCs makes them a suitable candidate for automotive applications [5]. The conventional PEMFCs use liquid coolant for extracting the heat produced inside the system which flows through coolant channels present at the bipolar plates [6]. The coolant loop needs to be additionally managed using an external chiller to maintain the constant stack temperature during the operation [7]. This whole setup adds extra cost and space to the total footprint of the PEMFC system. The automotive requirements of producing high power density and low cost fuel cells have led to advancements in fuel cell design in many ways over the years. The use of thinner reinforced membranes as compared to conventional PEMs has been demonstrated to reduce ohmic losses resulting in increased power density [8], [9]. Reduced Pt loading and the use of other non Pt group catalysts have also been explored for cost reduction [10], [11]. Moreover, a microporous layer (MPL) has been introduced in modern PEMFCs to improve water management. These developments have been inculcated to improvise the humidification at the cell level and achieve better thermal management via liquid cooling [12]–[14].

The open-cathode PEMFC design is an alternative to the conventional liquid-cooled design where the cathode side channels are open and the air is used as oxidant as well as coolant [15]. This concept has the distinct advantage of a lower system complexity

since it eliminates the need for liquid cooling and other balance of plant components [16]. The reduction in space, weight and cost are key factors that make the open-cathode design a potential candidate for automotive applications [17]. However, most MEA design and optimization studies have focused on liquid-cooled PEMFCs which generally operate at fully humidified operating conditions with low oxygen stoichiometry. In contrast, open-cathode PEMFCs operate at dry conditions, low operating temperatures, and high airflow rates [18]. The airflow distribution for open-cathode cells has been widely studied, focusing on the fan and air plenum configuration along with geometric optimization of the flow field plates [19]–[24]. Importantly, open-cathode cells experience high temperature gradients and non-uniform conditions along the channel [25], [26]. They are also greatly influenced by the ambient conditions, namely the temperature and relative humidity (RH) of the ambient air. Operation in hot and humid ambient conditions is considered favourable whereas membrane dry out is anticipated in hot and arid environments [27], [28]. Wu *et al.* [29] reported an experimental analysis on the cell performance of open-cathode PEMFCs and found dehydration to be crucial. The use of electro-thermal performance mapping was proposed by Meyer *et al.* [30] to identify the ideal operating point for an open-cathode PEMFC considering the trade-offs between various operating conditions and their impact on cell efficiency and power density. Catalyst coated membrane type MEAs showed higher performance than gas diffusion electrode based MEAs due to better membrane catalyst layer contact. A thicker catalyst layer (CL) with low Pt loading of 20% was found to provide stable cell performance through better water holding capacity at the expense of increased protonic and mass transport resistance [31]. Strategic selection of the ionomer having a lower water sorption/desorption rate constant was similarly proposed to enhance the water retention capability at the CL of open-cathode cells [32]. Generally in PEMFCs, the gas diffusion layer (GDL) controls the water management through its hydrophobicity and porous structure [33]. However, considering the water retention of open-cathode PEMFCs, hydrophilic GDLs were found to perform better than hydrophobic ones [34]. Furthermore, a decreased cathode GDL porosity was found to improve thermal management and cell hydration, thus reducing ohmic resistance [35]. This was attributed to improved thermal and electrical contact at the MEA interfaces. High GDL compression also furnished similar performance improvement. However, high compression and less porous GDLs may have negative side effects of poor oxygen transport to the cathode CL, which is typically critical for open-cathode PEMFCs [36]. The GDL thermal conductivity effect studied in a modelling work for open-cathode cells suggested an insignificant impact

on the thermal profile for such systems [37]. On the contrary, an experimental study recommended the use of a novel GDL having high hydrophobicity to achieve better cell hydration which was also linked to the lower thermal conductivity of such GDLs [38]. This GDL garnered high cell performance for open-cathode systems due to decreased internal cell resistance. A holistic approach to collectively design anode and cathode GDLs was advocated based on *ex-situ* X-ray tomography and *in-operando* neutron imaging data [39].

Most existing literature on MEA design for open-cathode PEMFCs has been empirically developed without robust fundamental knowledge of the underlying characteristics within the unique open-cathode fuel cell environment, often leading to conflicting findings that are likely influenced by the system design and other external factors. The present study, therefore, uses a computational modelling approach wherein the intrinsic coupling between the various governing physics is adequately captured, hence enabling robust predictions of the overall performance of open-cathode fuel cells. The objective of this work is to derive a high-performing MEA design for open-cathode PEMFCs operating at a given ambient condition. A 3D computational model of an open-cathode PEMFC is developed to simulate the fuel cell performance for a wide variety of MEA designs featuring targeted variations in the cathode catalyst layer (CCL), PEM, and cathode microporous layer (CMPL) components using a parametric study approach. The first phase of this work screens the individual parameters involved at the component level to access their impact on the overall cell performance. Next, a full factorial design of experiments (DoE) analysis is performed based on two levels of CCL, PEM, and CMPL design as factors, and the highest performing MEA design set is evaluated by considering both main effects and interaction effects and other critical parameters of the DoE. The best-case design is chosen for each component of the CCL, PEM, and CMPL using a comparative study based on the 3D computational model evaluation.

Methodology

The three-dimensional, two-phase computational open-cathode fuel cell model which was developed and validated in our previous work [26] is used to perform the parametric study concerning the various MEA design parameters as reported in Table C.1.

Table C.1. Parametric design of MEA components for simulation and performance comparison of open-cathode PEMFCs.

Layer	Parameter (unit)	Parametric levels
Cathode catalyst layer (CCL)	t_{CCL} (μm)	15, 30
	ε_{CCL} (%)	20, 40, 60
	wt_{ion} (%)	20, 40, 60
	Pt/C (%)	20, 40, 60
Polymer electrolyte membrane (PEM)	t_{PEM} (μm)	10, 25, 50
Cathode microporous layer (CMPL)	t_{CMPL} (μm)	30, 60, 90
	ε_{CMPL} (%)	40, 60

(a)

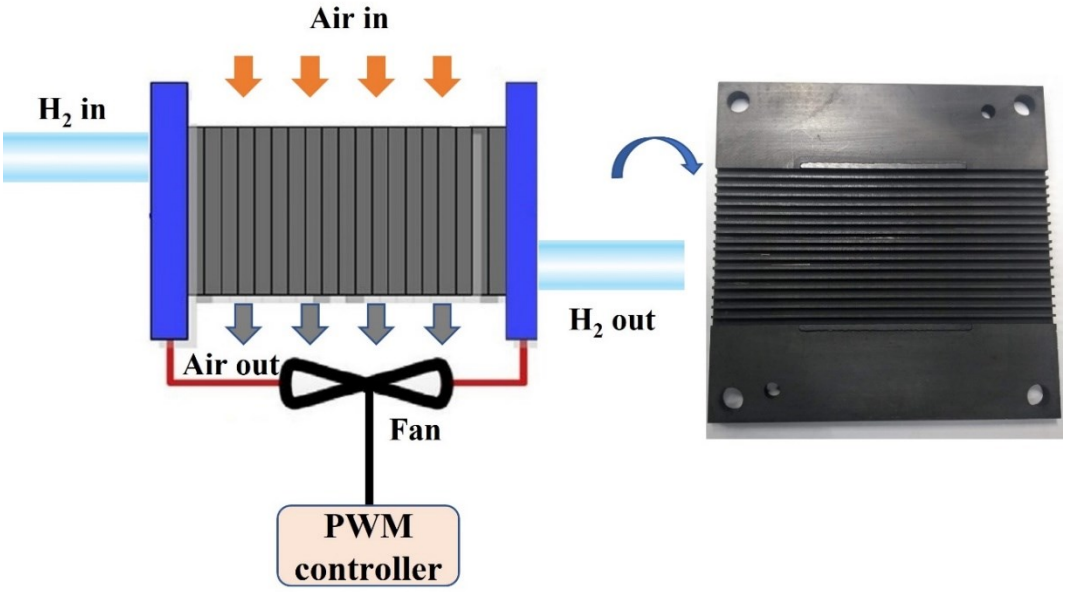

(b)

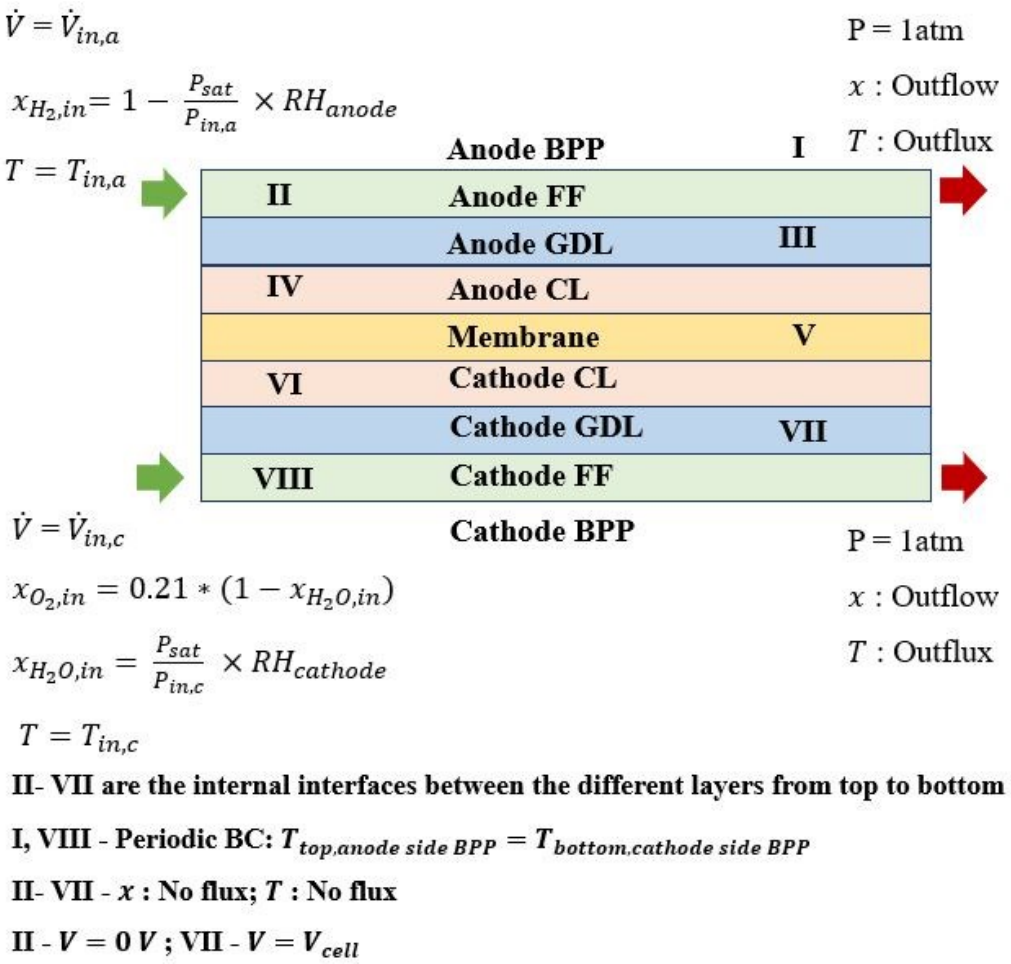

Figure C.1. (a) Schematic of an open-cathode PEM fuel cell stack with the open-cathode flow field (FF) in the bipolar plate (BPP) of a single cell portrayed on the right. (b) Cross-sectional, along-the-channel view of the 3D computational domain with annotated interfaces (indicated by Roman numerals) and boundary conditions (BCs).

Figure C.1 (a) shows the schematic of an open-cathode PEMFC along with a single-cell open-cathode channel. The set of governing equations namely, momentum conservation, mass conservation, species transport, heat transport, charge conservation, and two-phase water transport guiding the transport phenomena in open-cathode cells are solved with intricate couplings as detailed elsewhere [26]. The model geometry and boundary conditions are shown in Figure C.1. Considering the periodic repetition of cells within the full stack and a similar periodicity of straight, parallel open-cathode channels at the cell

level, a single channel/rib domain (Figure C.1) is taken as the focus of this study to evaluate the overall performance characteristics of the open-cathode system. The single channel/rib on each side of the electrode is further halved considering the symmetric condition which is the final computational domain for this study including the MEA sandwiched in between. The approximations are made to minimize the computational cost for model evaluation. The length of the channel is kept at 50 mm and the width of the anode and cathode channels are kept at 0.75 mm and 2.0 mm respectively. The anode ribs and cathode ribs are taken as 1.05 mm and 0.425 mm, whereas the overall height of the anode and cathode channels are kept as 0.7 mm and 2.0 mm. The baseline MEA design consists of a 190 μm carbon paper based GDL and a 15 μm CL on each electrode with a 50 μm membrane sandwiched in between. All domains in the computational model are discretized using tetrahedral and quad meshes with sufficient boundary layers in the flow channels to capture the onset of fully developed flow. The model is created in a COMSOL 5.4 Multiphysics platform using the battery & fuel cells module. Segregated solution steps for individual dependent variables with a final coupled step following a direct solving approach are used to execute the model. All simulation results are evaluated at a fixed operating condition of ambient air at 40ºC and 40% RH considering a typically hot and dry condition. The air flow rate at the cathode inlet is 2.5 nlpm whereas the anode inlet is assigned a hydrogen flow rate of 0.5 nlpm at 40ºC and 60% RH. The partially humidified condition on the anode side is intended to mimic the average anode RH for dead-end mode operation [40]. The model assumptions include incompressible, laminar flow; ideal gases; impermeable membrane; and zero contact resistance at the interfaces. The water produced at the cathode CL is assumed to be in the dissolved phase rather than in vapour form [26], which facilitates more efficient water transport in the system. The ionomer water adsorption/desorption rate constant is an important parameter in this regard, as discovered and extensively discussed in our previous work [32]. This parameter, γ is fixed at 0.1 s^{-1} for this work, which gave the maximum water retention capability while operating open-cathode cells in dry environments. More specifically, a low γ of 0.1 s^{-1} was found to give higher cell performance than the higher γ values of 10 s^{-1} and 1.0 s^{-1} with better membrane and CCL hydration and improved reaction kinetics [32]. Thus, γ = 0.1 s^{-1} is taken as the baseline parameter for the ionomer design in the present work.

The present parametric study focuses on a set of selected MEA design parameters related to the individual sub-components, namely the membrane, CLs, and GDLs, as specified in Table C.1, and utilizes the computational model to simulate their respective effects on the cell performance for open-cathode PEMFCs. The main emphasis is on the CCL, which is typically the MEA sub-component with the greatest influence on the performance of PEMFCs. The CCL is a thin porous layer generally composed of carbon supported electrocatalyst and ionomer mixed in a certain ratio which decides the overall microstructure of the electrode [41]. The net volume of the CCL, V_{CCL} is calculated from (1) where t_{CCL} is the thickness and A_{cell} is the geometrical active area of the CCL. The solid volume of the CCL has agglomerates of Pt, C, and ionomer. The individual weights of Pt, C, and ionomer are represented by W_{Pt}, W_C, and W_{ion} respectively and are calculated from (2), (3), and (4) where m_{Pt} is the Pt loading, Pt/C is the percentage of Pt on carbon, and wt_{ion} is the ionomer loading in weight percentage. W_{Pt+C} is the weight of Pt and C as depicted in (5). The individual volume fractions of Pt, C, and ionomer represented by ε_{Pt}, ε_C, and ε_{ion} respectively and the overall void fraction, ε_{CCL} are calculated from (6), (7), (8), and (9). The CCL design is considered to be based on four parameters namely, CCL thickness (t_{CCL}), CCL porosity (ε_{CCL}), ionomer loading (wt_{ion}) [wt%], and %Pt/C (Pt/C) having 2, 3, 3, and 3 parametric levels respectively, as listed in Table C.1 [42], [43]. The parametric levels for the PEM and CMPL are also mentioned in Table C.1 along with the CCL. The PEM is parametrized at three levels of thickness and the microporous layer introduced between the GDL and the CL on the cathode side has two parameters namely, cathode MPL thickness (t_{CMPL}) and cathode MPL porosity (ε_{CMPL}). The anode CL and GDL properties are kept fixed in this study, considering the relatively rapid hydrogen oxidation reaction at the anode which has limited influence on the overall cell performance [44].

$$V_{CCL} = t_{CCL} * A_{cell} \quad \textbf{(1)}$$

$$W_{Pt} = A_{cell} * m_{Pt} \quad \textbf{(2)}$$

$$W_C = W_{Pt+C} * (1 - Pt/C) \quad \textbf{(3)}$$

$$W_{ion} = \frac{wt_{ion} * W_{Pt+C}}{(1 - wt_{ion})} \quad \textbf{(4)}$$

$$W_{Pt+C} = \frac{W_{Pt}}{Pt/C} \quad \textbf{(5)}$$

$$\varepsilon_{ion} = \frac{(\frac{W_{ion}}{\rho_{ion}})}{V_{CCL}} \quad \textbf{(6)}$$

$$\varepsilon_C = \frac{(\frac{W_C}{\rho_C})}{V_{CCL}} \quad \textbf{(7)}$$

$$\varepsilon_{Pt} = \frac{(\frac{W_{Pt}}{\rho_{Pt}})}{V_{CCL}} \quad \textbf{(8)}$$

$$\varepsilon_{CCL} = 1 - \varepsilon_{ion} - \varepsilon_C - \varepsilon_{Pt} \quad \textbf{(9)}$$

Charge conservation at the CLs is governed by (10) and (11) where $\sigma_{s,eff}$ is the effective electrical conductivity and $\sigma_{m,eff}$ is the effective ionic conductivity. ϕ_s, j_s are the electrode potential and current density, whereas ϕ_m, j_m are the electrolyte potential and current density respectively. $\sigma_{s,eff}$ and $\sigma_{m,eff}$ are calculated from (12) and (13) using a Bruggeman's approximation with ε_{ion} as the electrolyte volume fraction and ε_s as the electrode volume fraction (14). σ_s and σ_m are the bulk electrode electrical conductivity and bulk electrolyte ionic conductivity respectively. The electrochemical reactions are

governed by the Butler-Volmer equations (15) and (16) where j_{a_0}, j_{c_0}, c_i, $c_{i,ref}$, α_i, and η_i are the exchange current density at anode and cathode, molar concentration of ith species, reference molar concentration of ith species, ith electrode transfer coefficient, and ith electrode overpotential respectively. Also, $j_{v,a}$, a_v , S_{Pt}, F, R, and T are volumetric current density, effective Pt surface area per unit volume of CL, the specific active surface area of Pt, Faraday's constant, universal gas constant, and local temperature respectively used in (17) – (18) [45]. The summation of activation overpotential and mass transfer (MT) overpotential represented by η_{act+MT} is obtained from the steady state solution achieved after running a fuel cell simulation at given operating conditions using. The voltage loss breakdown (VLB) used in the present work uses η_{act+MT} to quantify the percentage of individual losses out of the total voltage loss which is a summation of η_{act+MT} and ohmic overpotential (η_{ohm}). η_{ohm} is calculated using (19) where t_i, $\epsilon_{ion,i}$, and $\sigma_{m,i}$ are the thickness, ionomer volume fraction, and effective electrolyte conductivity, respectively for each component and *j* is the operating current density.

$$\nabla . \left(\sigma_{s,eff} \nabla \phi_s\right) = -j_s \quad \textbf{(10)}$$

$$\nabla . \left(\sigma_{m,eff} \nabla \phi_m\right) = -j_m \quad \textbf{(11)}$$

$$\sigma_{s,eff} = \varepsilon_s^{1.5} * \sigma_s \quad \textbf{(12)}$$

$$\sigma_{m,eff} = \varepsilon_{ion}^{1.5} * \sigma_m \quad \textbf{(13)}$$

$$\varepsilon_s = 1 - \varepsilon_{CL} \quad \textbf{(14)}$$

The MPL serves as a buffer layer for water transport between the GDL and the CL [46] and the present work includes the macro-scale modelling of mass transport at the MPL being governed by the convection-diffusion equation (20) where u is the fluid velocity, c_i is the ith species molar concentration, $D_{eff,MPL}$ is the effective diffusion coefficient, and S_{mol} is the molar source term (zero in the MPL). The diffusion in the MPL is governed by mixed (Bosanquet) diffusion represented by (21) where $D_{bulk,eff,MPL}$ is the bulk diffusion coefficient and $D_{Kn,MPL}$ is the Knudsen diffusion coefficient. Since micropores are present in the MPL, the Knudsen diffusion is limiting and dominates the species transport in the MPL. The bulk diffusion follows an empirical approximation (22) to calculate the

$D_{bulk,eff,MPL}$ where $D_{bulk,MPL}$ and ε_{MPL} are the bulk diffusion coefficient and the porosity of the MPL [47-48]. $D_{Kn,MPL}$ is calculated using (23) where $\bar{r}$ is the average pore radius for mass transport and M_k is the molecular mass of the k[th] gas species.

$$j_{s,a} = j_{a_0}\left(\frac{c_{H_2}}{c_{H_{2,ref}}}\right)^{0.5}\left(e^{\frac{\alpha_a F\eta_a}{RT}} - e^{\frac{-\alpha_c F\eta_a}{RT}}\right) \quad \textbf{(15)}$$

$$j_{s,c} = j_{c_0}\left(\frac{c_{O_2}}{c_{O_{2,ref}}}\right)\left(e^{\frac{\alpha_a F\eta_c}{RT}} - e^{\frac{-\alpha_c F\eta_c}{RT}}\right) \quad \textbf{(16)}$$

$$j_{v,a} = j_{s,a} * a_v\,;\; j_{v,c} = j_{s,c} * a_v \quad \textbf{(17)}$$

$$a_v = \frac{m_{Pt}S_{Pt}}{t_{CL}(1-\epsilon_{CL})} \quad \textbf{(18)}$$

$$\eta_{ohm,i} = \frac{t_i}{\epsilon_{ion,i} * \sigma_{m,i}} * j \quad \textbf{(19)}$$

$$u.\nabla c_i = \nabla.\left(D_{eff,MPL}\nabla c_i\right) + S_{mol} \quad \textbf{(20)}$$

$$D_{eff,MPL} = \left({D_{bulk,eff,MPL}}^{-1} + {D_{Kn,MPL}}^{-1}\right)^{-1} \quad \textbf{(21)}$$

$$D_{bulk,eff,MPL} = D_{bulk,MPL} * \left(1-(1-\varepsilon_{MPL})^{0.46}\right) \quad \textbf{(22)}$$

$$D_{Kn,MPL} = \frac{2}{3}\,\bar{r}\,\sqrt{\frac{8RT}{\Pi M_k}} \quad \textbf{(23)}$$

The design set at $t_{CCL} = 15\,\mu m$, $\varepsilon_{CCL} = 20\%$, $wt_{ion} = 20\%$, $Pt/C = 20\%$, $t_{PEM} = 50\,\mu m$, $t_{CMPL} = 90\,\mu m$, and $\varepsilon_{CMPL} = 40\%$ is considered as the baseline MEA design for this work based on previously reported works on open-cathode PEMFCs [26], [32]. Subsequent parametric studies are performed by running the model with parametric values from Table C.1 to understand the sensitivity of the listed parameters on the overall performance of

open-cathode cells. The cell performance is accessed by noting the change in current density with reference to the baseline MEA design while operating at cell voltages of 0.6 V and 0.4 V for each case. For each of the layers mentioned in Table C.1, the parametric values resulting in maximum and minimum current density are obtained and further assessed in terms of temperature, RH, and average O_2 mole fraction distributions at the CCL, which are deterministic to the overall cell performance. The VLB is also performed for the maximum and minimum performing cases to establish the dominant effect responsible for such trends as compared to the baseline MEA design. The maximum and minimum performing designs of the CCL are obtained by evaluating a total of 54 cases from the different permutations of the CCL parameters while the corresponding PEM and CMPL parameters are fixed at the baseline values. The maximum and minimum performing designs for PEM and CMPL are similarly determined by evaluating 3 and 6 different parameter combinations, respectively. Once the maximum and minimum performing cases are obtained based on the parametric evaluation for the PEM, CCL, and CMPL components, a full factorial design of experiments (DoE) study is performed to achieve the highest performing design set at the MEA level. The three factors for the DoE are taken as PEM, CCL, and CMPL, each with two levels namely high (H) and low (L) taken as the maximum and minimum performing design sets from the parametric evaluation performed earlier. Thus, a total of eight MEA design cases are evaluated computationally to achieve the final design set at the MEA level having the highest performance. Both the main effects and interaction effects of the three components are calculated and analyzed by performing this DoE since coupled effects between MEA components are anticipated.

Results and Discussion

Model Validation

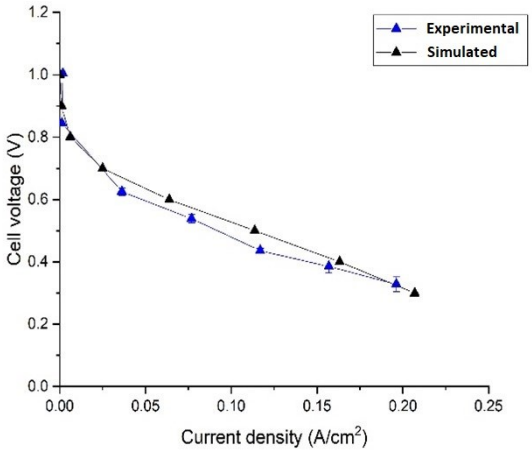

Figure C.2. Model validation on an open-cathode single cell operating at ambient condition of 50^{0}C and 30% RH.

The two-phase computational model discussed in the previous section and used in this work was previously validated with experimental data for various cases of open-cathode PEMFC operation. Figure C.2 shows the comparative polarization curve for one of these cases where the experimental data obtained for running the open-cathode single cell at an ambient condition of 50^{0}C and 30% RH are presented together with the corresponding simulation results for the same cell design and operating conditions. The polarization curves show a reasonably good agreement between experimental and simulated results with experimental measurement uncertainty below 5% over different current densities. This shows that the model is capable of capturing the unique performance characteristics of open-cathode PEMFCs, which generally feature greater variability than liquid-cooled PEMFCs due to higher internal gradients whereas the lower current densities obtained are due to the cell being operated in dry conditions which pose higher ohmic losses. This validated model is used in subsequent sections to perform parametric design at the component level of the MEA.

Parametric Results

PEM parametric design

With respect to the baseline MEA design when the CCL and CMPL parameters are kept constant and only the PEM design is changed parametrically, as per Table C.1, the current density (CD) is increased by 7.1% at 0.6 V and by 1.5% at 0.4 V respectively when the PEM thickness is changed from 50 μm to 10 μm. These results are illustrated in Figure C.3. The minor increments in CD can be attributed to the decreased ohmic resistance offered by the thinner membrane. However, the performance boost is limited by the other MEA design constraints of the CCL and CMPL which remain at baseline levels. The interaction effect of the PEM thickness with other component changes is explained in the subsequent section to understand the overall open-cathode cell performance dependence on PEM thickness.

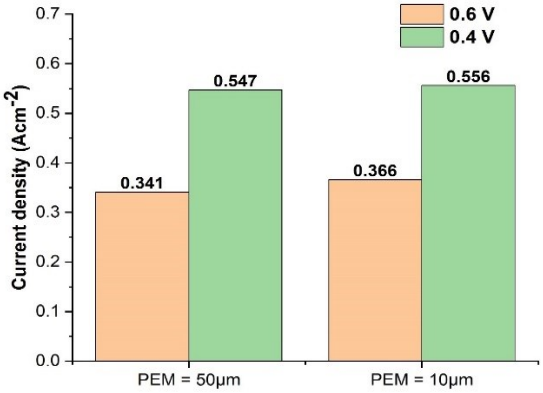

Figure C.3. Effect of PEM thickness on current densities at 0.6 V and 0.4 V.

Cathode CL parametric design

With respect to the baseline MEA design set at $t_{CCL} = 15\ \mu m$, $\varepsilon_{CCL} = 20\%$, $wt_{ion} = 20\%$, $Pt/C = 20\%$, $t_{PEM} = 50\ \mu m$, $t_{CMPL} = 90\ \mu m$, and $\varepsilon_{CMPL} = 40\%$; the individual effects of the parameters listed for the CCL in Table C.1 namely $t_{CCL}, \varepsilon_{CCL}$, wt_{ion}, and Pt/C are evaluated to ascribe the interdependence on the overall cell performance for open-

cathode cells. When t_{CCL} is increased from $15\ \mu m$ to $30\ \mu m$, the m_{Pt} doubles to 0.88 mg cm^{-2} as compared to 0.44 mg cm^{-2}, and the CD increases by 9.4% and 1.2% at 0.6 V and 0.4 V respectively as compared to the baseline. The main reason for the improved performance is the higher Pt loading resulting from the greater CCL thickness, noting that m_{Pt} is proportional to t_{CCL} while keeping other factors constant. Thus, the overall increase in CD comes at the expense of a very high Pt loading spread volumetrically. Similarly, when Pt/C is increased from 20% to 60% while keeping the other electrode parameters at the baseline reference, the overall Pt loading increases from 0.44 mg cm^{-2} to 2.0 mg cm^{-2} which is undesirable for preparation considering the high cost involved with such CCL design. Equivalent trends are also obtained for ε_{CCL} and wt_{ion} when parameterized individually as per Table C.1. The CCL design is thus found interlinked in the different variables associated with it. Thus, the parametric design analysis of the CCL is performed by evaluating a total of 54 cases obtained from the feasible permutations of the selected design variables namely $t_{CCL}, \varepsilon_{CCL}$, wt_{ion}, and Pt/C as specified in Table C.1. The individual cases which result in very high Pt loading (above 1 mg $_{Pt}$ cm^{-2}) are discarded considering the cost implication. Out of the remaining subset of 40 cases, the CCL design with $t_{CCL} = 15\ \mu m$, $\varepsilon_{CCL} = 40\%$, $wt_{ion} = 40\%$, and $Pt/C = 60\%$ gives the highest CD of 0.45 A cm^{-2} at 0.6 V as compared to 0.34 A cm^{-2} for the baseline case. Figure C.4 (a) shows the comparative polarization curve for the base case and the CCL design case with the highest cell performance. There is an overall shift from the base case at all operating current densities with a nearly 30% increment in current density observed at 0.6 V. The gap narrows down at lower cell voltages and is merely 4.2% at 0.4 V. The reasons for the increased CD for this modified CCL design are established by reviewing the trends (Figure C.4 (b)-(d)) of T, RH, and η_{act+MT}. The average temperature for the best CCL design case increases by 2-3°C at the cathode outlet region as compared to the base case. This can be attributed to increased heat generation due to the higher current density at 0.6 V, which is influenced by the higher levels of wt_{ion} and Pt/C for the best CCL design case as compared to the baseline. The increment in wt_{ion} from 20% to 40% provides improved proton conductivity whereas the Pt/C increment from 20% to 60% aids the oxygen reduction reaction (ORR) which in turn leads to higher CD and thereby increased temperature levels. The increment in average temperature from inlet to outlet shows a similar trend to that reported for open-cathode cells in the literature [26] and is attributed to self-heating at the cell level. The ΔT from inlet to outlet is roughly 10°C for the best CCL design as compared to 7.5°C for the base case. From Figure C.4 (c) the RH at the CCL

increases by up to 40% at the cathode inlet region for the best CCL design as compared to the base case. The difference in RH decreases somewhat towards the outlet and remains 10-15% higher. The elevated RH can be attributed to the increment in wt_{ion} and Pt/C for the best CCL design as compared to the base case which facilitates higher CD resulting in a higher amount of water produced at the CCL. The relative drop in ΔRH towards the outlet can be explained by the increased self-heating observed in the temperature plots (Figure C.4 (b)). Overall, however, it is noteworthy that both cases exhibit adequate hydration at the CCL, so membrane dry-out is unlikely. The O_2 mole fraction at the CCL shows a reverse trend versus the T and RH profiles, as seen in Figure C.4 (d), as it decreases for the best CCL design as compared to the base case. The decrease in the O_2 mole fraction is related to the increased consumption of O_2 due to the increased CD obtained for the best CCL design. The two cases show a similar ohmic loss (η_{ohm}) fraction of 16% out of the total polarization losses, as calculated using (19). With increased CD, η_{ohm} increases for a fixed design case. For the best CCL design, however, this is compensated by increased ionomer fraction in the CCL and increased proton conductivity facilitated by improved hydration.

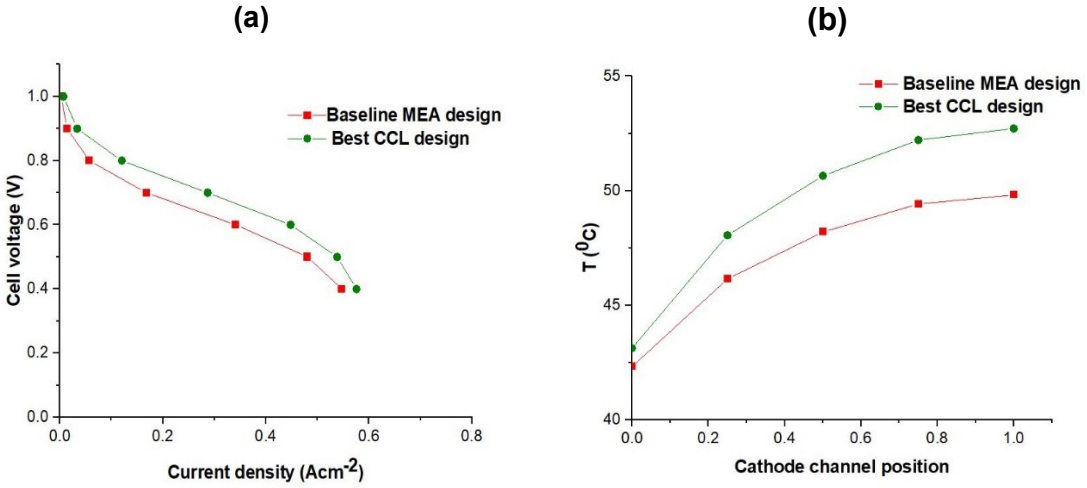

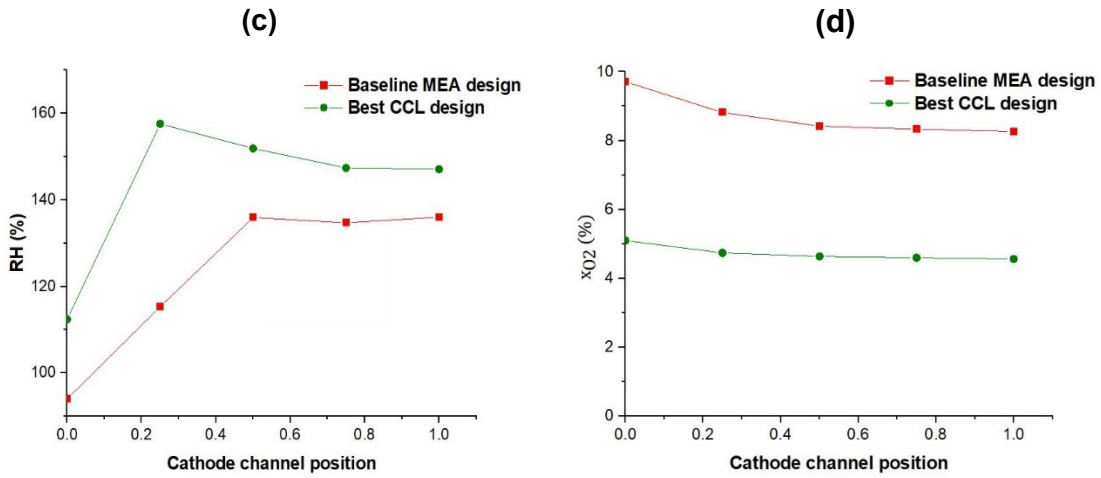

Figure C.4. Comparative (a) polarization curves and average (b) temperature, (c) RH, and (d) O_2 mole fraction profiles at the CCL across the cell length at 0.6 V for the baseline MEA design case and best CCL design case.

Cathode MPL parametric design

The effect of CMPL design on open-cathode fuel cell performance is analyzed by changing the CMPL thickness and porosity as compared to the base case. The CMPL thickness is varied at three levels of 30, 60, and 90 μm whereas the CMPL porosity is kept at two different levels of 40% and 60%. A total of five different cases are evaluated and the results in terms of CD are compared. When the CMPL thickness is reduced while keeping the porosity constant, the cell performance is found to increase. Similarly, increased porosity at a fixed CMPL thickness also leads to performance improvement. Hence, the thinnest CMPL (30 μm) with the highest porosity (60%) is found to maximize the open-cathode cell performance at both cell voltages (0.6 and 0.4 V) and is therefore considered the best CMPL design. Figure C.5 (a) shows the comparative polarization results for the base case and the best CMPL design case. The increment in cell performance is found to be achieved primarily in the mass transport region when operated at lower cell voltages. Figure C.5 (b) shows that the O_2 mole fraction at the CCL at 0.4 V is greatly improved for the best CMPL design as compared to the base case. For the base case, the O_2 availability is minimal and shows signs of O_2 scarcity at high current density operation whereas, for the obtained best CMPL design, the thin MPL with high porosity provides substantially lower oxygen diffusion resistance between the channel and the CCL. Thus, the best CMPL

design is able to sustain good oxygen availability at the CCL despite the higher CD and rate of oxygen conversion. Moreover, the average CCL temperature in the outlet region is found to increase by nearly 15°C for the best CMPL design as compared to the base case, as depicted in Figure C.5 (c) [49]. This effect can be attributed to the increased reactant availability at the CCL which intensifies the rate of ORR and thus generates more heat. Synergistically, the increased CCL temperature for the best CMPL design also aids the ORR by improving the cell kinetics which results in increased CD as depicted in Figure C.5 (a). Interestingly, the water content (λ) at the PEM for the best CMPL design remains lower throughout the cell as compared to the base case, as evident from Figure C.5 (d). This is a consequence of the increased ORR and higher heat generation which implicates overall drying of the CCL and the PEM and is common to an open-cathode system. This critical effect is further investigated in Figure C.6, featuring the full cathode side RH profiles in the two comparative cases. The RH is maximum at the CCL as compared to other parts of the cathode side and remains oversaturated for the base case, whereas for the best CMPL design the RH at the CCL drops from roughly 80% at the inlet to 40% at the outlet. Also, the RH drops further to 20% at the cathode flow channel outlet. This drying effect can be attributed to the heat generation due to high ORR rate and CD of the best CMPL design unlike the base case and complements the λ trend at the PEM from Figure C.5 (d). Also, it can be concluded that even though drying is evident at such operating cases for open-cathode systems, strategic CMPL design can achieve considerably improved cell performance.

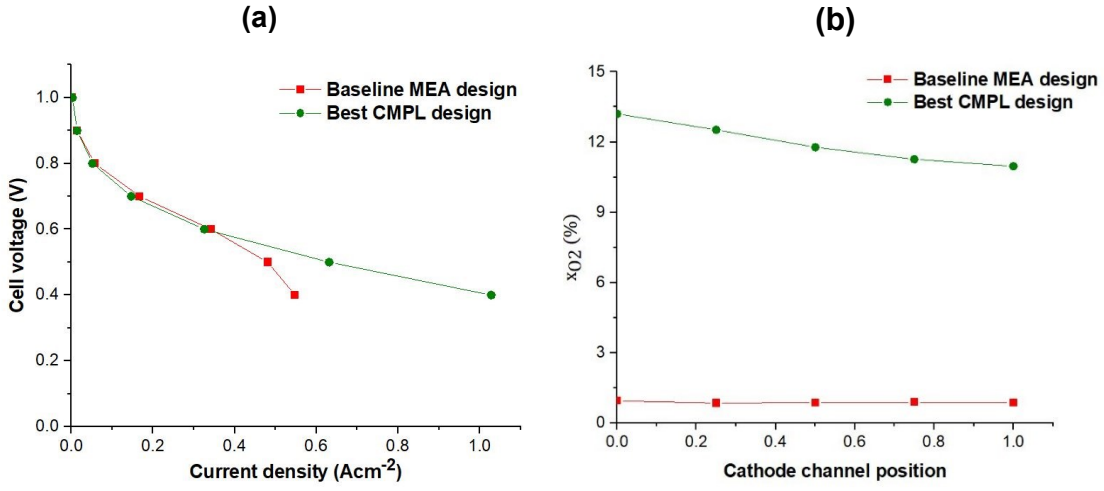

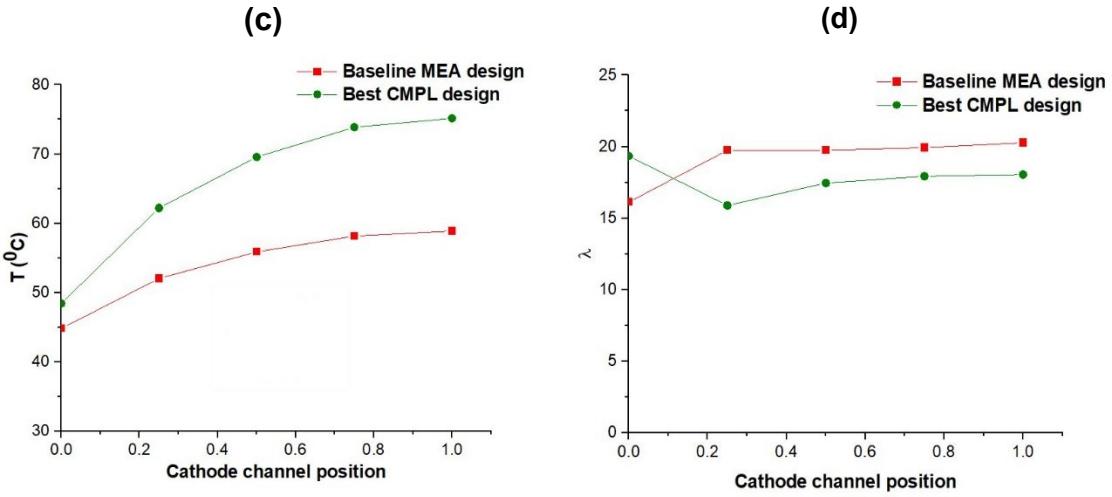

Figure C.5. Comparative (a) polarization curves and average (b) O_2 mole fraction profiles, (c) temperature at the CCL, and (d) water content (λ) of the PEM across the cell length at 0.4 V for the baseline MEA design case and best CMPL design case.

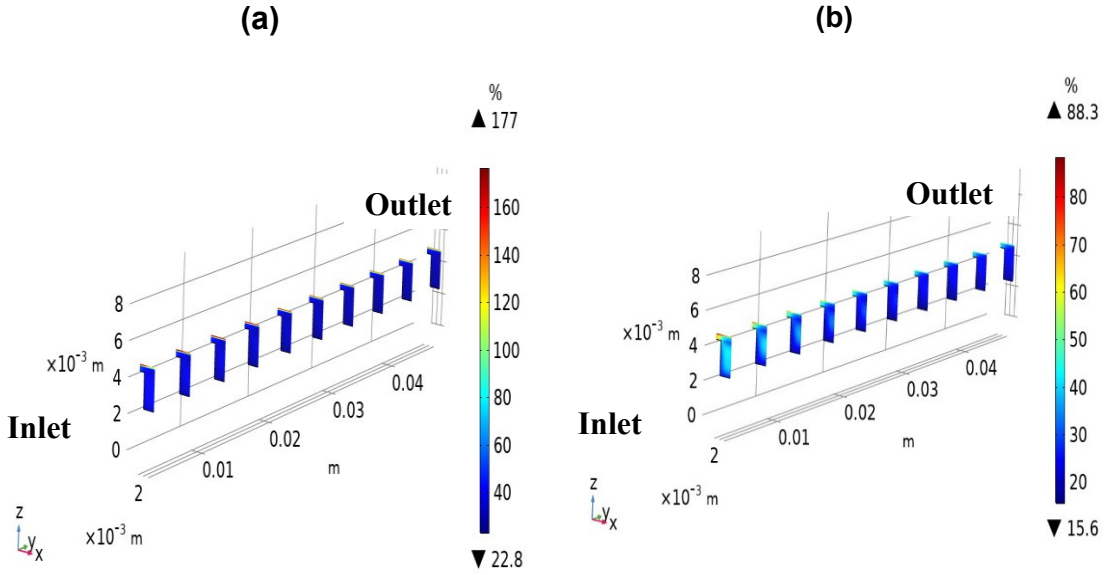

Figure C.6. Simulated RH profiles of the cathode side (flow channel, GDL, MPL, and CCL) for the (a) reference case and (b) optimum CMPL design at 0.4 V.

DoE Analysis

Table C.2. List of DoE design factors and levels.

Design Factor	Level (High)	Level (Low)
PEM Design	$t_{PEM} = 10\ \mu m$	$t_{PEM} = 50\ \mu m$
CCL Design	$t_{CCL} = 15\ \mu m$ $\varepsilon_{CCL} = 40\%$ $wt_{ion} = 40\%$ $per_{Pt/C} = 60\%$	$t_{CCL} = 15\ \mu m$ $\varepsilon_{CCL} = 20\%$ $wt_{ion} = 20\%$ $per_{Pt/C} = 20\%$
CMPL Design	$t_{CMPL} = 30\ \mu m$ $\varepsilon_{CMPL} = 60\%$	$t_{CMPL} = 90\ \mu m$ $\varepsilon_{CMPL} = 40\%$

Table C.3. Comparative current densities at 0.6 V and 0.4 V for various DoE cases.

Sl.no.	PEM design level	CCL design level	CMPL design level	I (Acm^{-2}) at 0.6 V	% (↑↓) in CD at 0.6 V w.r.t base case	I (Acm^{-2}) at 0.4 V	% (↑↓) in CD at 0.4 V w.r.t base case
1	L	L	L	0.342	0.00	0.548	0.00
2	H	L	L	0.366	7.11	0.556	1.48
3	L	H	L	0.447	30.9	0.570	4.20
4	H	H	L	0.468	36.9	0.576	5.20
5	L	L	H	0.325	-4.68	1.028	87.7
6	H	L	H	0.418	22.5	1.170	114
7	L	H	H	0.602	76.3	1.279	133
8	H	H	H	0.750	119	1.266	131

The DoE analysis is performed using statistical software (Minitab 17) for three MEA design variables termed as factors namely, PEM, CCL, and CMPL with two levels at high (H) and low (L) as per Table C.2. The maximum and minimum performing design cases obtained from the parametric evaluation of the three individual layers namely, the PEM, CCL, and CMPL are taken as the two distinct levels termed H and L, respectively. A total of eight simulations are run at these design levels and the resultant CD at 0.6 and 0.4 V is used as the response to evaluate the main and interaction effects of these factors using a full factorial design. Table C.3 lists the individual responses in terms of CD for these eight different cases of the DoE. The change in CD with respect to the design case with all three factors at their low level is also tabulated to understand the significance of the design changes. For the operation of open-cathode PEMFC at 0.6 V, case-8 having HHH design space shows the highest performance with an increment of 119% in CD compared to the base case, *i.e.*, case-1 (LLL). Whereas, case-7 and case-8 are found to have the highest performance among all the eight DoE cases with LHH and HHH design for PEM, CCL, and CMPL respectively for operation at 0.4 V. The detailed understanding of the DoE results is evaluated based on ANOVA analysis performed with a 95% significance level at 0.6 and 0.4 V for which the details are listed in Table C.4 and Table C.5 respectively. The three-way interaction effect is analyzed as an initial step of DoE at each cell voltage; however, this high-order interaction is found minimal for both cell voltages and hence eliminated for the final analysis of the data. At medium current density (0.6 V), the effect of CCL design is maximum followed by CMPL and PEM in terms of main effects, all three being statistically significant. Also, the CCL and CMPL interaction effect is significant as compared to less significant PEM and CMPL interaction. The PEM and CCL interaction effect is not significant and hence neglected from the final DoE analysis at 0.6 V shown in Table C.4 and Figure C.7. The interaction plot (Figure C.7 (a)) reveals the nature of these interactions: concurrently high levels (HH) of PEM and CCL and more importantly, concurrently high levels (HH) of CCL and CMPL have a particularly beneficial impact on the CD of the open-cathode cell operated at 0.6 V. This further reveals significant coupling between the design of the individual MEA layers that should be considered when designing open-cathode MEAs and fuel cells. The DoE results at high current density (0.4 V) show the CMPL main effect to be heavily dominant as compared to those of the CCL and PEM, with the main effect of PEM being negligible. The interaction of CCL and CMPL is dominant among the two-way interactions, which is consistent with the outcome at 0.6 V, whereas the other two-way interactions are insignificant and hence neglected from the

final DoE analysis at 0.4 V (Table C.5 and Figure C.7 (c-d)). Interestingly, this outcome suggests that the open-cathode cell performance at 0.4 V is statistically independent of the PEM thickness (10-50 μm) within the present scope of the DoE. This outcome is however influenced by the very strong impact of the CMPL design. The ANOVA analysis thus justifies the increase in CD with an enhanced level design of CCL and CMPL at both 0.6 V and 0.4 V. This is in adherence to the individual parametric study where CCL and CMPL were found influencing, but further shows their important coupled effect. At 0.4 V, the CMPL design dominance can be attributed to the well-managed oxygen mass transport achieved with a thin, highly porous CMPL as compared to an inferior CMPL design. Also, most notably at 0.6 V, the combined CCL and CMPL design elevation (thin, high-porosity CMPL and CCL; high ionomer loading; and high Pt/C ratio) contribute reduced ohmic resistance paired with favorable reaction kinetics, which leads to an overall performance enhancement for open-cathode PEMFCs. At this specific condition, the cell performance can be additionally enhanced by PEM design (*i.e.*, thin membrane) via a further reduction in ohmic loss.

Table C.4. ANOVA table for the DoE at 0.6 V.

Source	DF	Adj SS	Adj MS	F-Value	P-Value
Model	5	0.146307	0.029261	77.16	0.013
Linear	3	0.121305	0.040435	106.62	0.009
PEM	1	0.010224	0.010224	26.96	0.035
CCL	1	0.083232	0.083232	219.46	0.005
CMPL	1	0.027848	0.027848	73.43	0.013
2-Way Interactions	2	0.025003	0.012501	32.96	0.029
PEM*CMPL	1	0.004802	0.004802	12.66	0.071
CCL*CMPL	1	0.020200	0.020200	53.26	0.018
Error	2	0.000759	0.000379		
Total	7	0.147066			

Table C.5. ANOVA table for the DoE at 0.4 V.

Source	DF	Adj SS	Adj MS	F-Value	P-Value
Model	3	0.80742	0.269141	105.38	0.000
Linear	2	0.79580	0.397898	155.79	0.000
CCL	1	0.01892	0.018915	7.41	0.053
CMPL	1	0.77688	0.776881	304.17	0.000

2-Way Interactions	1	0.01163	0.011628	4.55	0.100
CCL*CMPL	1	0.01163	0.011628	4.55	0.100
Error	4	0.01022	0.002554		
Total	7	0.81764			

(a)

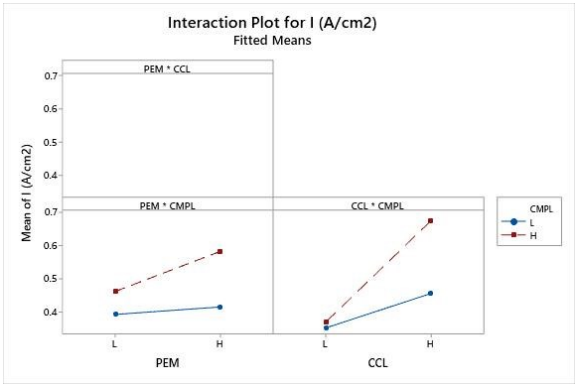

(b)

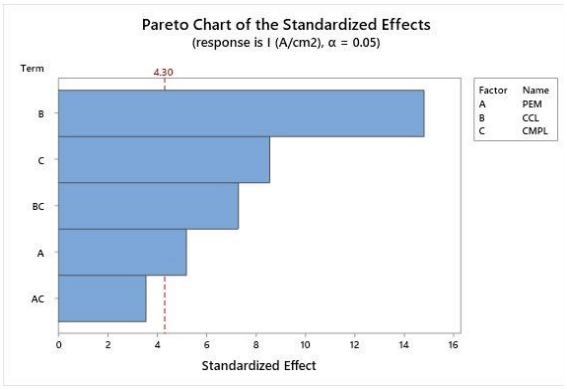

(c)

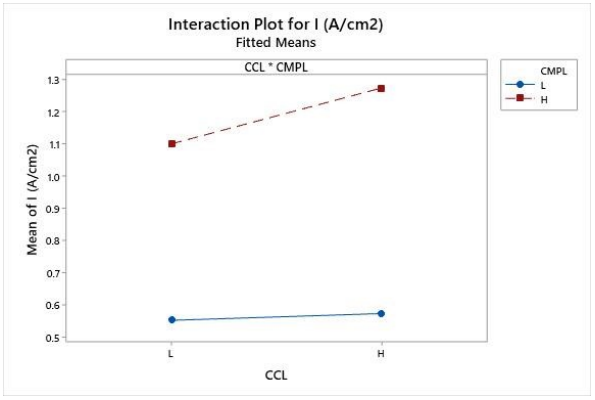

(d)

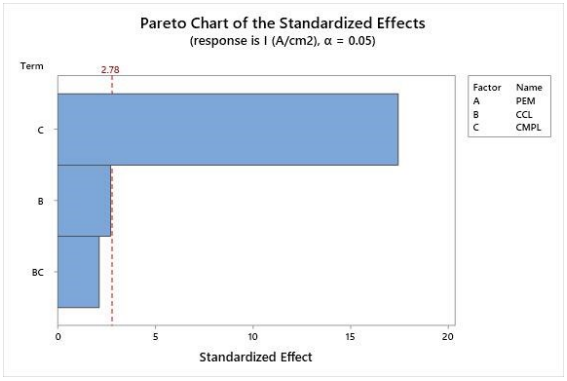

Figure C.7. (a) DoE interaction plot at 0.6 V; (b) Pareto chart at 0.6 V; (c) DoE interaction plot at 0.4 V; and (d) Pareto chart at 0.4 V.

γ interaction with optimized MEA design

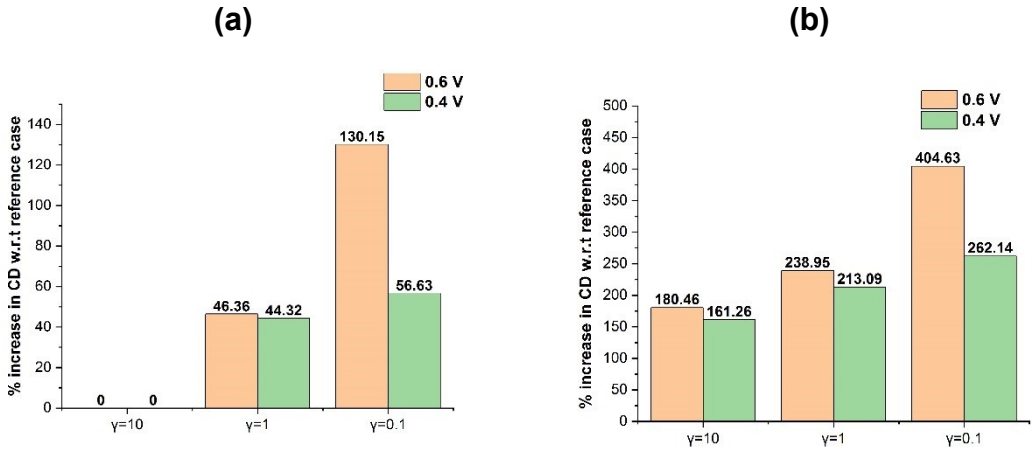

Figure C.8. (a) Relative increase in CD as an effect of γ for the (a) reference case and (b) optimum MEA design.

The sorption/desorption rate constant of the ionomer (γ) is an important factor influencing the CCL design as presented in our previous work [32]. The effect of γ at three levels of 10, 1, and 0.1 s^{-1} is simulated for the reference case and the best optimized case from prior discussions to analyze the interaction of γ with the optimum MEA design space for open-cathode cells. From Figure C.8 the change in γ is found to bring a CD improvement of 130% at 0.6 V and 57% at 0.4 V for the reference design space when varied from 10 to 0.1. For the same change in γ for the optimized MEA design space, the increment is 224% at 0.6 V and 100% at 0.4 V respectively. The effect of γ on the cell performance of open-cathode PEMFC by providing optimum water retention in the ionomer phase at the CCL is evident in all cases. Interestingly, this trend reveals the coupling between favourable γ improvement and favourable design space for the MEA. Decreased γ with improved MEA design is found to boost the performance by complementing each other. This can be attributed to the improved water retention in the dissolved phase contributed by lower γ and better water and O_2 transport facilitated by improved CMPL and CCL design. The combination presented as an optimized MEA design with γ = 0.1 s^{-1} is found to optimize the thermal and water management for open-cathode PEMFCs and elevate the cell performance near to a conventional liquid-cooled design.

Conclusions

In the present work, a model driven approach was used to investigate the impact of selected MEA design parameters on the cell performance of an open-cathode PEM fuel cell system operated at a typical dry ambient condition of 40°C and 40% RH. A pre-validated 3D computational fuel cell model developed specifically for open-cathode PEMFCs was utilized for this purpose. In the first phase, a parametric screening study was performed on a comprehensive set of design parameters for the PEM, CCL, and CMPL sub-components, whereas each component change was treated individually while the other components are kept at the baseline level. The PEM thickness showed the least sensitivity towards the CD as the MEA performance metric of interest. For the CCL, out of 40 design cases evaluated with Pt loading below 1 mg cm^{-2}, the most influential factors were high ionomer loading to improve proton conductance and high Pt/C ratio to enhance the oxygen reduction kinetics which collectively led to higher CD and thereby increased cell temperature. Overall, the thin CCL design with moderate porosity and ionomer loading and high Pt/C ratio gave the highest CD of 0.45 A cm^{-2} at 0.6 V as compared to 0.34 A cm^{-2} for the baseline design. Similarly, a thin CMPL design with high porosity was found to enhance the CD by means of lower oxygen diffusion resistance, with the strongest effect observed at 0.4 V. This design was able to sustain good oxygen availability at the CCL despite the higher CD and rate of oxygen conversion. The kinetics were also promoted by the higher internal cell temperature reached due to the increased heat generation within the cell at elevated CD. However, drying of the membrane was also evident as a consequence of this, which restricted the overall performance.

In the second phase of this work, a statistical analysis using full factorial DoE was performed for the MEA design using three factors namely the PEM, CCL, and CMPL with their high and low performing design cases obtained from the parametric study. At 0.6 V, the CCL showed the maximum significance over the CMPL and PEM factors in terms of individual effect whereas the CCL and CMPL interaction was the most significant interaction effect. A synergistic benefit was observed from the combination of high-performing CCL and CMPL designs, which can be attributed to concurrent improvements in reaction kinetics and reduced ohmic resistance. On the other hand, at 0.4 V, the CMPL showed the strongest individual effect while the CCL and CMPL interaction was yet again the key interaction effect of significance. This was attributed to the well-managed oxygen transport and self-heating achieved with the thin, highly porous CMPL design as compared to the inferior baseline design. Overall, the strategic MEA design that leverages the jointly

improved CCL, CMPL, and PEM designs was shown to more than double the CD performance at both 0.6 and 0.4 V, as the collective benefits of this MEA design were able to induce simultaneous improvements in kinetic, ohmic, and mass transport properties aided by elevated cell temperature while retaining sufficient moisture to maintain good membrane hydration. A low rate of water sorption/desorption at the ionomer was also shown to be beneficial for the overall cell performance by virtue of improved water retention at the CCL under the relatively dry operating environment experienced by open-cathode PEMFCs. In summary, it is important to consider the significant coupling between the design of the individual MEA layers when designing open-cathode MEAs and fuel cells. Subject to strategic design improvements, the performance of open-cathode cells could eventually approach that of liquid-cooled cells, thus unlocking opportunities for greater power output and further cost reduction with simplified open-cathode fuel cell systems.

Acknowledgments

This work was supported by Indian Oil R&D Centre, Faridabad, India and Simon Fraser University, Canada under the SFU-IOCL joint PhD program in clean energy. This research was undertaken, in part, thanks to funding from the Canada Research Chairs program.

References

[1] Q. Meyer, A. Himeur, S. Ashton, O. Curnick, R. Clague, T. Reisch, P. Adcock, P. R. Shearing, and D. J. L. Brett, “System-level electro-thermal optimisation of air-cooled open-cathode polymer electrolyte fuel cells: Air blower parasitic load and schemes for dynamic operation,” in *International Journal of Hydrogen Energy*, 2015, vol. 40, no. 46, pp. 16760–16766.

[2] S. Shahsavari, M. Bahrami, and E. Kjeang, “Computational analysis of heat transfer in air-cooled fuel cells,” in *ASME 2011 9th International Conference on Fuel Cell Science, Engineering and Technology. Collocated with ASME 2011 5th International Conference on Energy Sustainability, FUELCELL 2011*, 2011, pp. 799–808, [Online]. Available: https://www.researchgate.net/publication/267498096.

[3] M. Andisheh-Tadbir, A. Desouza, M. Bahrami, and E. Kjeang, “Cell level modeling

of the hygrothermal characteristics of open cathode polymer electrolyte membrane fuel cells," *Int. J. Hydrogen Energy*, vol. 39, no. 27, pp. 14993–15004, 2014.

[4] Y. Wang, D. F. Ruiz Diaz, K. S. Chen, Z. Wang, and X. C. Adroher, "Materials, technological status, and fundamentals of PEM fuel cells – A review," *Mater. Today*, vol. 32, pp. 178–203, Jan. 2020, [Online]. Available: https://linkinghub.elsevier.com/retrieve/pii/S1369702119304948.

[5] A. G. Olabi, T. Wilberforce, and M. A. Abdelkareem, "Fuel cell application in the automotive industry and future perspective," *Energy*, vol. 214, p. 118955, 2021, [Online]. Available: https://www.sciencedirect.com/science/article/pii/S0360544220320624.

[6] M. M. Mench, *Fuel Cell Engines*. 2008.

[7] B. J. Kim and M. S. Kim, "Studies on the cathode humidification by exhaust gas recirculation for PEM fuel cell," *Int. J. Hydrogen Energy*, vol. 37, no. 5, pp. 4290–4299, Mar. 2012, [Online]. Available: https://linkinghub.elsevier.com/retrieve/pii/S0360319911026012.

[8] J. A. Kolde, "Advanced Composite Polymer Electrolyte Fuel Cell Membranes," *ECS Proc. Vol.*, vol. 1995–23, no. 1, pp. 193–201, 1995, [Online]. Available: http://dx.doi.org/10.1149/199523.0193PV.

[9] W. Liu, T. Suzuki, H. Mao, and T. Schmiedel, "Development of thin, reinforced PEMFC membranes through understanding of structure-property-performance relationships," *ECS Trans.*, vol. 50, no. 2, p. 51, 2013.

[10] A. Serov, K. Artyushkova, E. Niangar, C. Wang, N. Dale, F. Jaouen, M.-T. Sougrati, Q. Jia, S. Mukerjee, and P. Atanassov, "Nano-structured non-platinum catalysts for automotive fuel cell application," *Nano Energy*, vol. 16, pp. 293–300, 2015, [Online]. Available: https://www.sciencedirect.com/science/article/pii/S2211285515002876.

[11] S. T. Thompson and D. Papageorgopoulos, "Platinum group metal-free catalysts boost cost competitiveness of fuel cell vehicles," *Nat. Catal.*, vol. 2, no. 7, pp. 558–561, 2019, [Online]. Available: https://doi.org/10.1038/s41929-019-0291-x.

[12] F. S. Nanadegani, E. N. Lay, and B. Sunden, "Computational analysis of the impact of a micro porous layer (MPL) on the characteristics of a high temperature PEMFC," *Electrochim. Acta*, vol. 333, p. 135552, 2020.

[13] S. G. Kandlikar and Z. Lu, "Thermal management issues in a PEMFC stack–A brief review of current status," *Appl. Therm. Eng.*, vol. 29, no. 7, pp. 1276–1280, 2009.

[14] H. Pourrahmani, M. Moghimi, and M. Siavashi, "Thermal management in PEMFCs: the respective effects of porous media in the gas flow channel," *Int. J. Hydrogen Energy*, vol. 44, no. 5, pp. 3121–3137, 2019.

[15] G. Zhang and S. G. Kandlikar, "A critical review of cooling techniques in proton exchange membrane fuel cell stacks," *International Journal of Hydrogen Energy*,

vol. 37, no. 3. pp. 2412–2429, 2012.

[16] A. P. Sasmito, K. W. Lum, E. Birgersson, and A. S. Mujumdar, “Computational study of forced air-convection in open-cathode polymer electrolyte fuel cell stacks,” *J. Power Sources*, vol. 195, no. 17, pp. 5550–5563, 2010, [Online]. Available: http://dx.doi.org/10.1016/j.jpowsour.2010.02.083.

[17] G. Wasselynck, B. Auvity, J.-C. Olivier, D. Trichet, C. Josset, and P. Maindru, “Design and testing of a fuel cell powertrain with energy constraints,” *Energy*, vol. 38, no. 1, pp. 414–424, 2012, [Online]. Available: https://www.sciencedirect.com/science/article/pii/S0360544211007407.

[18] W. Liu, L. Wan, J. Liu, M. Zhao, and Z. Zou, “Performance improvement of the open-cathode proton exchange membrane fuel cell by optimizing membrane electrode assemblies,” *Int. J. Hydrogen Energy*, 2015.

[19] D. T. Santa Rosa, D. G. Pinto, V. S. Silva, R. A. Silva, and C. M. Rangel, “High performance PEMFC stack with open-cathode at ambient pressure and temperature conditions,” *Int. J. Hydrogen Energy*, 2007.

[20] F. Barreras, A. M. López, A. Lozano, and J. E. Barranco, “Experimental study of the pressure drop in the cathode side of air-forced Open-cathode proton exchange membrane fuel cells,” *Int. J. Hydrogen Energy*, vol. 36, no. 13, pp. 7612–7620, 2011.

[21] S. Kreesaeng, B. Chalermsinsuwan, and P. Piumsomboon, “Effect of Channel Designs on Open-Cathode PEM Fuel Cell Performance: A Computational Study,” 2015.

[22] C. Zhao, S. Xing, M. Chen, W. Liu, and H. Wang, “Optimal design of cathode flow channel for air-cooled PEMFC with open cathode,” *Int. J. Hydrogen Energy*, vol. 45, no. 35, pp. 17771–17781, 2020, [Online]. Available: https://doi.org/10.1016/j.ijhydene.2020.04.165.

[23] S. Kiattamrong and A. Sripakagorn, *Effects of the Geometry of the Air Flowfield on the Performance of an Open-Cathode PEMFC - Transient Load Operation*, vol. 79. Elsevier B.V., 2015.

[24] S. Thomas, A. Bates, S. Park, A. K. Sahu, S. C. Lee, B. R. Son, J. G. Kim, and D. H. Lee, “An experimental and simulation study of novel channel designs for open-cathode high-temperature polymer electrolyte membrane fuel cells,” *Appl. Energy*, 2016.

[25] S. Thomas, O. Kwon, S. C. Lee, S. Park, G. H. Choi, and J. Y. Choi, “Optimized Flow Distribution for Enhancing Temperature Uniformity across an Open Cathode PEM Fuel Cell Stack,” *ECS Trans.*, vol. 58, no. 1, pp. 243–249, 2013, [Online]. Available: http://ecst.ecsdl.org/content/58/1/243.abstract.

[26] A. Sagar, S. Chugh, K. Sonkar, A. Sharma, and E. Kjeang, “A computational analysis on the operational behaviour of open-cathode polymer electrolyte membrane fuel cells,” *Int. J. Hydrogen Energy*, vol. 45, no. 58, pp. 34125–34138, Oct. 2020, [Online]. Available: https://doi.org/10.1016/j.ijhydene.2020.09.133.

[27] H. Al-Zeyoudi, A. P. Sasmito, and T. Shamim, “Performance evaluation of an open-cathode PEM fuel cell stack under ambient conditions: Case study of United Arab Emirates,” *Energy Convers. Manag.*, 2015.

[28] A. Alanazi, “Performance evaluation of air breathing PEMFC under Saudi Arabia ’ s ambient conditions using three-dimensional FEM model,” 2017, pp. 1–14.

[29] B. Wu, B. Li, W. Liu, J. Liu, M. Zhao, Y. Yao, J. Gu, and Z. Zou, “The performance improvement of membrane and electrode assembly in open-cathode proton exchange membrane fuel cell,” 2013, [Online]. Available: http://dx.doi.org/10.1016/j.ijhydene.2013.01.149.

[30] Q. Meyer, K. Ronaszegi, G. Pei-June, O. Curnick, S. Ashton, T. Reisch, P. Adcock, P. R. Shearing, and D. J. L. Brett, “Optimisation of air cooled, open-cathode fuel cells: Current of lowest resistance and electro-thermal performance mapping,” *J. Power Sources*, vol. 291, pp. 261–269, 2015.

[31] W. Liu, L. Wan, J. Liu, M. Zhao, and Z. Zou, “Performance improvement of the open-cathode proton exchange membrane fuel cell by optimizing membrane electrode assemblies,” *Int. J. Hydrogen Energy*, vol. 40, no. 22, pp. 7159–7167, Jun. 2015, [Online]. Available: https://linkinghub.elsevier.com/retrieve/pii/S0360319915008897.

[32] A. Sagar, S. Chugh, A. Sharma, and E. Kjeang, “Strategic ionomer design for high performing fuel cells with open cathode,” *Int. J. Hydrogen Energy*, vol. 47, no. 3, pp. 1940–1946, 2022, [Online]. Available: https://doi.org/10.1016/j.ijhydene.2021.10.131.

[33] R. Omrani and B. Shabani, “Review of gas diffusion layer for proton exchange membrane-based technologies with a focus on unitised regenerative fuel cells,” *Int. J. Hydrogen Energy*, vol. 44, no. 7, pp. 3834–3860, 2019, [Online]. Available: https://www.sciencedirect.com/science/article/pii/S0360319918340886.

[34] T. Kitahara, H. Nakajima, and K. Mori, “Hydrophilic and hydrophobic double microporous layer coated gas diffusion layer for enhancing performance of polymer electrolyte fuel cells under no-humidification at the cathode,” *J. Power Sources*, vol. 199, pp. 29–36, 2012, [Online]. Available: http://dx.doi.org/10.1016/j.jpowsour.2011.10.002.

[35] R. W. Atkinson, J. A. Rodgers, M. W. Hazard, R. O. Stroman, and B. D. Gould, “Influence of cathode gas diffusion media porosity on open-cathode fuel cells,” *J. Electrochem. Soc.*, vol. 165, no. 11, pp. F1002–F1011, 2018.

[36] R. W. Atkinson, M. W. Hazard, J. A. Rodgers, R. O. Stroman, and B. D. Gould, “Influence of Gas Diffusion Media Compression on Open-Cathode Fuel Cells,” *J. Electrochem. Soc.*, vol. 166, no. 13, pp. F926–F934, 2019.

[37] S. Shahsavari, A. Desouza, M. Bahrami, and E. Kjeang, “Thermal analysis of air-cooled PEM fuel cells,” *Int. J. Hydrogen Energy*, vol. 37, no. 23, pp. 18261–18271, 2012.

[38] A. J. Navarro, M. A. Gómez, L. Daza, A. Molina-García, and J. J. López-Cascales, “Influence of the gas diffusion layer on the performance of an open cathode

polymer electrolyte membrane fuel cell," *Int. J. Hydrogen Energy*, vol. 47, no. 12, pp. 7990–7999, 2022.

[39] Q. Meyer, S. Ashton, P. Boillat, M. Cochet, E. Engebretsen, D. P. Finegan, X. Lu, J. J. Bailey, N. Mansor, R. Abdulaziz, *et al.*, "Effect of gas diffusion layer properties on water distribution across air-cooled, open-cathode polymer electrolyte fuel cells: A combined ex-situ X-ray tomography and in-operando neutron imaging study," *Electrochim. Acta*, vol. 211, pp. 478–487, 2016, [Online]. Available: https://www.sciencedirect.com/science/article/pii/S0013468616313858.

[40] F. Brèque, J. Ramousse, Y. Dubé, K. Agbossou, and P. Adzakpa, "Sensibility study of flooding and drying issues to the operating conditions in PEM Fuel Cells," *Int. J. Energy Environ. IJEE*, vol. 1, no. 1, pp. 1–20, 2010.

[41] S.-J. Shin, J.-K. Lee, H.-Y. Ha, S.-A. Hong, H.-S. Chun, and I.-H. Oh, "Effect of the catalytic ink preparation method on the performance of polymer electrolyte membrane fuel cells," *J. Power Sources*, vol. 106, no. 1–2, pp. 146–152, Apr. 2002, [Online]. Available: https://linkinghub.elsevier.com/retrieve/pii/S037877530101045X.

[42] Y.-H. Cho, H.-S. Park, Y.-H. Cho, D.-S. Jung, H.-Y. Park, and Y.-E. Sung, "Effect of platinum amount in carbon supported platinum catalyst on performance of polymer electrolyte membrane fuel cell," *J. Power Sources*, vol. 172, no. 1, pp. 89–93, Oct. 2007, [Online]. Available: https://linkinghub.elsevier.com/retrieve/pii/S0378775307002418.

[43] J. Marquis and M.-O. Coppens, "Achieving ultra-high platinum utilization via optimization of PEM fuel cell cathode catalyst layer microstructure," *Chem. Eng. Sci.*, vol. 102, pp. 151–162, Oct. 2013, [Online]. Available: https://linkinghub.elsevier.com/retrieve/pii/S0009250913005460.

[44] Y. Liu, M. W. Murphy, D. R. Baker, W. Gu, C. Ji, J. Jorne, and H. A. Gasteiger, "Proton Conduction and Oxygen Reduction Kinetics in PEM Fuel Cell Cathodes: Effects of Ionomer-to-Carbon Ratio and Relative Humidity," *J. Electrochem. Soc.*, vol. 156, no. 8, p. B970, 2009.

[45] T. F. Cao, H. Lin, L. Chen, Y. L. He, and W. Q. Tao, "Numerical investigation of the coupled water and thermal management in PEM fuel cell," *Appl. Energy*, vol. 112, pp. 1115–1125, 2013, [Online]. Available: http://dx.doi.org/10.1016/j.apenergy.2013.02.031.

[46] A. Z. Weber and J. Newman, "Effects of Microporous Layers in Polymer Electrolyte Fuel Cells," *J. Electrochem. Soc.*, vol. 152, no. 4, p. A677, 2005.

[47] M. El Hannach, R. Singh, N. Djilali, and E. Kjeang, "Micro-porous layer stochastic reconstruction and transport parameter determination," *J. Power Sources*, vol. 282, pp. 58–64, 2015, [Online]. Available: http://dx.doi.org/10.1016/j.jpowsour.2015.02.034.

[48] J. H. Nam and M. Kaviany, "Effective diffusivity and water-saturation distribution in single- and two-layer PEMFC diffusion medium," *Int. J. Heat Mass Transf.*, vol. 46, no. 24, pp. 4595–4611, 2003.

[49] J. Zhou, S. Shukla, A. Putz, and M. Secanell, “Analysis of the role of the microporous layer in improving polymer electrolyte fuel cell performance,” *Electrochim. Acta*, vol. 268, pp. 366–382, Apr. 2018, [Online]. Available: https://linkinghub.elsevier.com/retrieve/pii/S0013468618304043.

Nomenclature

a_v	Active specific surface area (m^{-1})
A_{cell}	Active electrochemical area (m^2)
c_i	Molar concentration of i^{th} species (mol m^{-3})
D	Gas phase diffusivity (m s^{-1})
F	Faraday’s constant (C mol^{-1})
j	Current density (A m^{-2})
m_{Pt}	Platinum loading (g m^{-2})
Pt/C	Percentage platinum on carbon (%)
P	Pressure (Pa)
R	Gas constant (J mol^{-1} K^{-1})
S	Source
t_i	Thickness of i^{th} domain (m)
T	Temperature (K)
u	Velocity vector (m s^{-1})
V	Volume (m^3)
$\dot{V}$	Volumetric flow rate (m^3 s^{-1})
W	Weight (kg)

wt_{ion}	Ionomer loading (%)
x_{O_2}	Mole fraction of oxygen (%)

Greek symbols

α_i	Charge transfer coefficient at i^{th} electrode
γ	Water sorption/desorption rate constant (s^{-1})
ε_i	Volume fraction of i^{th} domain
η	Overpotential (V)
λ	Water content
σ_i	Effective electrolyte conductivity of i^{th} domain (S m^{-1})
Σ	Summation
ϕ_i	Potential at i^{th} electrode (V)

Acronyms

3D	Three dimensional
ANOVA	Analysis of variance
BC	Boundary condition
BPP	Bi-polar plate
CL	Catalyst layer
CCL	Cathode catalyst layer

CD	Current density
CMPL	Cathode microporous layer
DoE	Design of experiments
FF	Flow field
GDL	Gas diffusion layer
H	High
L	Low
MEA	Membrane electrode assembly
MPL	Microporous layer
MT	Mass transfer
ORR	Oxygen reduction reaction
PEM	Polymer electrolyte membrane
PEMFC	Polymer electrolyte membrane fuel cell
Pt	Platinum
Pt/C	Platinum on carbon
RH	Relative humidity
VLB	Voltage loss breakdown

Subscripts

a	Anode
c	Cathode

C	Carbon
eff	Effective
in	Inlet
ion	Ionomer
m	Membrane
mol	Molar
ohm	Ohmic
ref	Reference
s	Solid
sat	Saturation
v	Volumetric

Appendix D

Experimental design of high-performing open-cathode polymer electrolyte membrane fuel cells

Abstract

The performance of open-cathode fuel cell systems is generally restricted by poor humidification, high membrane resistance, higher charge transfer resistance, and overheating of the cell due to inefficient thermal and water management. This work aims at strategically designing the membrane electrode assembly (MEA) to improve the overall performance of such systems by minimizing the various losses limiting their performance. Five different MEA designs are fabricated and tested using a 25 cm^2 open-cathode single-cell setup operated at the ambient condition of 40 $^{\circ}C$ and 40% relative humidity. Short side chain ionomer is found to improve the performance compared to the incumbent long side chain ionomer due to increased water retention at the cathode catalyst layer. A thinner membrane with short side chain ionomer is also found to elevate the cell performance by minimizing the ohmic losses at dry conditions. Thinner gas diffusion layers with high porosity enable additional cell performance increment by improving oxygen availability at the cathode catalyst layer. An overall current density rises of 88% at 0.6 V and 53% at 0.4 V is achieved by the strategically designed MEA for open-cathode cells offering increased power density and thus lower cost compared to conventional open-cathode fuel cell designs.

Keywords: fuel cell; open cathode; performance; ionomer; membrane; gas diffusion layer

Introduction

Open-cathode polymer electrolyte membrane fuel cells (PEMFCs) have been gaining popularity for portable applications and other mid-range power applications considering the recent system advancements and the simple design of such systems [1]. In open-cathode cells, dry hydrogen is generally fed on the anode side and one or more fans in front of the cells blow ambient air on the cathode side by forced convection [2]. The air blown into the system through the open channels at the cathode not only provides oxygen (O_2) for the electrochemical reaction but also cools down the cell and maintains the internal temperature through heat extraction [3]. The need for liquid cooling is thus eliminated in contrast to conventional PEMFCs and the system design is simplified [4]. However, cell overheating caused by inefficient heat removal [5-6], membrane dehydration due to low humidity operations [7], high ohmic resistance possessed by increased membrane ionic resistance, and lower cell kinetics [8] are some of the key challenges associated with open-cathode fuel cell systems. The humidification of the ionomer in the membrane and catalyst layers (CLs) plays an important role in the overall performance of the cell. The water uptake dynamics of the ionomer are found to be strong functions of temperature [9]. At high relative humidity (RH) conditions where humidification is sufficient; a CL with a high electrochemical surface area (ECSA) catalyst is generally expected to perform better than a low ECSA catalyst given that the Pt loading and ionomer to carbon ratio remain the same for both cases. Whereas, at dry operating conditions even the increase in ECSA is not able to boost the cell performance due to poor protonic conduction [10]. The water sorption/desorption rate constant (γ) of the ionomer was therefore recently hypothesized to be an influential factor for the overall performance of open-cathode PEMFCs [11]. Based on predictions from computational modelling of an open-cathode cell, a lower γ ionomer is anticipated to support the cell performance by providing better water retention capability within the ionomer phase of the CL [11]. To date, however, there are no experimental reports available to corroborate these predictions. The equivalent weight (EW) of the ionomer has also been reported to influence cell performance for open-cathode systems. The use of a high EW ionomer with 1100 EW over 850 EW was found to possess improved cell hydration due to lower mass transport resistance as determined by electrochemical impedance spectroscopy (EIS) studies [12]. Also, low EW ionomers were reported to have high O_2 transport resistance and high ECSA at the same time as compared to high EW ionomers while operating under both dry and wet conditions in

conventional liquid-cooled PEMFCs [13-14]. Similarly, Garsany *et al.* reported that short side chain (SSC) ionomers with lower EW produce superior cell performance compared to long side chain (LSC) ionomers with higher EW for RH conditions ranging from 50% to 100% [15]. While these reports are important for conventional liquid-cooled PEMFCs, the findings may not be transferable to the unique operating conditions and local environment within open-cathode cells. The effect of membrane selection is also lacking in the literature for open-cathode cells, whereas it is relatively well established that thin, reinforced membranes are favourable for high performing liquid-cooled cells due to reduced ohmic resistance [16-17].

Gas diffusion layers (GDLs) may also play an important role in determining the overall cell performance by facilitating water and gas transport across the cell [18]. The addition of a microporous layer (MPL) on the CL side of a GDL generally benefits the performance of conventional PEMFCs [19] due to improved O_2 transport at the membrane electrode assembly (MEA) level and reduced mass transport resistance [20–22]. The inclusion of an MPL was also found to provide improved voltage stability [23]. However, the extent of potential MPL benefits for open-cathode cells has not yet been established. Within the GDL, the porosity available for gas phase transport is dependent on the presence of liquid water, which may cause flooding in conventional liquid-cooled PEMFCs. Hence, high GDL porosity is found to support the cell performance by increasing the O_2 transport at high current densities. However, the GDL porosity typically has less influence on the polarization level at medium or low current density (CD) [24-25]. The GDL thickness is also an important parameter. Reduction in GDL thickness was found to support the cell performance of conventional PEMFCs as a consequence of reduced mass transport resistance of the liquid and gaseous flow [21]. On the contrary, Zhou *et al.* [26] suggested the use of thinner GDLs to facilitate higher water content and improved hydration for the membrane. A similar modelling study by Jeng *et al.* [27] reported the dependence on PEMFC performance based on the GDL porosity and thickness. At low GDL porosity, a reduced thickness was found supportive of the cell performance. Whereas, at high GDL porosity the requirement of an optimal thickness of the GDL showed a reverse trend. The pore size distribution and hydrophobicity of the GDL are some of the other parameters which govern the overall cell performance to various extents [28–32]. Overall, the literature is rich in contributions investigating the effect of various GDL parameters such as porosity, thickness, hydrophobicity, and pore size on the performance of conventional liquid-cooled

PEMFCs. A few of the reports mention GDL impacts on air-breathing cells and air-cooled cells with separate air flow channels [33-35]. In the case of open-cathode PEMFCs with combined cathode air flow and cooling channels, Atkinson *et al.* [36] reported the impact of GDL porosity on the hydration levels of the cell, electrical resistance, and thermal profile. Cathode charge transfer, cell hydration, and thermal management were reported to be improved with a small decrement in GDL porosity. However, recent modelling results from our group [37] suggested the contrary effect of MPL selection in the GDL with highly porous, thin MPL being advantageous for open-cathode PEMFC operation due to reduced O_2 transport resistance. The need for further research to explore the GDL influence on various cell related parameters for open-cathode PEMFCs is therefore evident.

The present work addresses the critical gap in the literature on MEA design and component material selection specifically for high-performing open-cathode PEMFCs. The objective of this work is to experimentally determine the effects of CL ionomer type, membrane thickness, and GDL/MPL design on the overall cell performance of open-cathode fuel cells. The fabrication and testing of several MEAs are carried out and a novel MEA configuration are proposed to enhance the performance of open-cathode cells by minimizing the limitations offered by a baseline MEA originating from conventional MEA design for liquid-cooled fuel cells. A total of five different MEAs are tested to understand the individual as well as combined effects of ionomer, membrane, and GDL changes on the open-cathode cell performance using a single-cell experimental setup with a 25 cm^2 active area. The results obtained for all the MEAs in the form of achieved CD at fixed cell voltages, impedance data, and temperature profiles are compared and assessed. The results are also compared with theoretical predictions obtained from numerical modelling of open-cathode fuel cells [8], [11].

Materials

A total of five MEAs are fabricated for evaluating the effect of different materials by changing one of the components of the MEA at a time. The baseline MEA for this work, MEA-1, is taken as the commercial MEA procured from Ion Power Inc. with specifications given in Table D.1. It is a catalyst coated membrane (CCM) based MEA with an active area of 25 cm^2 having 60% Pt/C on Vulcan type carbon support and Nafion® type LSC ionomer and membrane. MEA-2, MEA-3, MEA-4, and MEA-5 are prepared in-house by

following similar methods with specifications as in Table D.1. The MEA-2 is prepared with similar composition as MEA-1 to establish the in-house MEA preparation capability and validate the baseline results. The effect of SSC ionomer on the cell performance of open-cathode systems is studied by changing the ionomer material for MEA-3 as compared to MEA-2 while keeping other compositional parameters the same as for MEA-2. A subsequent change in the membrane by using Aquivion-720-20 is done for MEA-4 to analyze the effect of the SSC membrane in conjunction with a similar ionomer. As an additional step, in MEA-5 the GDL is changed from SGL 29BC to SGL 22BB on the cathode electrode to access the effect of thinner GDL with high porosity on open-cathode cell performance. The slurry ink is prepared by mixing Vulcan carbon supported 60% Pt/C of PK catalyst along with ionomer and solvent. The same catalyst is used for preparing all the in-house MEAs with fixed Pt loading of 0.5 mg cm^{-2} on both anode and cathode CLs. The catalyst is measured as per the loading of individual MEAs and wetted with 2-3 drops of deionized water with mixing done using a glass rod before preparation of the catalyst ink slurry. The respective ionomer is measured separately and added to the slurry dropwise. 5 wt% of Nafion® D521- 1100 EW is taken as the initial ingredient for ionomer solution while preparing MEA-2 whereas 25 wt% of Aquivion D72-25BS is used for MEA-3, 4, and 5. A mixture of 2 ml of deionized water and 18 ml of ethanol is used as a solvent for preparing the slurry ink solution required for coating each side of the membrane. The process of slurry ink formation involves the first step of adding half of the solvent to the weighed catalyst and ultrasonic stirring for 15 min. In the next step, the ionomer is added with the remaining solvent and the solution is then subjected to ultrasonic stirring for another 20 min. The same process is followed for each MEA preparation. Once the catalyst ink slurry is ready, it is sprayed on the desired PEM using Flair Stainless Steel Multipurpose Air Brush Paint Spray Gun on both sides. While spraying the ink solution on the PEM, a temperature of 60˚C is maintained at the base plate where the PEM is placed to ensure uniform drying of the ink. The spray gun is operated at a pressure of 20 psi using dry nitrogen gas for a uniform flow of slurry and to achieve uniform contact of the slurry onto the membrane. Both anode and cathode CLs are spray coated using the same procedure.

Table D.1. Details of the different MEAs prepared for open-cathode fuel cell testing.

	Anode	Cathode	PEM

MEA-1 **(Commercial)**	m_{Pt} = 0.5 mg cm^{-2} GDL - SGL 29BC Ionomer – Nafion® (D521- 1100 EW)	m_{Pt} = 0.5 mg cm^{-2} GDL - SGL 29BC Ionomer – Nafion® (D521- 1100 EW)	Nafion® 212
MEA-2	m_{Pt} = 0.5 mg cm^{-2} GDL - SGL 29BC Ionomer – Nafion® (D521- 1100 EW)	m_{Pt} = 0.5 mg cm^{-2} GDL - SGL 29BC Ionomer – Nafion® (D521- 1100 EW)	Nafion® 212
MEA-3	m_{Pt} = 0.5 mg cm^{-2} GDL - SGL 29BC Ionomer – Aquivion (D72-25BS – 720 EW)	m_{Pt} = 0.5 mg cm^{-2} GDL - SGL 29BC Ionomer – Aquivion (D72-25BS – 720 EW)	Nafion® 212
MEA-4	m_{Pt} = 0.5 mg cm^{-2} GDL - SGL 29BC Ionomer – Aquivion (D72-25BS – 720 EW)	m_{Pt} = 0.5 mg cm^{-2} GDL - SGL 29BC Ionomer – Aquivion (D72-25BS – 720 EW)	Aquivion – 720-20
MEA-5	m_{Pt} = 0.5 mg cm^{-2} GDL - SGL 29BC Ionomer – Aquivion (D72-25BS – 720 EW)	m_{Pt} = 0.5 mg cm^{-2} GDL - SGL 22BB Ionomer – Aquivion (D72-25BS – 720 EW)	Aquivion – 720-20

Experimental setup and test procedure

The performance of the five MEAs is evaluated by performing single-cell tests on an open-cathode PEMFC with an active area of 25 cm^2. The single-cell test setup from Figure D.1 is equipped with an external duct made up of PA2200 Nylon to carry the ambient air onto the open channels on the cathode side. Ethylene propylene diene monomer rubber gaskets are used at the junction of the duct and the graphite plates open channels to arrest leaks across the duct. The single-cell setup consists of graphite plates with serpentine channels on the anode side and open channels grooved on the cathode side plate with dimensions as listed in Table D.2. The graphite plates are compressed in a single cell fuel cell hardware consisting of gold-plated current collectors and aluminium end plates with eight bolts across the plates which are tightened by providing manual torque of 4 Nm at each of the bolts. The MEA is placed between the two graphite plates consisting of spray coated CCM with GDL on both sides. The edges of the MEA are sealed by using a Teflon gasket on both sides of the membrane having a suitable thickness.

Table D.2. Dimensions of anode and cathode flow field plates used for experimental evaluation of single-cell open-cathode PEMFCs.

	Flow channel configuration	Width (mm)		Depth (mm)	Length (mm)
		Rib	Channel		
Anode	Single serpentine	1.0	1.0	0.7	50
Cathode	Open-channel (Parallel)	0.85	2.0	2.0	50

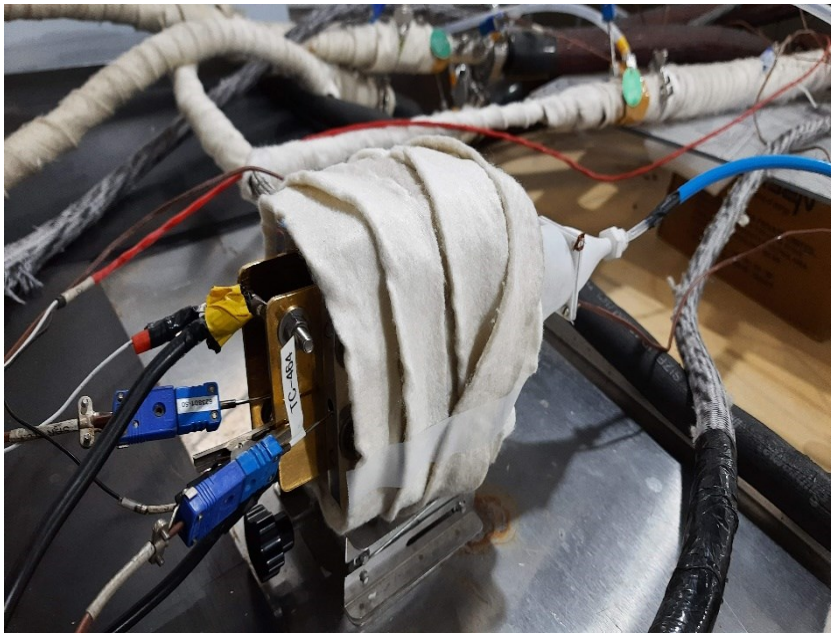

Figure D.1. Open-cathode single-cell setup for testing.

The MEAs are tested in the open-cathode single-cell setup at an operating ambient air condition of 40˚C and 40% RH. The test setup is placed in an environmental chamber connected with a Greenlight Innovation G400 test station inside which the ambient air condition is maintained. A small air compression device is installed inside the environmental chamber which delivers the air to the open-cathode channels through pipe fittings connected to the duct at ambient pressure. A manual rotameter is connected along the pipe fittings to control the air flow rate at 2.5 nlpm for all the experimental conditions at all current densities. This cathode side flow rate corresponds to air stoichiometry of nearly 12 at the operating current density of 0.5 A cm^{-2} for the current MEA active area of 25 cm^2. The anode side uses 99.999% pure H_2 fed at an operating temperature of 40˚C and ambient pressure. The flow is kept at 0.5 nlpm with RH of the incoming gas maintained at 60% mimicking dead-end mode operating conditions [38]. The single-cell setup is enclosed by glass wool across all the peripheries to suppress any loss of heat generated within the system and thus direct the heat dissipation to the air channels. The fuel cell tests are performed by measuring the steady state current density at fixed cell voltages of 0.6 V and 0.4 V until the thermal equilibrium is achieved for each case in 40-60 min. The thermal equilibrium is monitored by the temperature recorded as T1, T2, and T3 at the central open cathode channel at the cathode-GDL interface, center of the cathode side

solid graphite plate, and the cathode endplate using thermocouples TC1, TC2, and TC3 respectively as reported in Figure D.2 (a).

The conditioning of individual MEAs is performed using the same active area liquid-cooled setup operating at 60˚C with three sets of 100 cyclic voltammetry scans performed at the scan rate of 50 mV s^{-1}, constant voltage operation at 0.6 V for 4-5 h, and polarization curve measurement before actual data collection on the open-cathode setup. The fuel cell current density is recorded for the open-cathode single cell for each of the MEAs while operating at 0.6 V and 0.4 V respectively. Three repeated measurements are taken on each individual MEA to ensure the reproducibility of the results. EIS is performed in potentiostatic mode at 0.6 V for each of the MEAs with the frequency range scanned from 1 kHz to 0.1 Hz with AC perturbation voltage of 5 mV using Gamry Reference 5000 E with a booster connected to the Greenlight Innovation G400 test station for data acquisition.

Results and Discussion

(a)

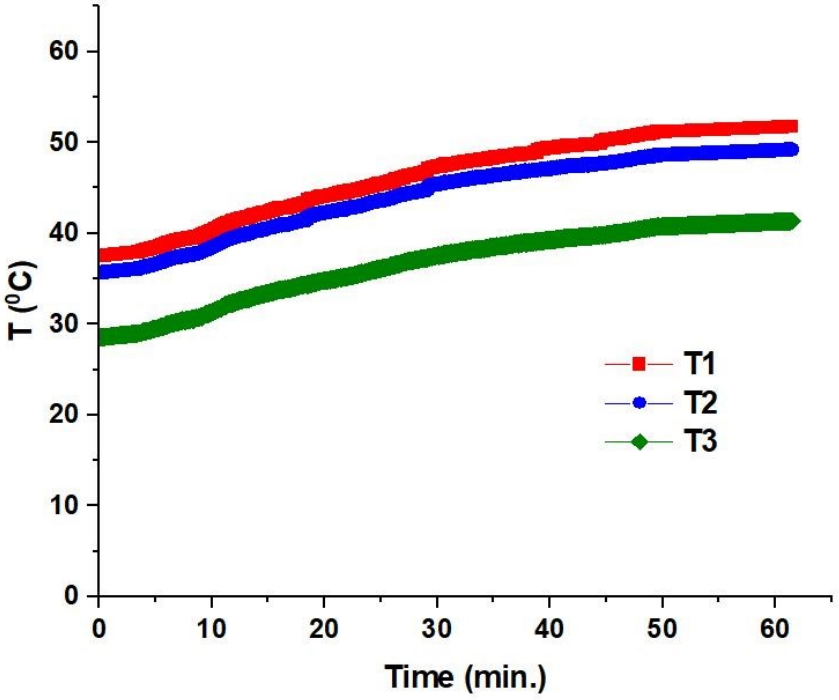

(b)

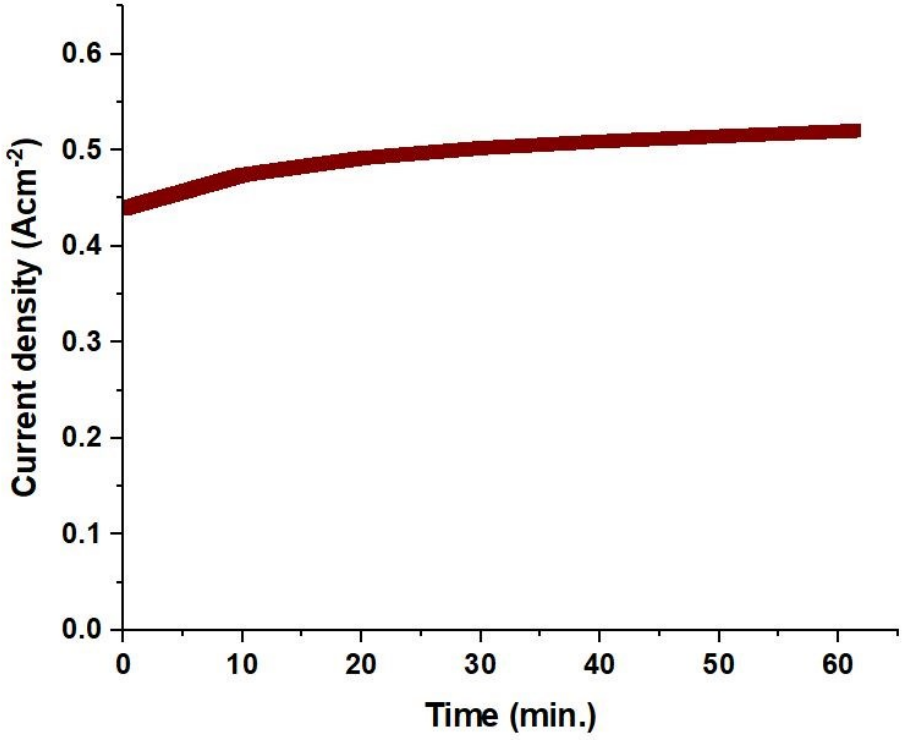

Figure D.2. (a) Thermal equilibration data for MEA-3 while operating at 0.4 V where, T1, T2, and T3 are the temperature at the central open cathode channel at the cathode-GDL interface, center of the cathode side solid graphite plate, and the cathode endplate respectively. (b) Current density at 0.4 V for MEA-3 during thermal equilibration.

Figure D.2 (a) shows the thermal equilibration data for MEA-3 which depicts the trends of T1, T2, and T3 measured using TC1, TC2, and TC3 while operating at 0.4 V where, T1, T2, and T3 are the temperature at the central open cathode channel at the cathode-GDL interface, center of the cathode side solid graphite plate, and the cathode endplate respectively. The internal temperatures at the cathode channel-GDL interface and graphite plate increase due to self-heating and reach nearly 52˚C while operating at the given current density, whereas the external cathode endplate remains at a proportionally lower temperature of around 40˚C which is near the ambient operating condition. The system is found to be equilibrated after approximately 50 min while operating at 0.4 V with a rise below 0.05˚C min^{-1}. The current density starts from an initial value of 0.44 A cm^{-2} and rises slightly until it equilibrates at 0.52 A cm^{-2} as depicted in Figure D.2 (b). As

expected due to self-heating, most notably within the MEA at the center of the cell, the rise in internal cell temperature appears to lag the rise and equilibration in CD, until a new thermal equilibrium is established under the steady state open-cathode fuel cell operating condition. The internal cell temperature reaches a higher value at 0.4 V than at 0.6 V due to the higher CD and increased heat generation. A similar thermal equilibrium is achieved for each of the MEAs before recording the fuel cell data. The measured CDs for all the tested MEAs are captured in Figure D.3 while being operated at 0.6 V and 0.4 V along with error bars for the three repeats of each polarization data captured.

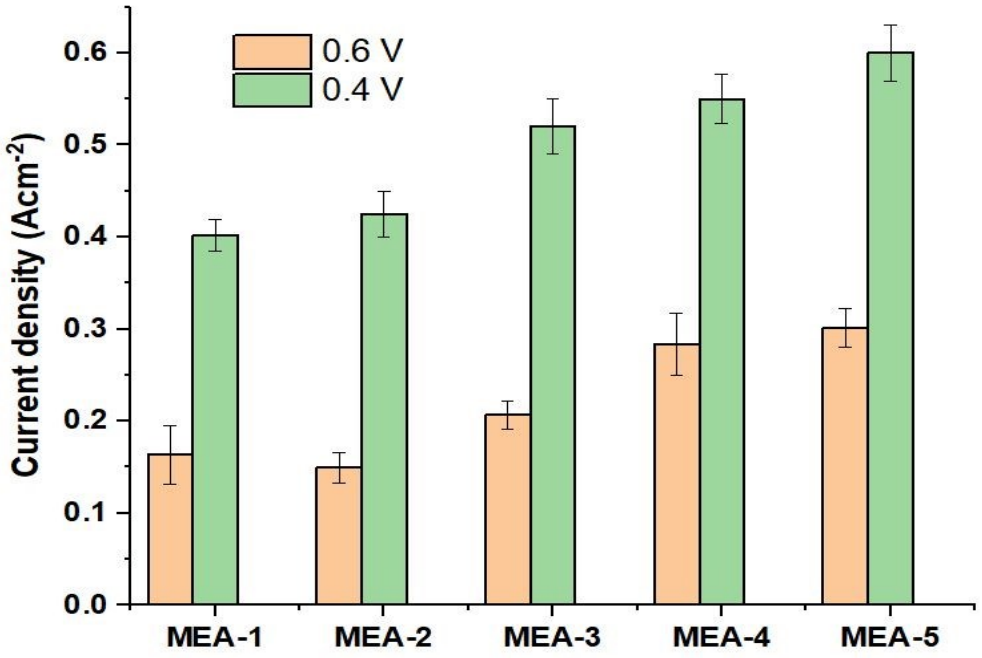

Figure D.3. Current density for the five MEAs operated at cell voltages of 0.6 V and 0.4 V at steady state, following thermal equilibration.

Table D.3. Average current density data obtained for single-cell open-cathode fuel cells operated at 0.6 V and 0.4 V using five different MEAs.

	Avg. current density (A cm^{-2}) at 0.6 V	% Change in CD w.r.t. baseline (at 0.6 V)	Avg. current density (A cm^{-2}) at 0.4 V	% Change in CD w.r.t. baseline (at 0.4 V)

MEA-1	0.16	0.0	0.40	0.0
MEA-2	0.15	-6.2	0.42	5.0
MEA-3	0.21	31.2	0.52	30.0
MEA-4	0.28	75.0	0.55	37.5
MEA-5	0.30	87.5	0.61	52.5

The average CD and the percentage change in CD with respect to the baseline MEA test data are presented in Table D.3 for further understanding. For the in-house fabricated MEA-2 with a similar composition to that of the commercial MEA-1, the average CD is found to be nearly the same with a deviation of 6% at an operating cell voltage of 0.6 V and 5% at 0.4 V. This trend validates the repeatability of the MEA performance at the same operating condition and similar MEA composition. The slight deviation can be attributed to the different methods of MEA preparation. MEA-3 is found to give a CD increment of 31% at 0.6 V and 30% at 0.4 V respectively with reference to the baseline performance of MEA-1. This increase in CD is attributed to the change in ionomer as compared to MEA-2, the Aquivion ionomer which has lower EW and short-side chain polymer structure with reference to the Nafion® ionomer used in the baseline MEA. This improvement is likely due to better water retention capability at the ionomer sites in the CL [39] and may also be related to the low water sorption/desorption rate constant inherent to SSC ionomer [11]. Next, the change in membrane from Nafion® 212 to Aquivion 720 along with the ionomer change with respect to the baseline for MEA-4 leads to a significant improvement in CD by 75% at 0.6 V and 38% at 0.4 V respectively. The higher rate of increment observed at medium current density operation at 0.6 V is attributed to the decreased ohmic resistance due to the lesser membrane thickness of 20 μm used for MEA-4 as compared to 50 μm in the baseline MEA. Also, the use of Aquivion membrane in MEA-4 compared to Nafion® membrane for the baseline may benefit from the improved water absorption capability of the Aquivion membrane pertaining to its SSC structure and low EW [40-41]. This also adds to the increased water content at the membrane-CL region of the MEA which is contributing to the elevated CD. A further boost in CD by 13% at 0.6 V is found for MEA-5 as compared to MEA-4, whereas the increment at 0.4 V is 15%. This increase in CD is attributed to the modified GDL used in MEA-5, which is thinner and has

a higher porosity than the baseline GDL used in the other MEAs. More specifically, the modified GDL features a thickness reduction from 235 to 215 μm and a reduced areal weight from 90 to 70 g m^{-2}. The reduced GDL thickness and increased porosity are expected to jointly reduce the O_2 diffusion resistance in the MEA with increased O_2 availability at the active sites of the cathode CL (CCL) [37]. This leads to an enhanced rate of reaction and thus resulting in increased CD.

The measured average temperatures T1, T2, and T3 after reaching thermal equilibrium at 0.4 V operation are shown in Figure D.4. Overall, the cell temperature is observed to be higher for the MEAs with higher CDs and closely follows the trend established in the cell performance data. Accordingly, the highest temperature is observed for MEA-5, which is the highest performing MEA out of the five MEAs being tested. Similarly, the highest incremental temperature rise is observed for MEA-3 versus MEA-2, in agreement with its high CD increment stemming from the improved ionomer type. This indicates the direct dependence of temperature distribution on the CD which is further associated with the improvement in the MEA design. These findings are consistent with theoretical expectations, as the waste heat generation at a given cell voltage is proportional to CD, as well as numerical modelling predictions for open-cathode PEMFCs [8], [11]. The temperature increment may also benefit the overall cell performance through enhanced kinetics, but only if membrane hydration can be maintained.

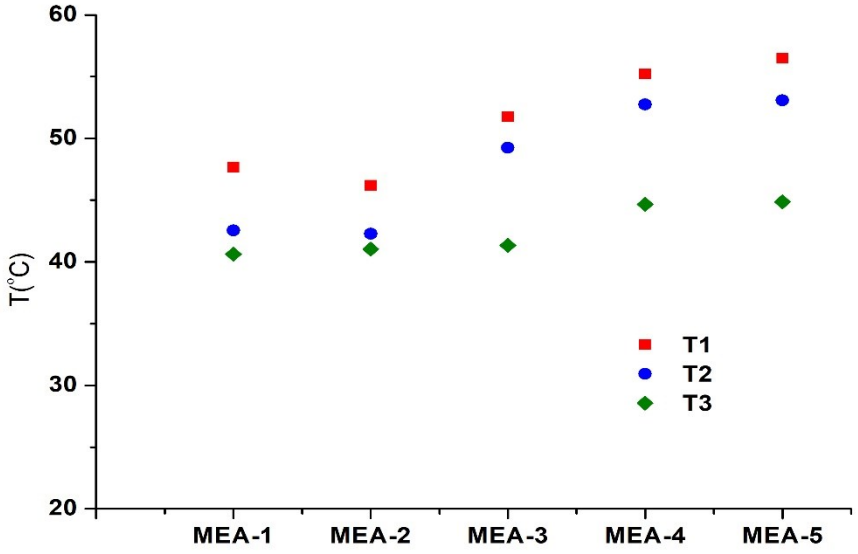

Figure D.4. Average temperatures (T1, T2, and T3) reached at thermal equilibrium for the five MEAs at 0.4 V operation.

The Nyquist plot obtained from the EIS data for the five different MEAs is shown in Figure D.5 while operating at 0.6 V. The high-frequency resistance (HFR) decreases subsequently from MEA-1 to MEA-5. This trend agrees with the CD data obtained for these cases and asserts the performance increment for the subsequent MEA design. The HFR values for MEA-1 and MEA-2 are essentially equal with only 2% deviation and justify the similar composition of the two MEAs being operated at the same ambient conditions. However, the second x-axis intercept representing the charge transfer resistance (R_{ct}) is lower for MEA-2 compared to MEA-1. This can be attributed to the difference in kinetic overpotential possessed by these two MEAs which is likely related to variations in catalyst microstructure.

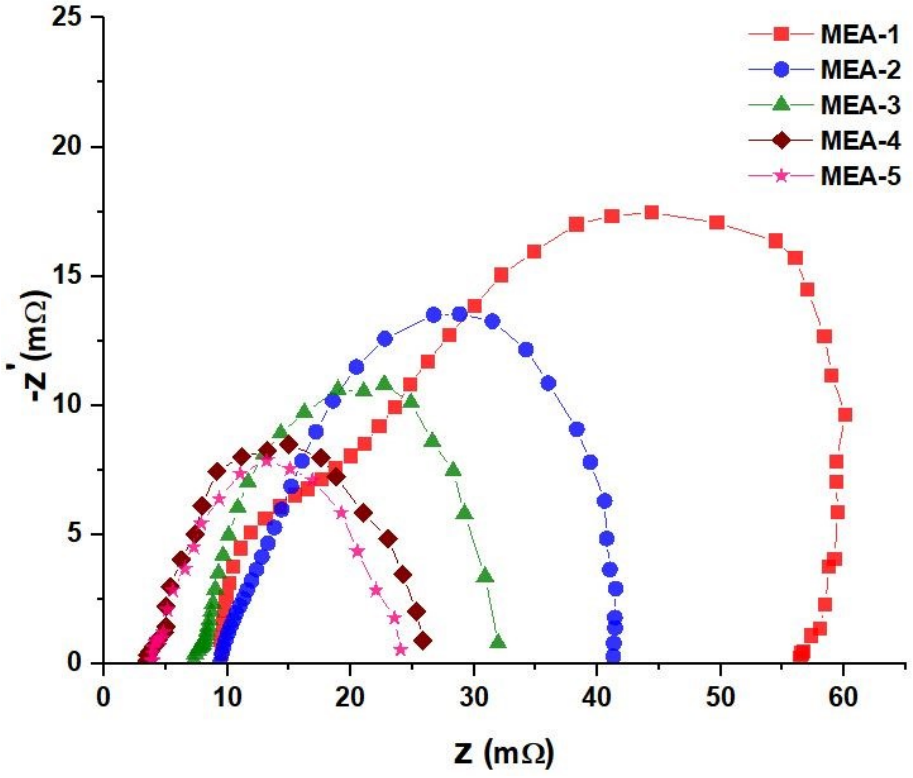

Figure D.5. Comparative Nyquist plot of impedance for the five MEAs obtained by in-situ EIS on the single cell open-cathode fuel cell operated at 0.6 V.

The HFR reduces from 9.39 mΩ for MEA-2 to 7.26 mΩ for MEA-3, following the change in ionomer from Nafion® D521 to Aquivion D72-25BS. However, the protonic resistance of the ionomer in the CLs is only a minor contribution to the combined ohmic cell resistance measured by HFR. Hence, the 23% HFR decrement for open-cathode PEMFC operation is more likely due to improved membrane hydration induced by ionomer related water retention under dry conditions. This is accompanied by a moderate reduction in R_{ct} as another indication of ionomer related improvements in the CL performance. A further reduction in HFR to 3.45 mΩ is observed by replacing the 50 μm Nafion® 212 membrane with a 20 μm Aquivion membrane in MEA-4. The low HFR is primarily attributed to the reduced membrane thickness which offers less protonic resistance when combined with good water retention facilitated by the same SSC ionomer with low EW in both membrane and CLs. This trend in HFR is believed to be a major contributing factor to the CD enhancement for the improved MEA designs. Consequently, the successive R_{ct} decrements from MEA-2 to MEA-3 and further to MEA-4 by 23% and 9% respectively can be attributed to the increased cell temperature stemming from the enhanced CD with SSC ionomer (Figure D.5). The HFR of MEA-5 is close to that of MEA-4; however, the R_{ct} is found to decrease for MEA-5 as compared to MEA-4. This outcome is likely a result of enhanced O_2 availability at the active sites of the CCL in the presence of a more porous and thinner GDL [37].

These experimental results are comparable to our previously published modelling predictions [8], [11] where a 3D computational fuel cell model was used to establish the effect of ionomer property changes, membrane changes, and MPL/GDL modifications for open-cathode PEMFCs. The model revealed the theoretical benefits of an ionomer with a low water sorption/desorption rate constant (γ) to aid water retention at the CCL and thereby increase the CD performance by up to 130% at 0.6 V [11]. Similar water retention capability is featured experimentally in the present work using SSC ionomers with low EW over conventional LSC ionomers. Both results point toward enhanced water retention capability and pave pathways for designing novel materials with low γ and EW. The experimentally observed benefits of a thin membrane, when paired with the same ionomer, also follow the trend predicted by modelling results due to less ohmic resistance offered by such membranes. The present experimental findings for the thinner, low-density GDL (MEA-5) are also corroborated by the modelling results, wherein a highly porous, thinner MPL was predicted to enhance CD performance by means of increased mole fraction of

O_2 in the CCL. The magnitude of decrement in R_{ct} achieved experimentally with MEA-5 is however constrained by the limited availability of desired commercial GDLs with high porosity and low thickness. It further opens the scope for designing novel materials for high-performing open-cathode fuel cell systems based on the collective predictions from both modelling and experimental works reported herein.

Conclusions

The effect of experimentally tuned membrane electrode assembly design was evaluated in this work for a 25 cm^2 single-cell open-cathode setup operated at the ambient condition of 40°C and 40% RH. A total of five MEAs were tested at the given operating condition with a commercial MEA taken as the baseline. The other four MEAs were fabricated in-house and the subsequent effects of ionomer, membrane, and GDL changes were analyzed by comparing the average current densities obtained at fixed cell voltages of 0.6 V and 0.4 V. The three MEAs having SSC ionomer with low EW consistently achieved major performance improvement for the open-cathode cell by inducing better water retention capability at the CCL site which leads to improved protonic conduction in an otherwise dry environment. The subsequent introduction of a thinner membrane with the same low-EW SSC ionomer contributed a further CD increment of 44% at 0.6 V owing to drastically reduced ohmic cell resistance as measured by EIS. Lastly, a thinner GDL with a more porous structure was found to elevate the cell performance by an additional 15% at 0.4 V through improved oxygen transport and thus leads to a suitable MEA design for high-performing open cathode PEMFCs. Importantly, the tuned MEA designs were able to leverage the incremental temperature rise at high CDs toward improved kinetics, as manifested from reduced charge transfer resistance measured by EIS. This capability was enabled by the improved water retention of the modified ionomer and membrane in order to avoid or delay membrane dry out. The results obtained experimentally in this work were also corroborated by theoretical predictions from computational modelling results for similarly designed and operated open-cathode fuel cells. In our future work, efforts will be made to develop novel materials designed for the specific requirements of high-performing open-cathode PEMFC systems using the insights obtained from this work, with the goal to approach the performance of conventional, liquid-cooled PEMFCs.

Acknowledgments

This work was supported by Indian Oil R&D Centre, Faridabad, India, and Simon Fraser University, Canada under the SFU-IOCL joint PhD program in clean energy. The authors deeply acknowledge the technical advice offered by Dr. K. Mohanraju and Dr. S. Meenakshi at Indian Oil R&D Centre, India toward the electrode fabrication process and experiments at the fuel cell materials evaluation laboratory. This research was undertaken, in part, thanks to funding from the Canada Research Chairs program.

References

[1] C. Y. Ling, H. Cao, Y. Chen, M. Han, and E. Birgersson, “Compact open cathode feed system for PEMFCs,” *Appl. Energy*, vol. 164, pp. 670–675, 2016, [Online]. Available: http://dx.doi.org/10.1016/j.apenergy.2015.12.012.

[2] E. Pahon, S. Jemei, J.-P. Chabriat, and D. Hissel, “Impact of the temperature on calendar aging of an open cathode fuel cell stack,” *J. Power Sources*, vol. 488, p. 229436, 2021, [Online]. Available: https://www.sciencedirect.com/science/article/pii/S0378775320317195.

[3] J. Larminie, A. Dicks, and M. S. McDonald, *Fuel cell systems explained*, vol. 2. J. Wiley Chichester, UK, 2003.

[4] A. P. Sasmito, E. Birgersson, K. W. Lum, and A. S. Mujumdar, “Fan selection and stack design for open-cathode polymer electrolyte fuel cell stacks,” *Renew. Energy*, vol. 37, no. 1, pp. 325–332, 2012, [Online]. Available: http://dx.doi.org/10.1016/j.renene.2011.06.037.

[5] M. Kandidayeni, A. Macias F, L. Boulon, and S. Kelouwani, “Efficiency Enhancement of an Open Cathode Fuel Cell through a Systemic Management,” *IEEE Trans. Veh. Technol.*, vol. 68, no. 12, pp. 11462–11472, 2019.

[6] M. Akbari, A. Tamayol, and M. Bahrami, “Thermal assessment of convective heat transfer in air- Cooled PEMFC stacks: An experimental study,” *WHEC 2012 Conf. Proc. - 19th World Hydrog. Energy Conf.*, vol. 29, pp. 1–11, 2012, [Online]. Available: http://dx.doi.org/10.1016/j.egypro.2012.09.002.

[7] M. Andisheh-Tadbir, A. Desouza, M. Bahrami, and E. Kjeang, “Cell level modeling of the hygrothermal characteristics of open cathode polymer electrolyte membrane fuel cells,” *Int. J. Hydrogen Energy*, vol. 39, no. 27, pp. 14993–15004, 2014.

[8] A. Sagar, S. Chugh, K. Sonkar, A. Sharma, and E. Kjeang, “A computational

analysis on the operational behaviour of open-cathode polymer electrolyte membrane fuel cells," *Int. J. Hydrogen Energy*, vol. 45, no. 58, pp. 34125–34138, Oct. 2020, [Online]. Available: https://doi.org/10.1016/j.ijhydene.2020.09.133.

[9] S. Strahl, A. Husar, and M. Serra, "Development and experimental validation of a dynamic thermal and water distribution model of an open cathode proton exchange membrane fuel cell," *J. Power Sources*, vol. 196, no. 9, pp. 4251–4263, 2011.

[10] Y. Liu, C. Ji, W. Gu, J. Jorne, and H. A. Gasteiger, "Effects of Catalyst Carbon Support on Proton Conduction and Cathode Performance in PEM Fuel Cells," *J. Electrochem. Soc.*, vol. 158, no. 6, p. B614, 2011.

[11] A. Sagar, S. Chugh, A. Sharma, and E. Kjeang, "Strategic ionomer design for high performing fuel cells with open cathode," *Int. J. Hydrogen Energy*, vol. 47, no. 3, pp. 1940–1946, 2022, [Online]. Available: https://doi.org/10.1016/j.ijhydene.2021.10.131.

[12] R. W. Atkinson, Y. Garsany, J. A. Rodgers, M. W. Hazard, R. O. Stroman, and B. D. Gould, "Influence of Cathode Catalyst Layer Ionomer on Air-Cooled, Open-Cathode Fuel Cells," *ECS Trans.*, vol. 80, no. 8, pp. 461–475, 2017.

[13] S. Poojary, M. N. Islam, U. N. Shrivastava, E. P. L. Roberts, and K. Karan, "Transport and Electrochemical Interface Properties of Ionomers in Low-Pt Loading Catalyst Layers: Effect of Ionomer Equivalent Weight and Relative Humidity," *Molecules*, vol. 25, no. 15, p. 3387, Jul. 2020, [Online]. Available: https://www.mdpi.com/1420-3049/25/15/3387.

[14] Y. Ono, A. Ohma, K. Shinohara, and K. Fushinobu, "Influence of Equivalent Weight of Ionomer on Local Oxygen Transport Resistance in Cathode Catalyst Layers," *J. Electrochem. Soc.*, vol. 160, no. 8, pp. F779–F787, 2013.

[15] Y. Garsany, M. B. Sassin, B. D. Gould, R. Marielle, E. Hjelm, and K. Swider-lyons, "Influence of Short-Side-Chain Perfluorosulfonic Acid Ionomer As Binders on the Performance of Fuel Cell Cathode Catalyst Layers," in *ECS Meeting Abstracts*, 2017, vol. MA2017-02, no. 1469, pp. 33–35, [Online]. Available: https://iopscience.iop.org/article/10.1149/MA2017-02/34/1469.

[16] S. O. Mert, I. Dincer, and Z. Ozcelik, "Performance investigation of a transportation PEM fuel cell system," *Int. J. Hydrogen Energy*, vol. 37, no. 1, pp. 623–633, 2012, [Online]. Available: https://www.sciencedirect.com/science/article/pii/S0360319911021008.

[17] M. Tohidi, S. H. Mansouri, and H. Amiri, "Effect of primary parameters on the performance of PEM fuel cell," *Int. J. Hydrogen Energy*, vol. 35, no. 17, pp. 9338–9348, 2010, [Online]. Available: https://www.sciencedirect.com/science/article/pii/S0360319910006294.

[18] R. Omrani and B. Shabani, "Gas diffusion layer modifications and treatments for improving the performance of proton exchange membrane fuel cells and electrolysers: A review," *Int. J. Hydrogen Energy*, vol. 42, no. 47, pp. 28515–28536, Nov. 2017, [Online]. Available: https://linkinghub.elsevier.com/retrieve/pii/S0360319917338065.

[19] H. K. Atiyeh, K. Karan, B. Peppley, A. Phoenix, E. Halliop, and J. Pharoah, “Experimental investigation of the role of a microporous layer on the water transport and performance of a PEM fuel cell,” *J. Power Sources*, vol. 170, no. 1, pp. 111–121, Jun. 2007, [Online]. Available: https://linkinghub.elsevier.com/retrieve/pii/S0378775307007203.

[20] D. Malevich, E. Halliop, B. A. Peppley, J. G. Pharoah, and K. Karan, “Investigation of Charge-Transfer and Mass-Transport Resistances in PEMFCs with Microporous Layer Using Electrochemical Impedance Spectroscopy,” *J. Electrochem. Soc.*, vol. 156, no. 2, p. B216, 2009.

[21] E. Carcadea, M. Varlam, M. Ismail, D. B. Ingham, A. Marinoiu, M. Raceanu, C. Jianu, L. Patularu, and D. Ion-Ebrasu, “PEM fuel cell performance improvement through numerical optimization of the parameters of the porous layers,” *Int. J. Hydrogen Energy*, vol. 45, no. 14, pp. 7968–7980, Mar. 2020, [Online]. Available: https://linkinghub.elsevier.com/retrieve/pii/S0360319919332380.

[22] C.-J. Tseng and S.-K. Lo, “Effects of microstructure characteristics of gas diffusion layer and microporous layer on the performance of PEMFC,” *Energy Convers. Manag.*, vol. 51, no. 4, pp. 677–684, Apr. 2010, [Online]. Available: https://linkinghub.elsevier.com/retrieve/pii/S0196890409004312.

[23] M. Blanco and D. P. Wilkinson, “Investigation of the effect of microporous layers on water management in a proton exchange membrane fuel cell using novel diagnostic methods,” *Int. J. Hydrogen Energy*, vol. 39, no. 29, pp. 16390–16404, 2014, [Online]. Available: http://dx.doi.org/10.1016/j.ijhydene.2014.07.147.

[24] H. S. Chu, C. Yeh, and F. Chen, “Effects of porosity change of gas diffuser on performance of proton exchange membrane fuel cell,” *J. Power Sources*, vol. 123, no. 1, pp. 1–9, 2003.

[25] R. Roshandel, B. Farhanieh, and E. Saievar-Iranizad, “The effects of porosity distribution variation on PEM fuel cell performance,” *Renew. Energy*, vol. 30, no. 10, pp. 1557–1572, 2005, [Online]. Available: https://www.sciencedirect.com/science/article/pii/S0960148104004574.

[26] Y. Zhou, K. Jiao, Q. Du, Y. Yin, and X. Li, “Gas diffusion layer deformation and its effect on the transport characteristics and performance of proton exchange membrane fuel cell,” *Int. J. Hydrogen Energy*, vol. 38, no. 29, pp. 12891–12903, 2013, [Online]. Available: http://dx.doi.org/10.1016/j.ijhydene.2013.05.150.

[27] K. T. Jeng, S. F. Lee, G. F. Tsai, and C. H. Wang, “Oxygen mass transfer in PEM fuel cell gas diffusion layers,” *J. Power Sources*, vol. 138, no. 1–2, pp. 41–50, 2004.

[28] J. Park, H. Oh, Y. Il Lee, K. Min, E. Lee, and J. Y. Jyoung, “Effect of the pore size variation in the substrate of the gas diffusion layer on water management and fuel cell performance,” *Appl. Energy*, vol. 171, pp. 200–212, 2016, [Online]. Available: http://dx.doi.org/10.1016/j.apenergy.2016.02.132.

[29] S. Park, J.-W. Lee, and B. N. Popov, “Effect of PTFE content in microporous layer on water management in PEM fuel cells,” *J. Power Sources*, vol. 177, no. 2, pp. 457–463, Mar. 2008, [Online]. Available:

https://linkinghub.elsevier.com/retrieve/pii/S0378775307025657.

[30] F.-B. Weng, C.-Y. Hsu, and M.-C. Su, “Experimental study of micro-porous layers for PEMFC with gradient hydrophobicity under various humidity conditions,” *Int. J. Hydrogen Energy*, vol. 36, no. 21, pp. 13708–13714, Oct. 2011, [Online]. Available: https://linkinghub.elsevier.com/retrieve/pii/S0360319911018477.

[31] T. Kitahara, H. Nakajima, and K. Mori, “Hydrophilic and hydrophobic double microporous layer coated gas diffusion layer for enhancing performance of polymer electrolyte fuel cells under no-humidification at the cathode,” *J. Power Sources*, vol. 199, pp. 29–36, 2012, [Online]. Available: http://dx.doi.org/10.1016/j.jpowsour.2011.10.002.

[32] J. H. Chun, K. T. Park, D. H. Jo, J. Y. Lee, S. G. Kim, S. H. Park, E. S. Lee, J. Y. Jyoung, and S. H. Kim, “Development of a novel hydrophobic/hydrophilic double micro porous layer for use in a cathode gas diffusion layer in PEMFC,” *Int. J. Hydrogen Energy*, vol. 36, no. 14, pp. 8422–8428, 2011, [Online]. Available: http://dx.doi.org/10.1016/j.ijhydene.2011.04.038.

[33] T. Hottinen, O. Himanen, and P. Lund, “Effect of cathode structure on planar free-breathing PEMFC,” *J. Power Sources*, vol. 138, no. 1, pp. 205–210, 2004, [Online]. Available: https://www.sciencedirect.com/science/article/pii/S0378775304006998.

[34] A. Schmitz, M. Tranitz, S. Wagner, R. Hahn, and C. Hebling, “Planar self-breathing fuel cells,” *J. Power Sources*, vol. 118, no. 1, pp. 162–171, 2003, [Online]. Available: https://www.sciencedirect.com/science/article/pii/S0378775303000806.

[35] Q. Meyer, S. Ashton, P. Boillat, M. Cochet, E. Engebretsen, D. P. Finegan, X. Lu, J. J. Bailey, N. Mansor, R. Abdulaziz, *et al.*, “Effect of gas diffusion layer properties on water distribution across air-cooled, open-cathode polymer electrolyte fuel cells: A combined ex-situ X-ray tomography and in-operando neutron imaging study,” *Electrochim. Acta*, vol. 211, pp. 478–487, 2016, [Online]. Available: https://www.sciencedirect.com/science/article/pii/S0013468616313858.

[36] R. W. Atkinson, J. A. Rodgers, M. W. Hazard, R. O. Stroman, and B. D. Gould, “Influence of cathode gas diffusion media porosity on open-cathode fuel cells,” *J. Electrochem. Soc.*, vol. 165, no. 11, pp. F1002–F1011, 2018.

[37] A. Sagar, S. Chugh, A. Sharma, and E. Kjeang, “Microporous Layer Design for High Performing Open-Cathode Polymer Electrolyte Membrane Fuel Cells,” in *ECS Meeting Abstracts*, 2020, vol. MA2020-02, no. 33, p. 2147, [Online]. Available: http://dx.doi.org/10.1149/MA2020-02332147mtgabs.

[38] F. Brèque, J. Ramousse, Y. Dubé, K. Agbossou, and P. Adzakpa, “Sensibility study of flooding and drying issues to the operating conditions in PEM Fuel Cells,” *Int. J. Energy Environ. IJEE*, vol. 1, no. 1, pp. 1–20, 2010.

[39] D. Cha, S. W. Jeon, W. Yang, D. Kim, and Y. Kim, “Comparative performance evaluation of self-humidifying PEMFCs with short-side-chain and long-side-chain membranes under various operating conditions,” *Energy*, vol. 150, pp. 320–328, 2018, [Online]. Available: https://doi.org/10.1016/j.energy.2018.02.133.

[40] D. Cha, W. Yang, and Y. Kim, “Performance improvement of self-humidifying PEM fuel cells using water injection at various start-up conditions,” *Energy*, vol. 183, pp. 514–524, 2019, [Online]. Available: https://www.sciencedirect.com/science/article/pii/S0360544219312861.

[41] A. Stassi, I. Gatto, E. Passalacqua, V. Antonucci, A. S. Arico, L. Merlo, C. Oldani, and E. Pagano, “Performance comparison of long and short-side chain perfluorosulfonic membranes for high temperature polymer electrolyte membrane fuel cell operation,” *J. Power Sources*, vol. 196, no. 21, pp. 8925–8930, 2011, [Online]. Available: https://www.sciencedirect.com/science/article/pii/S0378775311000115.

Acronyms

CCL	Cathode catalyst layer
CCM	Catalyst coated membrane
CD	Current density
CL	Catalyst layer
ECSA	Electrochemical surface area
EIS	Electrochemical impedance spectroscopy
EW	Equivalent weight
GDL	Gas diffusion layer
HFR	High frequency resistance
LSC	Long side chain
MEA	Membrane electrode assembly
MPL	Microporous layer

O_2	Oxygen
PEM	Polymer electrolyte membrane
PEMFC	Polymer electrolyte membrane fuel cell
R_{ct}	Charge transfer resistance
RH	Relative humidity
SSC	Short side chain